Università degli Studi di Cagliari

DOTTORATO DI RICERCA

IN FISICA

Ciclo XXVIII

THERMAL PROPERTIES OF GRAPHENE AND GRAPHENE-BASED THERMAL DIODES

A molecular dynamics study

Settore/i scientifico disciplinari di afferenza

FIS/03

Presentata da: Barbarino Giuliana

Coordinatore Dottorato Pr. Alessandro De Falco
Pr. Paolo Ruggerone

Tutor Pr. Luciano Colombo

Esame finale anno accademico 2014 – 2015

UNIVERSITÁ DEGLI STUDI DI CAGLIARI
Facoltá di Scienze Matematiche Fisiche e Naturali
Dipartimento di Fisica

Ph.D. Thesis Fis/03
CICLO XXVIII

THERMAL PROPERTIES OF GRAPHENE AND GRAPHENE-BASED THERMAL DIODES

A molecular dynamics study

BARBARINO GIULIANA

RELATORE: Prof. Luciano Colombo

CORRELATORE: Dott. Claudio Melis

ABSTRACT

In the perspective of manipulating and controlling heat fluxes, graphene represents a promising material revealing an unusually high thermal conductivity κ. However, both experimental and theoretical previous works lack of a strict thermal conductivity value, estimating results in the range 89-5000 W m^{-1} K^{-1}. In this scenario, I address graphene thermal transport properties by means of molecular dynamics simulations using the novel "approach to equilibrium molecular dynamics" (AEMD) technique.

The first issue is to offer some insight on the active debate about graphene thermal conductivity extrapolation for infinite sample. To this aim, I perform unbiased (i.e. with no *a priori* guess) direct atomistic simulations aimed at estimating thermal conductivity in samples with increasing size up to the unprecedented value of 0.1 mm. The results provide evidence that thermal conductivity in graphene is definitely upper limited, in samples long enough to allow a diffusive transport regime for both single and collective phonon excitations.

Another important issue is to characterize at atomistic level the experimental techniques used to estimate graphene thermal conductivity. Some of these use laser source to provide heat. For these reasons, I deal with the characterization of the transient response to a pulsed laser focused on a circular graphene sample. In order to reproduce the laser effect on the sample, the $K - A_1'$ and $\Gamma - E_{2g}$ optical phonon modes, resulting from the decay of photo-excited electrons, are thermalized. The estimated thermal conductivity in the case of these single-mode thermalizations is dramatically reduced with respect to the case in which all the vibrational modes are initially excited. A vibrational density of state (VDOS) analysis is performed to explain such differences, showing that the phonon population distribution remains out of the equilibrium for the whole simulation.

After the characterization of pristine graphene thermal properties, I focus on the possible strategies to control heat transport in graphenebased systems. One possibility is to exploit hydrogenation. In fact, Graphene can react with atomic hydrogen creating a stable material which re-

tains its crystalline hexagonal lattice, called graphane. In the second part of this work, I present the results about thermal conductivity of the three most stable graphane isomers (C-, B- and W-graphane), calculated by AEMD simulations. I observe a dramatic reduction by at least one order of magnitude with respect to pristine graphene, which I explain in terms of the different VDOS and mean-free path distribution between graphene and graphane.
Finally, the deterioration of thermal transport upon hydrogenation in graphene is proposed as a strategy to design a novel thermal diode. I consider three graphane/graphene nanoribbons with vertical, triangular and T-shaped junctions. All of them report a significant thermal rectification, reaching the value of 54% for the triangular interface. The physical origin of the observed rectification is analyzed in terms of the different temperature-dependence of the thermal conductivity between graphene and graphane and the overlap of VDOS for the different morphologies. Moreover, I proposed a continuum model to describe thermal rectification, which is based on the steady state temperature profile, rather than the actual heat flux used in standard analysis.

PUBLICATIONS

---

[1] G. Barbarino, C. Melis and L. Colombo, Effect of hydrogenation on graphene thermal transport, *Carbon*, **80** 167 (2014).

[2] G. Barbarino, C. Melis and L. Colombo, Intrinsic thermal conductivity in monolayer graphene is ultimately upper limited: A direct estimation by atomistic simulations, *Phys. Rev. B*, **91** 035416 (2015).

[3] C. Melis, G. Barbarino and L. Colombo, Exploiting hydrogenation for thermal rectification in graphene nanoribbons, *Phys. Rev. B*, **92** 245408 (2015).

[4] G. Barbarino, G. Fugallo, C. Melis, F. Mauri and L. Colombo, On the propagation of heat waves in graphene (tentative title), in preparation, (2015).

CONFERENCES

The works presented in this thesis have been discussed in the following national and international conferences:

1. (Febr.7, 2014) Contributed talk to "Graphene day"
   University of Catania, (Italy)

2. (July8, 2015) Contributed talk to "Advanced Thermoelectrics at nanoscale: from material to device" CECAM workshop
   FIAP Jean Monnet-Paris, (France)

3. (Sept.15, 2014) Poster contribution to "E-MRS 2014 FALL MEETING"
   Warsaw University of Technology, (Poland)

4. (May26, 2014) Poster contribution to "E-MRS 2014 SPRING MEETING"
   Lille, (France)

Noi vogliamo dunque abolire radicalmente la dominazione e lo sfruttamento dell'uomo sull'uomo, noi vogliamo che gli uomini affratellati da una solidarietà cosciente e voluta cooperino tutti volontariamente al benessere di tutti; noi vogliamo che la società sia costituita allo scopo di fornire a tutti gli esseri umani i mezzi per raggiungere il massimo benessere possibile, il massimo possibile sviluppo morale e materiale; noi vogliamo per tutti pane, libertà, amore, scienza.

— Errico Malatesta

ACKNOWLEDGEMENTS

First, I would like to express my gratitude to my supervisor, Pr. Luciano Colombo, for his guidance during my Ph.D.. Pr. Colombo taught me to be dedicated to my work and he introduced me in the hard but rewarding research world. A special thank to Dr. Claudio Melis for his constant support and insight during my research activity. This work could not be accomplished without their help. I acknowledge Pr. Francesco Mauri and Dr. Giorgia Fugallo for their supervision during my visiting period at the IMPMC. I would also like to thank my referee Pr. Giorgio Benedek for his helpful remarks on my thesis.

I acknowledge financial support by MIUR under project PRIN-GRAF and computational support by CINECA under project THEBUNA.

I would thank my colleagues, especially Roberto for the informatics support, Silvia and Claudia for helping me to stay motivated through the hard times, Tommaso for his friendship. A special thank to my parents for their great love and encouragement, Elena, Ramona and Luana that are alway by my side, no matter how far. Thanks to Mirko for his patience, because he forced me to start the Ph.D. and then remained always by my side. Thanks to all my friends who made my three years in Cagliari so colorful, thanks to Capoeira and thanks to Citro which made me feel less alone during my everyday life.

CONTENTS

ACRONYMS

1D One-dimensional

2D Two-dimensional

3D Three-dimensional

RT Room temperature

MD Molecular Dynamics

EMD Equilibrium Molecular Dynamics

NEMD Non-equilibrium Molecular Dynamics

AEMD Approach to Equilibrium Molecular Dynamics

PDOS (VDOS) Phonon (Vibrational) density of state

MFP Mean free path

NR Nanoribbon

GNR Graphene nanoribbon

GANR Graphane nanoribbon

CNT Carbon nanotube

SWCNT Single-wall Carbon nanotube

TD Thermal diode

TR Thermal rectification

LAMMPS Large-scale Atomic/Molecular Massively Parallel Simulator

BTE Boltzmann transport equation

SMA Single mode approximation

RTA Relaxation time approximation

EIP Empirical interatomic potential

REBO Reactive empirical bond order potential

DFT Density functional theory

DFPT Density functional perturbation theory

PLTR Pulsed laser-assisted thermal relaxation technique

VACF Velocity autocorrelation function

CG Conjugate gradient minimization

ITR Interface thermal resistance

Part I

INTRODUCTION

Since the first Graphene exfoliation in 2004[5], for which A. Geim and K. Novoselov are awarded the Noble Prize in 2010, it has been absolutely clear how many unique and fascinating qualities this material has, such as the remarkable mechanical, electrical and thermal properties. In particular, thermal transport in graphene has been largely studied both experimentally and theoretically, thanks to the promising technological applications in the framework of heat and energy production management as well as in thermal circuits for logic devices.

1

INTRODUCTION

Thermal management is a critical issue in electronic industry for the designing of next generation integrated circuits. The performances of ultra-large scale integrated circuits are indeed critically affected by temperature. The number of components packed in a single chip has been increasing at an amazing rate as predicted by Moore's law, stating that the number of transistors in a dense integrated circuit doubles approximately every two years [6] (see Fig.1.1).

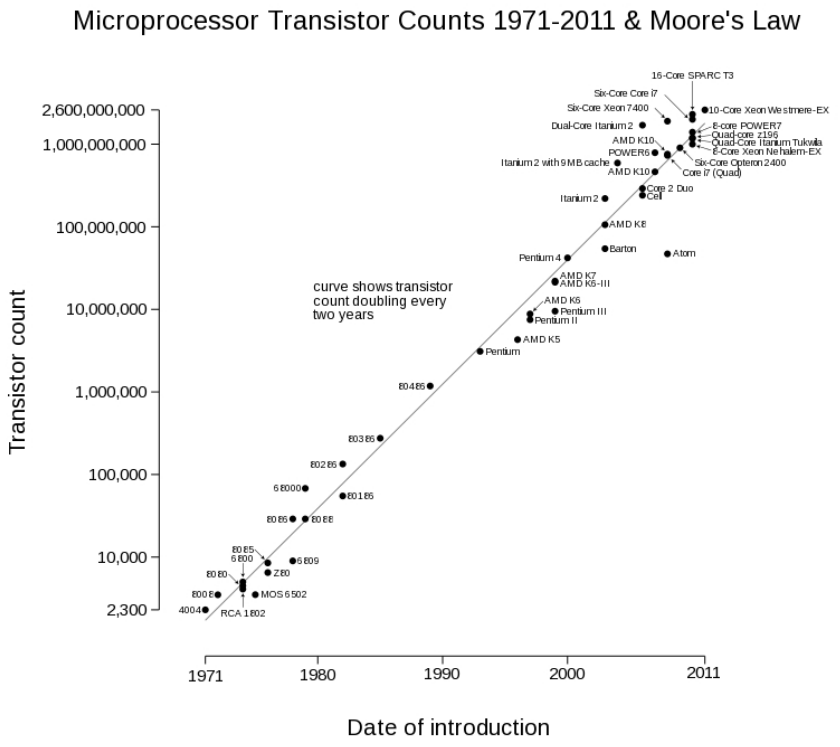

Figure 1.1: Microprocessor transistor counts against dates of introduction (note the logarithmic vertical scale). The line corresponds to exponential growth with transistor count doubling every two years, as predicted by Moore's law.

The raise of the number of component interconnections and the transistor size reduction increase the importance to remove heat produced by thermal resistance. For these reasons, recent years have seen a rapid growth of interest by the scientific and engineering communities in the thermal properties of materials [7].

The amount of energy that can be transported away from a given device is limited by the thermal conductivity κ of the circuit material. In this perspective graphene represents a promising material revealing an unusually high thermal conductivity [8, 9, 10, 11].

Graphene is a two-dimensional rippled sheet of sp^2-hybridized carbon atoms

Graphene is a two-dimensional (2D) atomic crystal composed by carbon atoms arranged in a hexagonal lattice. It is only one atom thick and despite the well-known Mermin rule [12, 13], stating that two-dimensional crystals are thermodynamically unstable, it still displays long-range crystalline order. In fact, the stability of macroscopic 2D object has been questioned for long time, both theoretically and experimentally [14].

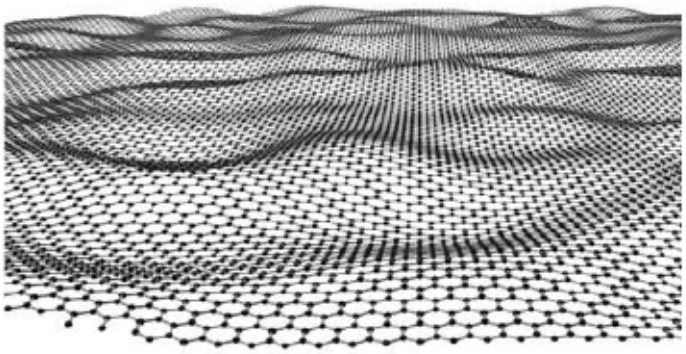

Figure 1.2: Example of rippled graphene sample after a thermalization at T=300 K in a molecular dynamics simulation.

Actually, transmission electron microscopy studies reveal that the suspended graphene sheets are not perfectly flat but they exhibit intrinsic microscopic roughening resulting in ripples with a size distribution peaked around 50-100 Å[15]. The observed corrugations may provide an explanation for the stability of this two-dimensional crystal [16, 17]. In Fig.1.2, I show the rippled

graphene sample, minimized and thermalized at T=300 K, during a molecular dynamics simulation (MD).

On the other side, during the high temperature crystal growth procedure, thermal fluctuations, detrimental for the stability, rapidly grow and, in the meanwhile, the phonon density increases leading to a divergence on a macroscopic scale. This forces 2D crystallites to morph into a variety of stable three-dimensional 3D structures. However, it is possible to grow a monolayer material inside or on top of another crystal (as an inherent part of a 3D system) and then remove it from the bulk when the temperature is sufficiently low such that thermal fluctuations are unable to break atomic bonds [18]. One chance is to mechanically split strongly-layered materials such as graphite into individual atomic planes. This technique is referred to as micromechanical cleavage technique, or the "Scotch tape method", and it is how graphene was first isolated and studied [5]. Instead of cleaving graphite manually, it is also possible to automate the process by employing, for example, ultrasonic cleavage. An alternative approach is to start with graphitic layers grown epitaxially on top of other crystals. During the 3D growth, the layers remain bound to the underlying substrate and the bond-breaking fluctuations are suppressed. Eventually, the epitaxial structure is cooled down and the substrate removed by chemical etching. Today there are several methods to produce graphene that can be extended to industrial scale. For electronics applications, high quality graphene can be grown on silicon carbide and other substrates through a process known as chemical vapor deposition. For bulk applications in nanocomposites or printed electronics, natural graphite can be used to create graphene flakes in solution. Finally, direct chemical synthesis can be used to create small graphene structures with well-defined geometries.[18] Graphene exhibits a number of intriguing properties. Its charge carriers exhibit giant intrinsic mobility, have the smallest effective mass (it is actually zero) and can travel micrometer-long distances without scattering. Graphene can sustain current densities 6 orders higher than copper, it is impermeable to gases and it shows su-

Synthesis of graphene

Main graphene properties

perior mechanical properties with Young's modulus of 1 TPa and record stiffness. Electrons in single-layer graphene behave like massless relativistic Dirac fermions and therefore electron transport is described by a Dirac-like equation, which allows the investigation of relativistic quantum phenomena in a bench-top experiment and gives rise to unique effects such as quantum spin Hall state. Its extraordinary high room temperature (RT) carrier mobility, conductance quantization and possibilities of inducing a band gap through the lateral quantum confinement make graphene a promising material for the future electronic circuits.

The strong and anisotropic bonding and the low mass of the carbon atoms give to graphene and related materials unique thermal properties, forming a rich playground for new discoveries of thermal transport physics and potentially leading to novel thermal management applications [19, 20, 21].

Thermal conductivity is the property of a material to conduct heat

Thermal conductivity κ is introduced through the empirical Fourier law $\mathbf{j} = -\kappa\nabla T$, where $\mathbf{j}$ is the heat flux and ∇T is the temperature gradient. In more general case, the thermal conductivity is a tensor of the second order that has nine components, where $\kappa_{xy} = \kappa_{yx}$, $\kappa_{xz} = \kappa_{zx}$, and $\kappa_{yz} = \kappa_{zy}$ according to the reciprocity relation derived from the Onsagar's principle of thermodynamics of irreversible processes. However, in isotropic medium thermal conductivity does not depend on the direction of the heat flow and κ is treated as a constant. In the specific case of a 2D material such as graphene, anyway, just the in-plane components of κ are meaningful.

In general, in a solid material, heat is carried by lattice vibrations and electrons. The value of κ_e, i.e. the thermal conductivity relates to electrons, can be obtained from the measurement of the electrical conductivity σ via the Wiedemann-Franz law: $\frac{\kappa_e}{\sigma T} = \frac{\pi^2 K_B^2}{3e^2}$, where K_B is the Boltzmann constant and e is the electronic charge [22]. In the case of graphene at room temperature, showing a high total thermal conductivity, κ_e corresponds to just $\sim$ 1% of the total κ. This may seem unusual for a semimetal but it is in line with the prediction for graphite [9]. In fact, in carbon material, the strong sp^2 covalent bond be-

tween adjacent carbon atoms (for instance they are among the strongest in nature) results in an efficient heat transfer by lattice vibrations. In particular, in graphene the electronic thermal conductivity is limited by the very small (vanishing) Fermi surface, whereas the lattice contribution is very large due to the very low anharmonicity at ordinary temperatures.

Quantization of the lattice vibrational modes

For this reason, a deep knowledge of thermal transport in graphene, as well as a reliable estimation of its thermal conductivity, needs an analysis of lattice vibrational normal modes. Quantum theory describes these modes as particles called phonons. Each phonon with wave vector $\mathbf{q}$ is characterized by a specific frequency $\omega(\mathbf{q})$ or energy ($E = \hbar\omega$) and a group velocity $\mathbf{v}(\mathbf{q}) = \partial\omega(\mathbf{q})/\partial\mathbf{q}$. The connection between frequencies and wave-vectors are described in the dispersion relation curves of the system. While for graphite many methods exist to experimentally characterize the phonon band structure, such as inelastic x-ray or neutron scattering, they do not give enough signal with graphene because of its two-dimensional nature. Hence, only a very limited number of experimental data points for the graphene phonon band structure were obtained using inelastic light scattering (Raman) [23]. Raman spectroscopy experiments, in fact, enable to map out a general in-plane phonon dispersion by using the excitation energy dependence of the various Raman lines. In Fig.1.3, I report the results obtained in Ref.[24], in which by using Raman spectroscopy with different laser energies, a detailed experimental phonon dispersion relation for many points in the Brillouin zone has been mapped. Since they analyzed graphene samples on Cu foils, in order to avoid the substrate effect on the Raman spectrum, they considered the difference between the spectra of the two isotopes C^{13} and C^{12}, identifying peaks which only correspond to graphene, even in the presence of substrate-induced peaks. The experimental points are superimposed on theoretical phonon dispersions obtained from fully *ab initio* calculations based on density functional theory corrected with GW [25].

Graphene phonon dispersion curve obtained by Raman spectroscopy

Another useful information about the heat transport behavior of a solid is the vibrational density of state VDOS (or phonon den-

sity of state PDOS) i.e. a function which describes the number of states per unit angular frequency and area that are supported by the material.

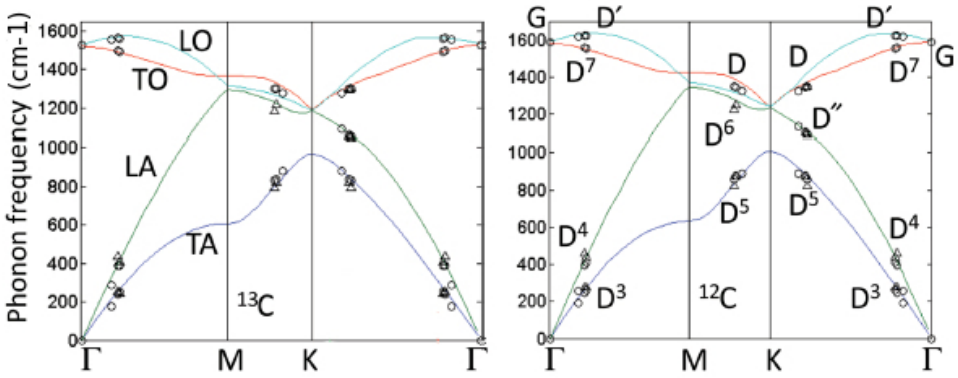

Figure 1.3: [Figure from Ref.[24]] Experimental phonon energies obtained in Ref.[24] at the corresponding wave numbers superposed onto the theoretical phonon dispersions taken from Ref.[25] for the C^{13} (left) and C^{12} (right) samples. In the top left the four in-plane phonon branches have been labeled, whereas the corresponding Raman lines are identified in the top right.

Contribute to graphene thermal transport by ZA flexural phonons

The graphene unit cell, shown by dashed lines in Fig.1.4, contains N=2 carbon atoms. This leads to the formation of three acoustic (A) and $3N-3$=3 optical (O) phonon modes. Longitudinal (L) modes correspond to atomic displacements along the wave propagation direction (compressive waves), while transverse (T) modes correspond to in-plane displacements perpendicular to the propagation direction (shear waves). In typical three dimensional (3D) solids transverse modes can have two equivalent polarizations, but the unique 2D nature of graphene allows out-of-plane atomic displacements, also known as flexural (Z) phonons. At low wave vector $\mathbf{q}$ near the center of the Brillouin zone, which is shown in Fig.1.4, the frequencies of the transverse acoustic (TA) and longitudinal acoustic (LA) modes have linear dispersions, while the flexural ZA modes have an approximately quadratic dispersion. The existence and features of these ZA modes are responsable for many of the unusual thermal properties of graphene [26, 27, 28].

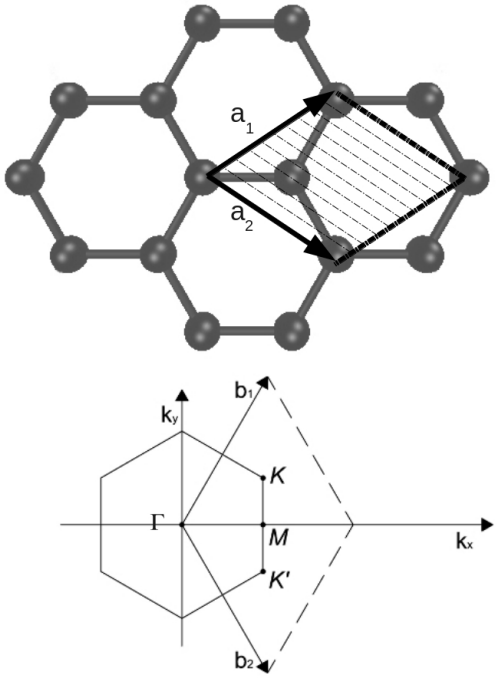

Figure 1.4: (Top) Graphene crystal lattice in which the rhombic unit cell is shown as a shaded region. (Bottom) The graphene Brillouin zone.

Most investigations underline the dominant role in the transport of heat played by acoustic phonons [26, 29, 30, 31, 32]. Even if initially it has been guessed that only in-plane phonons carry heat [33] (LA and TA), more recently it has been recognized that the ZA phonons are in fact fundamental in graphene thermal transport [31, 34, 35]. Despite they show a very low group velocity, their life-time is comparatively very long due to selection rules for three-phonon scattering. In fact, by imposing that the lattice potential energy must be invariant under the symmetry operations of the lattice, just phonon-phonon scatterings with even number of flexural modes have been allowed. This three-phonon scattering rule strongly restricts the phase space for ZA scattering.

Following this picture, the thermal transport phenomena are described in terms of many-body system of interacting phonons and, in particular, the anharmonic interactions between phonons

cause the thermalization and resistance to current flow, resulting in intrinsic thermal conductivity coefficient. The κ is also limited by some extrinsic effects, such as the phonon scattering with edges, defects or different isotopes in the graphene sample.

Phonon life-time and mean free path

All the scattering event rates contribute to a finite phonon life-time $\tau(\mathbf{q})$ and to its corresponding mean-free path (MFP) $\lambda(\mathbf{q}) = \tau(\mathbf{q})\mathbf{v}(\mathbf{q})$ i.e. the average space traveled by the phonon without experience scatterings. Noting that MFP is a spectral property that depends on the frequency of each phonon, it is clear that what is called the MFP of a material is an average MFP of all the phonons which mainly contribute to thermal conduction. In the case of graphene, it has been predicted theoretically around $\sim 1\mu m$ [31]. It can be also calculated by using $\kappa = (1/2)C_V V\lambda$, where $(1/2)$ takes into account the material 2D nature, C_V is the specific heat and V the averaged phonon velocity, from the experimental measured thermal conductivity (for example $\lambda \sim$ 800 nm in Ref.[11]).

Measurement of the graphene thermal conductivity

The first experiment aimed to measure graphene thermal conductivity was done by Balandin in 2008 by using a technique called Optothermal Raman measure, which basically uses a laser beam focused on the sample as heater source and estimates the established temperature gradients by measuring the Raman G-peak shift [8, 36]. This last, in fact, manifests a strong temperature dependence[37] which enables to monitor the local temperature change produced by the laser excitation. Since this first measure of graphene thermal conductivity, several experimental and theoretical investigations have been focused on the characterization of graphene thermal properties. However, at the moment it is still difficult to assign a well defined intrinsic graphene thermal conductivity value since all the experimentally κ measures scatter between 600 and 5000 W m^{-1} K^{-1} [8, 20, 11, 27]. These differences have been justified in terms of different sample qualities, defects and grains, thickness non uniformity, strain distribution and temperature of the sample.

Generally graphene thermal conductivity can be measured by means of two groups of techniques: transient and steady-state[20]. In transient techniques κ is measured by monitoring thermal

gradients as a function of time. As far as concerns steady-state techniques, a thermal gradient is established across the sample and thermal conductivity is then measured once such a gradient is constant with time. Both steady-state and transient methods can rely on electrical means for supplying heating power or use the power provided by light. Some examples of transient methods are:

a) the thermal bridge: in this case a direct current is used to heat the sample and the temperature difference between T_{heater} and T_{sensor} is recorded trough two electrical resistances (R_{heater} and R_{sensor}) [38].

b) the heat spreader method: in Ref.[39] a metallic heater is used as Joule dissipator that spreads heat trough the graphene flake and the resulting temperature profile along the sample is measured by three resistance temperature sensors in series.

c) Non-contact optical microscopy [40]: this method is based on a thermal lens microscopy setup with two pump-probe laser beams configuration. The thermal lens signal is proportional to the optical absorption and to the thermal conductivity of the examined graphene sample.

The optothermal Raman technique, cited above, is indeed one example of steady-state experiment.

Theoretical investigations about graphene thermal conduction

In order to rationalize this experimental scenario, several theoretical models have been implemented [34, 41, 30] to better estimate κ by accurately correlating thermal transport to the atomistic structural and morphological features. Many different approaches, both *ab initio* technique without introduction of any experimental-fitted parameter and empirical methods, have been widely used to study thermal conductivity in pristine graphene, including Boltzmann transport equation [30, 31, 29], molecular dynamics [42, 43, 44, 45], Green's functions approaches [46] and lattice dynamics [**?** 33]. However also in the framework of theoretical simulations, there are large discrepancies in the resulting thermal conductivity values as due to the different numerical technicalities and/or the model potentials

used. The graphene thermal conductivity has been predicted to range between 89 and 3000 W m^{-1} K^{-1} [47, 48, 49].

In my Ph.D. research, I focused in particular on molecular dynamics methodologies which accurately describe graphene phonon transport properties.

I In Chapter 3, I introduce some of the most common computational methods. As far as concerned MD, both equilibrium (EMD) [50] and non-equilibrium (NEMD) [51] methods have been previously implemented. Recently, a novel transient technique named "approach to equilibrium molecular dynamics" (AEMD) [52, 53] has been proposed, which basically uses the solutions under given border and initial conditions of the Fourier heat-transport equation

$$\frac{\partial T}{\partial t} = \alpha \nabla^2 T \tag{1.1}$$

where α is the thermal diffusivity defined as $\alpha = \frac{\kappa}{\rho C_V}$, ρ is the material density and C_V is the volumetric specific heat. The solution of Eq.1.1 is used in order to fit the time-evolution of simulation temperature profile along the sample. I will focus in particular on the description of NEMD and AEMD, which are the methods I used in my works (AEMD as far as concerned the results in Chapter 4, Chapter 5 and Chapter 6 and NEMD for the results in Chapter 7).

Chapter 4 deals with the estimation of thermal conductivity in monolayer-graphene. In the sample size domain so far explored, the graphene κ shows an intriguing dependence on the sample length L_x along the heat flux direction. An extrapolated infinite value for such a thermal conductivity is sometimes suggested for infinite samples, while other investigations predict anyway an upper limit for it. I address this issue by performing direct atomistic simulations aimed at estimating thermal conductivity in samples with increasing size up to the unprecedented value of L_x=0.1 mm. Our results provide evidence that thermal conductivity in graphene is definitely upper limited in samples long enough to allow a diffusive transport regime for both single and collective phonon excitations.

In Chapter 5, I focus on the characterization via AEMD simulations of the transient response to a pulsed laser focused on a free standing graphene layer. It is interesting to observe heat pulse propagation in a "transient" way since another open issue in graphene thermal transport knowledge is to define the phenomena occurred in transient regime before the thermal equilibrium is reached. Moreover, in order to compare the simulations with experiments, we must take care about the kind of measurement we consider. For example, in the framework of MD simulations, we can distinguish between NEMD techniques that are comparable to a steady-state experiment and AEMD which is based on monitoring the transient evolution towards equilibrium upon a thermal perturbation. For a more realistic simulation of the sample heating by means of a laser, we need to take into account the photo-electronic excitation decay in two principal optical phonons, i.e. A_1' and E_{2g}. With this aim, we thermalized the laser-spot exciting one single optical phonon mode with a specific atom displacement pattern. Interestly enough, the thermal conductivity obtained by fitting the simulation temperature profile with the Fourier analytical solution in the case of this single-mode spot excitation is some order of magnitude lower with respect to the simulation in which all the possible phonon modes are excited. In order to analyze such a difference, the phonon relaxation during the achievement of an uniform temperature distribution is analyzed in terms of phonon density of state (PDOS), reveling what phonon-phonon decay channels occur. Nevertheless, the dynamical response to a heat pulse as is described by Fourier diffusive equation (Eq.1.1) could be questionable for graphene and some non-Fourier phenomena, such as the evidence of "second sound" feature, could be observed, especially at low temperatures. I address also this issue, considering the analytical solution of a more generic heat equation.

In Chapter 6, I present our investigation addressed to thermal conductivity in graphene upon hydrogenation, motivated by the need to improve our basic understanding of thermal transport properties in 2D carbon sheets, as well as by the possible useful applications. It is well known that the possibility to

control heat fluxes generated by nanoscale thermal gradients is a promising perspective in designing novel switch-on-off devices as alternative to conventional electronics [54]. For instance, novel kind of logic-devices could be created by using phonons as information carriers in thermal circuits[55, 56, 57]. In addition, a tailored heat flux could be used as an effective tool for thermal management improvement in nano-devices, such as on-chip cooling and energy conversion. Heat flow in graphene or graphene composites could be tunable through a variety of means, including phonon scattering by defects, edges or interfaces. In Ref.[47] theoretical NEMD calculations demonstrated that randomly adding as few as 10% hydrogen atoms on top of pristine graphene causes a sharp drop of thermal conductivity. Instead of a randomly decorated graphene lattice, we considered ordered graphene decorations where H atoms are attached to each C atom with 1:1 ratio. This hydrogenated form of graphene is referred to as graphane [58] and it has been synthesized by cold hydrogen plasma exposure at low pressure [59]. I have already explained why in graphene the electronic thermal conductivity is limited. Moreover, considering that graphane is a semiconductor, the electronic contribution to thermal conductivity can be neglected, allowing the use of MD simulation to investigate the thermal behaviour.

In the case of three graphane isomers we observed a dramatic κ reduction by at least one order of magnitude with respect to pristine graphene. We elucidated this reduction in terms of different phonon density of states (PDOS) and mean-free path (MFP) distribution between graphene and graphane.

Finally, in Chapter 7 I propose the possibility to use a suitable hydrogen decoration upon a graphene nano-ribbon (GNR) in order to design an efficient thermal diode (TD), i.e. a thermal device where the magnitude of the heat flux depends on the temperature gradient direction (thermal bias). The parameter which indicates the diode's efficiency is called thermal rectification (TR) and it is defined as the relative difference between the

heat flux modulus in the two opposite thermal bias (forward and revers bias)

$$TR = \frac{|\mathbf{J}_{for}| - |\mathbf{J}_{rev}|}{|\mathbf{J}_{rev}|} \tag{1.2}$$

We estimate the thermal rectification for graphane/graphene nanoribbons with vertical, triangular and T-shaped morphologies and we report a significant TR up to $\sim 54\%$ for the triangular one. The dependence of the thermal rectification on the nanoribbon dimensions, vertex angle and temperature gradient is also explored. The physical origin of the observed rectification is analyzed in terms of the different temperature-dependence of the thermal conductivity in the pristine materials and the overlap of phonon densities in the different morphologies. Finally, we propose a model to describe TR, which is only based on the steady state temperature profile, rather than by using heat flux as generally has been done. The model quantitatively predicts thermal rectification in very good agreement with the standard analysis based on the heat flux estimate.

All the simulations presented in this thesis are performed by using the Large-scale Atomic/Molecular Massively Parallel Simulator (LAMMPS) package[60]. LAMMPS is a classical molecular dynamics code that integrates Newton's equations of motion for collections of atoms, molecules, or macroscopic particles that interact via short- or long-range forces with a variety of initial and/or boundary conditions. It can model systems with particles up to millions or billions. It is designed for parallel computers on which LAMMPS uses spatial-decomposition techniques to partition the simulation domain into small 3d sub-domains, one of which is assigned to each processor. The current version of LAMMPS is written in C++.

Large-scale Atomic/Molecular Massively Parallel Simulator

Part II

THEORY OF THERMAL TRANSPORT AND COMPUTATIONAL METHODS

Theory of transport in a material is devoted to study the system response to an external perturbation and to connect some macroscopic phenomena and the related measurable quantities to their microscopical explanations. In the case of thermal transport, the measurable coefficient is the thermal conductivity which can be calculated in terms of the solid lattice vibrations. Several efforts have been done to use computer science and simulation codes to calculate thermal conductivity, both in the framework of *ab initio* calculations than in Molecular Dynamics simulations.

2

BASIC THEORY OF THERMAL TRANSPORT

2.1 INTRODUCTION TO THERMAL TRANSPORT PROBLEMS

Heat transfer is thermal energy in transit due to a spatial temperature difference. Three kinds of heat transfer processes can be considered. The first mode is the conduction, referred to the case of heat transfer across a stationary medium, which may be a solid or a fluid, when a temperature gradient is imposed upon it. The convection mode, on the other side, refers to heat transfer that will occur between a surface and a moving fluid at different temperatures. Finally, the third mode is transferring heat trough thermal radiation, when energy is emitted in the form of electromagnetic waves.

As far as concerned conduction, the processes that sustain heat transfer in this mode are completely related to atomic and molecular activity. In fact, conduction may be viewed as the transfer of energy from the more energetic to the less energetic particles of a system due to interactions between them.
In order to analyze any thermal phenomenon, we must start from a clear microscopic definition of temperature. By considering a system of molecules, we associate the temperature at any point with the energy related to the random translational motion as well as to the internal rotational and vibrational motions of the molecules in proximity to that point. In this picture, higher temperatures are associated with higher molecular energies.

To describe heat conduction processes, an appropriate rate equation may be used to compute the amount of energy being transferred per unit time [61]. This equation is known as Fourier's law:

Heat conduction: Fourier's law and thermal conductivity definition

$$J_x = -\kappa \frac{dT}{dx} \tag{2.1}$$

where J_x is the heat transfer rate in the x-direction per unit area perpendicular to the direction of transfer, $\frac{dT}{dx}$ is the temperature gradient in this direction, while κ is a transport property known as the thermal conductivity which is a characteristic of the whole material. The minus sign is a consequence of the fact that heat is transferred in the direction of decreasing temperature. Exending Eq.2.1 to the case of tridimensional transport, the following vectorial equation is obtained

$$\mathbf{J} = -\kappa \nabla \mathbf{T} \tag{2.2}$$

This last implies that the heat flux is a directional quantity whose direction is normal to a surface of constant temperature, called isothermal surface.

In changing the material (e.g., from a metal to plastic), we would find that this proportionality remains valid. Following this idea, the proportionality may be converted to an equality by introducing a coefficient that is a measure of the material thermal behavior. Hence, we write

$$\kappa_x = \frac{J_x}{\frac{dT}{dx}} \tag{2.3}$$

which is the formal definition of thermal conductivity in a solid material in x-direction. Similar definitions are associated with thermal conductivities in the y- and z-directions. For an isotropic material, in particular, the thermal conductivity is independent on the direction of transfer and therefore $\kappa_x = \kappa_y = \kappa_z$. κ provides an indication of the rate at which energy is transferred by the diffusion process. It depends on the physical structure of the material, atomic and molecular, which is in turn related to the state of the matter. By instance in a solid state system, κ is generally larger with respect to that of a liquid, which is in turn larger than the one of a gas.

Finally, if we embrace the picture of a solid as a system of free electrons and atoms bound in a periodic lattice, thermal energy transport may be due to two effects: the migration of free electrons and the lattice vibrational waves, or in other words the phonons motion (choosing a particle-like description of the phenomenon) [62]. When both electrons and phonons carry ther-

mal heat, the thermal conductivity may be expressed as: $\kappa = \kappa_e + \kappa_{ph}$.

It is important to underline that Fourier's equation is a phenomenological law and it has been developed from experimental evidence rather than being derived from first principles. Moreover, it is a steady state equation, which means that it is valid when the thermal equilibrium is established and the temperature distribution is invariant with time.

The first task in a conduction analysis is to determine the temperature field in a medium resulting from some imposed conditions. This means to know how the temperature varies with position in the system (what we will refer as the temperature profile). Once this distribution is known, the conduction heat flux at any point may be computed by Fourier's law.

However, many heat transfer problems are time dependent. The second task, therefore, is to develop procedures for determining the time dependence of the temperature distribution within a solid during a transient process.

Lamped capacitance method validity and Biot number

The nature of the procedure used to obtain the temperature response depends on assumptions that may be made for the process. For example, a very simple approach, named the "lumped capacitance method", may be used to determine the variation of temperature with time. It is certainly the simplest and most convenient strategy that can be used to solve transient heating and cooling problems. The essence of this method is that the temperature of the solid is spatially uniform at any instant during the transient process or in other words that temperature gradients within the solid are negligible. To better determine under what conditions the lumped capacitance method can be used with reasonable accuracy, we consider a steady-state conduction through a plane wall of area A (see Fig.2.1).

One surface of the wall is maintained at a temperature T_{S1} and the other is exposed to a fluid of temperature $T_\infty < T_{S1}$. The temperature of this surface will be some intermediate value T_{S2}, for which $T_\infty < T_{S2} < T_{S1}$. Hence under a steady-state condition, the surface energy balance is $\kappa A/L(T_{S1} - T_{S2}) = hA(T_{S2} - T_\infty)$, where L is the solid length, κ is the thermal conductivity of

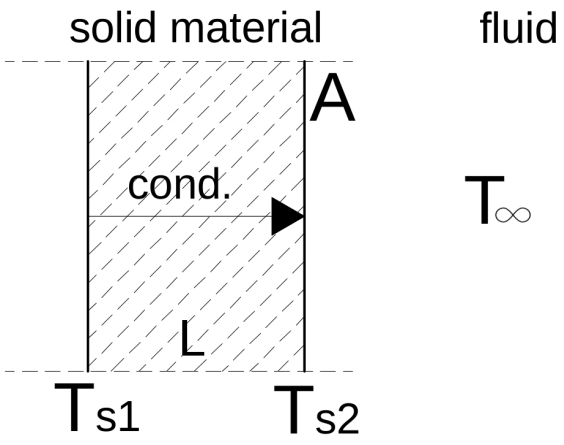

Figure 2.1: Biot number on steady-state temperature distribution in a plane wall of area A.

the solid and h is the interface thermal conductivity. Rearranging, we then obtain $\frac{T_{s1}-T_{s2}}{T_{s2}-T_\infty} = (L/\kappa A)(1/hA) = B_i$. The quantity B_i is a dimensionless parameter, named the Biot number, and it provides a measure of the temperature drop in the solid relative to the temperature difference between the solid's surface and the fluid. The Biot number may be interpreted as a ratio of thermal resistances. In particular, if $B_i << 1$, the resistance to conduction within the solid is much less than the resistance to convection across the interface. Hence, the assumption of a uniform temperature distribution within the solid is reasonable if the Biot number is small. When this condition is verified, the transient temperature response is determined by formulating an overall energy balance on the entire solid. This balance must relate the rate of heat loss at the surface to the rate of change of the internal energy.

The heat diffusion equation

On the other side in the case where $B_i << 1$ is not satisfied, to obtain the transient temperature response an equation which takes into account both the time and spacial dependence of the temperature $T(x,t)$ has to be considered. We have seen by Fourier's law that the flow rate of heat energy through a surface is proportional to the negative temperature gradient across the surface (see Eq.2.1 for one dimensional case). In the absence of work done, a change in internal energy per unit volume in

the material q is proportional to the change in temperature ΔT. That is

$$\Delta q = C_V \rho \Delta T \tag{2.4}$$

where C_V is the volumetric specific heat capacity and ρ is the mass density of the material. This last equation, choosing zero energy at absolute zero temperature becomes

$$q = C_V \rho T \tag{2.5}$$

Increase in internal energy in a small spatial region of the material, $x - \Delta x \leqslant \epsilon \leqslant x + \Delta x$, over the time period $t - \delta t \leqslant \tau \leqslant t + \delta t$, is given by

$$\begin{aligned} C_V \rho \int_{x-\Delta x}^{x+\Delta x} [T(\epsilon, t+\Delta t) - T(\epsilon, t-\Delta t)] d\epsilon \\ = C_V \rho \int_{x-\Delta x}^{x+\Delta x} \int_{t-\Delta t}^{t+\Delta t} \frac{\partial T}{\partial \tau} d\epsilon d\tau \end{aligned} \tag{2.6}$$

where we are assuming that the material has constant mass density and heat capacity through space as well as time. If no work is done and there are neither heat sources nor sinks, the change in internal energy in the interval $[x-\Delta x, x+\Delta x]$ is accounted for enteirely by the flux of heat across the boundaries. By Fourier's law (Eq.2.1), this is

$$\kappa \int_{t-\Delta t}^{t+\Delta t} [\frac{\partial T}{\partial x}(x+\Delta x, \tau) - \frac{\partial T}{\partial x}(x-\Delta x, \tau)] d\tau = \kappa \int_{x-\Delta x}^{x+\Delta x} \int_{t-\Delta t}^{t+\Delta t} \frac{\partial^2 T}{\partial^2 \epsilon} d\epsilon d\tau \tag{2.7}$$

by conservation of energy

$$\int_{x-\Delta x}^{x+\Delta x} \int_{t-\Delta t}^{t+\Delta t} [C_V \rho \frac{\partial T}{\partial \tau} - \kappa \frac{\partial^2 T}{\partial^2 \epsilon}] d\epsilon d\tau = 0 \tag{2.8}$$

This is true for any rectangle $[x - \Delta x, x + \Delta x][t - \Delta t, t + \Delta t]$ and therefore the integrand must vanish identically:

$$C_V \rho \frac{\partial T}{\partial t} - \kappa \frac{\partial^2 T}{\partial^2 x} = 0 \tag{2.9}$$

that can be rewritten as

$$\frac{\partial T}{\partial t} = \frac{\kappa}{C_V \rho} \frac{\partial^2 T}{\partial^2 x} \tag{2.10}$$

This is the most common form of the heat equation, where we can define $\alpha = \frac{\kappa}{C_V \rho}$ that is another thermal coefficient called thermal diffusivity. The heat equation is a parabolic partial differential equation which describes the distribution of heat (or variation in temperature) in a given region over time. Solution of Eq.2.10 provides the temperature distribution $T(x)$ as a function of time (what we will refer as time-evolution of the temperature profile along the sample).

To determine the temperature profile in a medium with length L by solving an appropriate form of the heat equation, it is necessary to fix the physical conditions existing at the boundaries of the medium and, if the situation is time dependent, the conditions existing in the medium at some initial time. In particular, since the heat equation is second order in the spatial coordinates and first order in time, two boundary conditions must be expressed for each coordinate needed to describe the system and only one condition to specify the initial condition. This latter is set once a function $T(x, 0) = f(x)$ is defined for $x \in [0, L]$. As far as concerned boundary of the system, on the other side, four kinds of conditions are commonly encountered in heat transfer problems:

Initial and boundary conditions

a) Dirichlet ($I = [0, L]$) : $T(0, t) = 0 = T(L, t)$.

b) Neumann ($I = [0, L]$) : $Tx(0, t) = 0 = Tx(L, t)$.

c) Robin ($I = [0, L]$) : $Tx(0, t) - a_0 T(0, t) = 0$ and $Tx(L, t) + a_L T(L, t) = 0$.

d) periodic ($I = [-L/2, L/2]$): $T(-L/2, t) = T(L/2, t)$ and $Tx(-L/2, t) = Tx(L/2, t)$.

Different boundary conditions correspond to different physical models of cooling. The first one states that you have a constant temperature at the boundary (in this case equal to zero). This can be considered as the model of an ideal cooler having infinitely large thermal conductivity. The second one states that we have a fixed or constant heat flux at the boundary. If the flux is equal zero, the boundary conditions describe the heat diffusion within an ideal heat insulator. Robin boundary conditions are the mathematical formulation of the Newton's law

of cooling where the heat transfer coefficient α is utilized. The heat transfer coefficient is determined by details of the interface structure (sharpness, geometry) between two media. This law describes quite well the boundary between metals and gas and it is good for describing convective heat transfer at the surface. Finally, the last one reflects the Stefan-Boltzmann law and is good for describing the heat transfer due to radiation in vacuum.

2.2 SOLVING THE HEAT EQUATION IN THE CASE OF PERIODIC BOUNDARY CONDITIONS

In order to solve Eq.2.10 , we separate the variables in T in such a way that $T(x,t) = x(x)u(t)$ by obtaining

$$u_t(t) = \lambda\alpha u(t) \tag{2.11}$$

$$X_{xx} = -\lambda X(x) \tag{2.12}$$

The solutions of 2.11 are in the form:

$$u(t) = ae^{-\lambda\alpha t} \tag{2.13}$$

which specifies, therefore, the time evolution of the temperature.

As far as concerned the spatial dependence, the eigenvalue problem given by 2.12 has to be solved with the following periodic boundary conditions:

- $X(-L/2) = X(L/2)$
- $X_x(-L/2) = X_x(L/2)$

The solution of the differential equation is

$$X(x) = b\cos(\beta x) + c\sin(\beta x) \tag{2.14}$$

Applying the boundary conditions:

- $X(-L/2) = X(L/2) \rightarrow c\sin(\beta L/2) = 0 \rightarrow c = 0$ or $\beta = \frac{2n\pi}{L}$
- $X_x(-L/2) = X_x(L/2) \rightarrow b\beta\sin(\beta L/2) = 0 \rightarrow b = 0$ or $\beta = \frac{2n\pi}{L}$

Therefore we have a sequence of positive eigenvalues:

$$\lambda_n = (\frac{2n\pi}{L})^2 \tag{2.15}$$

with corresponding eigenfunctions:

$$X_n(x) = b\cos(\frac{2n\pi}{L}x) + c\sin(\frac{2n\pi}{L}x) \tag{2.16}$$

I will now show that nontrivial solutions for values of $\lambda < 0$ cannot occur. Suppose that $\lambda < 0$, therefore there exist real numbers b and c such that:

$$X_n(x) = be^{-\sqrt{-\lambda}x} + ce^{\sqrt{-\lambda}x} \tag{2.17}$$

That is umcompatible with the boundary conditions. In the case of $\lambda = 0$, instead, the solution has the form $X(x) = bx + c$ which, in addition with boundary conditions, gives the particular case of temperature uniform in space i.e. $X(x) = X_0$. I remark that if X_n is a sequence of solutions of the heat equation with the periodic boundary conditions, then any linear combination of these solutions will satisfy Eq.2.12 with the same conditions. The general solution will be therefore

$$T(x,t) = a_0 + \sum_{n=1}^{\infty} [a_n\cos(\frac{2n\pi}{L}x) + b_n\mathrm{sen}(\frac{2n\pi}{L}x)]e^{-\alpha(\frac{2n\pi}{L})^2 t} \tag{2.18}$$

It is possible to demonstrate that the coefficients a_0,a_n and b_n depend on the initial conditions i.e. on the temperature profile at $t = 0$ $T(x,0) = f(x)$ as

$$a_0 = \frac{1}{L}\int_{-L/2}^{L/2} f(x)dx \tag{2.19}$$

$$a_n = \frac{2}{L}\int_{-L/2}^{L/2} \cos(\frac{2n\pi}{L}x)f(x)dx \tag{2.20}$$

$$b_n = \frac{2}{L}\int_{-L/2}^{L/2} \sin(\frac{2n\pi}{L}x)f(x)dx \tag{2.21}$$

2.3 FROM MACROSCOPIC TO MICROSCOPIC ANALYSIS: BOLTZMANN TRANSPORT EQUATION

F. These elementary excitations have complete meaning only in the harmonic approximation. However, as it has been amply

demonstrated both theoretically and experimentally, they are well-defined for practical purposes even when they have a finite lifetime (i.e. in an anharmonic crystal or crystal with defects etc.). In equilibrium condition, the phonon system is characterized by the well-known Bose-Einstein thermal equilibrium distribution:

Bose-Einstein equilibrium phonon population

$$\overline{n}_\nu = \frac{1}{\exp(\frac{\hbar\omega_\nu}{K_B T}) - 1} \tag{2.22}$$

where ν indicates ($\mathbf{q}$,s) i.e. the phonon wave vector $\mathbf{q}$ in a specific phonon branch s, while ω_ν is the phonon frequency.

In this scenario, the temperature gradient is a perturbation to the phonon system thermodynamically equilibrated and therefore, in order to describe the system response, we need to introduce a non-equilibrium statistical mechanics analysis.

In particular, to express κ as a function of microscopic quantities, we need the out-of-equilibrium phonon distribution n_ν (with the same ν definition given above) [28]. For small perturbations, this non-equilibrium distribution is linearized around the Bose-Einstein thermal equilibrium distribution i.e.:

$$n_\nu = \overline{n}_\nu(\overline{n}_\nu + 1)\nabla T F_\nu \tag{2.23}$$

where F_ν includes all deviations from equilibrium phonon distribution. Using the microscopic expression of the heat flux, κ can be expressed in terms of microscopic quantities as

$$\kappa = \frac{1}{NV}\sum_\nu \overline{n}_\nu(\overline{n}_\nu + 1)\hbar\omega_\nu v_\nu F_\nu. \tag{2.24}$$

where $\hbar\omega_\nu$ is the phonon energy, v_ν is the projection of the phonon group velocity on the direction parallel to ∇T and NV is the volume of the crystal. The challenge is to find the function F_ν that describes the deviations from equilibrium. In fact, to obtain the out of equilibrium distribution, we have to solve the linearized BTE:

Boltzmann heat transport equation

$$v_\nu \nabla T(\frac{\partial \overline{n}_\nu}{\partial T}) = \sum_{\nu'} \Omega_{\nu,\nu'} n_{\nu'} \tag{2.25}$$

where the scattering operator is represented by a matrix of scattering rates $\Omega_{\nu,\nu'}$, acting on the phonon populations n_ν.

This scattering matrix is built by using phonon-phonon anharmonic processes and all the other scattering rates (isotopic and extrinsic). For simplicity, the BTE is often solved in the single-mode relaxation time approximation (SMA), which relies on the assumption that heat-current is dissipated every time a phonon undergoes a scattering event. In this case $F_\nu = (v_\nu \omega_\nu)^2 \tau_\nu$, where τ_ν is the phonon lifetime i.e. the average time between phonon scattering events at equilibrium. A more complete approach is obtained by solving the exact BTE (Eq.2.25), inverting the scattering matrix $\Omega_{\nu,\nu'}$ [41, 28].

3

COMPUTATIONAL METHODS

3.1 INTRODUCTION TO CLASSIC MOLECULAR DYNAMICS

Classical molecular dynamics is a method, based on statistical mechanics, that is used for computing the equilibrium properties of a many body system by averaging over a set of configurations which are distributed according to some statistical distribution function or statistical ensemble. The successive configurations of the system are generated by following the simultaneous motion of its constituents (molecules, atoms) according to the laws of classical mechanics [63].

Theoretical description of many-body system

In principle, the complete description of a many-body system requires the solution of the time-dependent Schrödinger equation including both degree of freedom of electrons (whose coordinates are $\mathbf{r_j} = \mathbf{r_1}, \mathbf{r_2}, ..., \mathbf{r_{N_e}}$) and nuclei (with coordinates $\mathbf{R_i} = \mathbf{R_1}, \mathbf{R_2}, ..., \mathbf{R_{N_n}}$):

$$H(\mathbf{R_i}, \mathbf{r_j})\Psi(\mathbf{R_i}, \mathbf{r_j}) = E\Psi(\mathbf{R_i}, \mathbf{r_j}) \tag{3.1}$$

where the Hamiltonian operator is expressed by

$$H(\mathbf{R_i}, \mathbf{r_j}) = \mathbf{T_n}(\mathbf{R_i}) + \mathbf{U_{nn}}(\mathbf{R_i}) + \mathbf{T_e}(\mathbf{r_j}) + \mathbf{U_{ee}}(\mathbf{r_j}) + \mathbf{U_{en}}(\mathbf{R_i}, \mathbf{r_j}) \tag{3.2}$$

The labels e and n refer respectively to electrons and nuclei; $i = 1, \cdot\cdot, N_n$ and $j = 1, \cdot\cdot N_e$, where N_n and N_e are the numbers of electrons and nuclei respectively.

The T_n (T_e) operator represents the kinetic energy of the nuclei (electrons). The U_{nn} operator represents the potential energy correspondent to the nucleus-nucleus interactions, U_{ee} the electron-electron interactions and U_{en} the electron-nucleus interactions. Eq.3.1 however cannot be solved exactly for systems consisting of more than two electrons. Hence, to study the dynamics of the vast majority of chemical systems, several approximations have to be imposed. The Born-Oppenheimer or

adiabatic approximation states that the nuclear and electronic motions can be treated separately. This is based on the observation that the ratio between the electronic and the nuclear mass is small. The electrons can instantaneously adapt their wavefunction to the nuclear positions. The nuclear coordinates appear as parameters in the electronic Hamiltonian and the nuclei are considered "frozen" in their positions. In this way we can separate the Schröedinger equation into two different equations. One is for the electrons and depends parametrically on the nuclear coordinates:

The Born-Oppenheimer or adiabatic approximation

$$H_e(\mathbf{R}_i, \mathbf{r}_j)\psi(\mathbf{R}_i, \mathbf{r}_j) = E_e(\mathbf{R}_i)\psi(\mathbf{R}_i, \mathbf{r}_j) \tag{3.3}$$

The other is for the nuclei:

$$[T_n(\mathbf{R}_i) + E_e(\mathbf{R}_i)]\phi(\mathbf{R}_i) = E\phi(\mathbf{R}_i) \tag{3.4}$$

where the eigenvalue $E_e(\mathbf{R_i})$, calculated from Eq.3.3, plays the role of the potential energy for the nuclear motion. Since the nuclei are sufficiently heavy particles the quantum effects on their motion are negligible and they can be considered as classical particles. In this way Eq.3.4 can be substituted by the classical Newton equation of motion:

$$M\ddot{\mathbf{R}}_i = -\frac{dE_e(\mathbf{R_i})}{d\mathbf{R_i}} \tag{3.5}$$

The forces acting on the nuclei are obtained as the negative of the gradients of the potential energy, and the time evolution of the system is determined by integrating these equations of motion.

A this point it is essential to evaluate the potential $E_e(\mathbf{R_i})$. In principle one should solve the electronic Schröedinger equation (Eq.3.3) in order to obtain the potential, and this is the approach followed by the first principles (or *ab initio*) methods. Instead classical molecular dynamics simplifies the problem by using empiric potentials which are functions of the atomic positions and depend on parameters that fit, as accurately as possible, experimental data or first principles calculations (see below).

To start a molecular dynamics simulation, the first step is the initialization of the atomic positions and velocities. The atomic

positions should be chosen compatibly with the structure which has to be studied often by initial placing the particles in a specific lattice.

Description of a molecular dynamics program

The initial velocities can be chosen randomly (usually according to the Maxwell-Boltzmann distribution) in order to reproduce the desired initial temperature.

After the initialization, the forces acting on every atom have to be calculated.This is the most time consuming part of the molecular dynamics simulation. For example, if we consider only the interaction between a particle and the nearest image of another particle for a system of N atoms, this implies $N \times (N-1)/2$ evaluation of distances. Therefore the time needed for force evaluation scale as N^2. There exist some efficient techniques to speed up the procedure in such a way that the simulation time scales as N instead of N^2.

The next step is to calculate the coordinates and the velocities of the atomsat future times by integrating the equations of motions. Due to the complicated nature of the potential energy of the system (which is a function of the positions of all of the atoms), there is no analytical solution. Therefore the only way of evolving the system in time is to solve numerically the equations of motion.

Time is partitioned in intervals of appropriate length which are usually called time steps. In principle it is desirable to have long time steps in order to observe the system for a long time. However, if the time step is too long, there is a risk that the system will deviate from its true evolution. In general the time-step must be chosen small enough to sample the fastest vibrational mode in the system. Typical time steps for classical molecular dynamics are in the order of 1 femtosecond.

There are many different algorithms used to integrate the equations of motion, in the following I will describe the most popular. The Verlet algorithm is the most simple and popular integration algorithm used in molecular dynamics [64]. The derivation

Velocity Verlet algorithm

of the Verlet algorithm starts from the Taylor expansion of the coordinate of a particle around time t:

$$\mathbf{R}(t+\Delta t) = \mathbf{R}(t) + \mathbf{v}(t)\Delta t + \frac{\mathbf{F}(t)}{2M}\Delta t^2 + \frac{1}{6}b(t)\Delta t^3 + O(\Delta t^4) \quad (3.6)$$

where $\mathbf{v}(t)$ is the velocity, $\mathbf{F}(t)$ is the force, M is the particle mass, $b(t)$ is the third derivative of the particle position with respect to time and Δt is the time step. Similarly:

$$\mathbf{R}(t-\Delta t) = \mathbf{R}(t) - \mathbf{v}(t)\Delta t + \frac{\mathbf{F}(t)}{2M}\Delta t^2 - \frac{1}{6}b(t)\Delta t^3 + O(\Delta t^4) \quad (3.7)$$

The sum of these two equations is:

$$\mathbf{R}(t+\Delta t) + \mathbf{R}(t-\Delta t) = 2\mathbf{R}(t) + \frac{\mathbf{F}(t)}{M}\Delta t^2 + O(\Delta t^4) \quad (3.8)$$

$$\mathbf{R}(t+\Delta t) \simeq 2\mathbf{R}(t) - \mathbf{R}(t-\Delta t) + \frac{\mathbf{F}(t)}{M}\Delta t^2$$

The new positions are estimated with an error of order Δt^4. In order to calculate the new positions, the Verlet algorithm does not need to compute the velocities. The velocities can be obtained from knowledge of the trajectory:

$$\mathbf{v}(t) = \frac{\mathbf{R}(t+\Delta t) - \mathbf{R}(t-\Delta t)}{2\Delta t} + O(\Delta t^2) \quad (3.9)$$

Hence velocities are only accurate to order Δt^2.

There are several algorithms which are equivalent to the Verlet one. An example is the so called Leap Frog algorithm [65], which evaluates the velocities at half integer time steps and uses these velocities to compute the new positions. In such a way, this algorithm allows the evaluation of the velocities with a greater precision than the Verlet algorithm. However, the disadvantage for both methods is that the velocities are not calculated at the same time as the positions. As a consequence kinetic and potential energy are not defined at the same instant. The velocity Verlet algorithm solves this problem by calculating positions and velocities at equal times:

$$\mathbf{R}(t+\Delta t) = \mathbf{R}(t) + \Delta t\mathbf{v}(t) + \Delta t^2\frac{\mathbf{F}(t)}{2M} \quad (3.10)$$

$$\mathbf{v}(t+\Delta t) = \mathbf{v}(t) + \Delta t\mathbf{F}(t+\Delta t) + \frac{\mathbf{F}(t)}{2M} \quad (3.11)$$

It is obvious that a good molecular dynamics program requires a good algorithm to integrate Newton's equations.

Interatomic empirical potentials

Another issue which crucially determines the reliability of the molecular dynamic simulations is the choose of the rules governing interaction of atoms in the system. Classical molecular dynamics, in fact, is based on the use of force fields which contain all the information necessary to calculate the forces and energies [63]. A force field consists of:

a) A simple analytic model of the interatomic potential energy (IP) with contributions from processes such as the stretching of the bonds, the bending of the angles and the torsion about bonds. For all these contributions the energy is a function of the particles coordinates, so it is correlated to the structure.

b) A series of parameters used to build the potential energy function.

c) Characteristics of the building blocks of the molecule such as atom types, containing information about the hybridization state and the local environment of an atom.

One could assume a functional form for the potential function and then choose the parameters to reproduce a set of experimental data, as in the case of the so-called empirical interatomic potential (EIP), or in addition the potential functions could be derived from quantum-mechanical arguments (sometimes referred to as semi-empirical potential).

Generally, the energy of N interacting particles may be written as:

$$E = \sum_{i=1}^{N} V_i(\mathbf{R_i}) + \sum_{i<j} \mathbf{V_2}(\mathbf{R_i}, \mathbf{R_j}) + \sum_{i<j} \sum_{j<l} \mathbf{V_3}(\mathbf{R_i}, \mathbf{R_j}, \mathbf{R_l}) + \cdots \tag{3.12}$$

where V_m is called m-body potential, while the first (one body) term corresponds to an external potential. The simplest model of IP is the pair potential, such as the Lennard-Jones and the exponential Morse. Such potentials can be directly applied to a completely arbitrary configuration of atoms but do not accurately describe any but the simplest closed-shell systems. In particular, pair potentials are completely inapplicable to strongly

covalent systems. Moreover, even by considering three-body potentials, a wide range of bonding geometries can not be described.

As an alternative, a new approach to construct an accurate and tractable potential, could be not based on a traditional many-body expansion of energy but on a parametrized bond order function, used to introduce many-body effects and chemical bonding into a pair potential. In fact, beginning with a local basis of unperturbed atomic orbitals, the chemical bending energy E_b can be expressed as a sum over nearest neighbors:

$$E_b = \sum_i \sum_{j>i} f^C_{i,j}[a_{i,j} V^R(\mathbf{R}_{i,j}) - b_{i,j} V^A(\mathbf{R}_{i,j})] \tag{3.13}$$

where $V^R(\mathbf{R_{i,j}})$ and $V^A(\mathbf{R_{i,j}})$ are pair-additive interatomic repulsive and attractive interaction, respectively. $f^C_{i,j}$ is a cut-off function that ensures only nearest-neighbors interactions. The quantity $\mathbf{R}_{i,j} = \mathbf{R}_i - \mathbf{R}_j$ is the distance between pairs of atoms i and j which are nearest-neighbor, and b_{ij} is the corresponding bond order. In particular, this last $b_{ij} \sim N^{-(1/2)}$, where N is the local coordination number, predicting an increase in bond length and a decrease in individual bond energy as coordination increases.

The most commonly used EIPs for Carbon-based material, such as diamond, graphite, graphene and hydrocarbons are those developed by Tersoff[66] and Brenner[67, 68, 69]. The convenience of the Tersoff and Brenner EIPs comes from their rather simple, analytical forms and the short range of atomic interactions.

In the Tersoff potential, for example the functional forms of interatomic interactions are $V^R(R_{i,j}) = A \exp -\lambda_1 R_{i,j}$ and $V^A(R_{i,j}) = B \exp -\lambda_2 R_{i,j}$, while the analytic parametrized forms for the bond order depends both on the local coordination around atom i and on bond angles $\theta_{i,j,k}$ between atoms i, j and k:

Empirical bond order Tersoff potential

$$b_{i,j} = (1 + \beta^n \zeta^n_{i,j})^{-\frac{1}{2n}} \tag{3.14}$$

$$\zeta_{i,j} = \sum_{k \neq i,j} f^C_{i,j} g_{i,j,k} \exp \lambda_3^3 (\mathbf{R}_{i,j} - \mathbf{R}_{j,k})^3 \tag{3.15}$$

where $f^C_{i,j}$ has the same definition given above and $g_{i,j,k}$ is a bond-bending spline function defined as:

$$g_{i,j,k} = 1 + \frac{c^2}{d^2} - \frac{c^2}{d^2 + (h - \cos[\theta_{i,j,k}])^2} \tag{3.16}$$

All the parameters $(A, \lambda_1, B, \lambda_2, \beta, \lambda_3, c, d, h, n)$ present in the equations have been empirically fitted. The angle term allows the Tersoff potential to describe the strong covalent bond that occurs in carbon system and to be compatible with different carbon bonds geometry, such as tetrahedral in diamond and 120° tribonded in graphene.

Reactive Empirical Bond Order potential

On the other side, Brenner developed the so called Reactive Empirical Bond Order potential (REBO). I will expose the second generation version of this potential, that includes both modified analytic functions for the intramolecular interactions and an expanded fitting database, especially though with the aim of modeling hydrocarbon materials.

In this second generation potential, the form of the interaction functions are

$$V^R(\mathbf{R}_{i,j}) = (1 + \frac{Q}{\mathbf{R}_{i,j}})A \exp -\alpha \mathbf{R}_{i,j} \tag{3.17}$$

$$V^A(\mathbf{R}_{i,j}) = \sum_{n=1}^{3} B_n \exp -\lambda_n \mathbf{R}_{i,j} \tag{3.18}$$

and bond order term:

$$\bar{b}_{i,j} = \frac{1}{2}[b_{i,j}^{\sigma-\pi} + b_{j,i}^{\sigma-\pi}] + \Pi_{i,j}^{RC} + b_{i,j}^{DH} \tag{3.19}$$

$$b_{j,i}^{\sigma-\pi} = (1 + \sum_{k \neq i,j} f_{i,k}^{C} g_{i,j,k})^{-1/2} \tag{3.20}$$

$$g_{i,j,k} = \sum_{i=0}^{5} \beta_i \cos^i[\theta_{i,j,k}] \tag{3.21}$$

$$b_{i,j}^{DH} = \frac{T_0}{2} \sum_{k,l \neq i,j} f_{i,k}^{C} f_{j,l}^{C} (1 - \cos^i[\Theta_{i,j,k,l}]) \tag{3.22}$$

$$\cos[\Theta_{i,j,k,l}] = \prime\prime_{j,i,k} \cdot \prime\prime_{i,j,l} \tag{3.23}$$

$$\eta_{j,i,k} = \frac{\mathbf{R}_{i,j} \times \mathbf{R}_{j,k}}{|\mathbf{R}_{i,j}||\mathbf{R}_{j,k}|} \sin[\theta_{i,j,k}] \tag{3.24}$$

No predetermined atomic hybridizations are assumed as in traditional force fields; atomic bonding is determined, indeed, from

local bonding neighbors and non-local conjugation i.e. not only by considering the number of neighbors one atom has, but also if it belongs to a conjugate system. This makes this potential particularly suitable to simulate atomic rehybridization as well as covalent bonds break.

As in Tersoff case, $b_{j,i}^{\sigma-\pi}$ depends on the local coordination of atoms around atom i and the angle $\theta_{i,j,k}$ between atoms i, j and k. The coefficients β_i in the bond-bending spline function Eq.3.21 were fit to experimental data for graphite and diamond. The value of the term $\Pi_{i,j}^{RC}$ depends on whether a bond between atoms i and j has radical character and is part of a conjugated system, while $b_{i,j}^{DH}$ depends on the dihedral angle Θ_{ijkl} for carbon-carbon double bonds. This dihedral bending function that depends on the local conjugation and is zero for diamond is instead very important for describing graphene. It involves third nearest-neighbor atoms and is given by Eq.3.22 where T_0 is a parameter and Θ_{ijkl} is given by Eq.3.23. $''_{jikl}$ and $''_{ijlr}$ are unit vectors normal to the triangles formed by the atoms given by the subscripts. In flat graphene, the dihedral angle, Θ_{ijkl}, is either 0 or π and the dihedral term is subsequently zero.

Thus, an accurate description of the lattice dynamics is critically important in modeling the lattice thermal conductivities of SWCNTs and graphene. The original parameter sets of the Tersoff and Brenner EIPs do not accurately reproduce the phonon dispersions of graphene, as has been noted previously. In particular, they do not accurately obtain the velocities of the three acoustic branches near the center of the Brillouin zone.

Lindsay and Broido presented in Ref. [34] an optimized parameter sets for the Tersoff and Brenner EIPs, which better represent the lattice dynamical properties of graphene. In detail, implementing a χ^2 procedure, they fitted the force field parameters giving greatest importance to the phonon frequencies and the velocity in the near-zone-center acoustic branches, in order to improve the potential accuracy in the transport phenomena description. These optimized parameters for the Tersoff and Brenner potentials have been demonstrated to improve the agreement between the calculated ZA, TA and LA phonon branches

in graphene and in-plane graphite. Based on this, we expect that they will also provide better representation of the lattice dynamics and of phonon thermal transport in graphene, graphene nanoribbons, and graphane. For this reasons, in the works I present in this thesis, I always refer to this optimized version of Tersoff and REBO interatomic potentials.

3.2 SIMULATING THERMODYNAMICAL ENSAMBLE BY MEANS OF MD

The previously explained mechanical formulation of MD can be naturally recast into a statistical mechanics formulation. In fact, the set of instantaneous particle positions $\mathbf{R_1}, \mathbf{R_2}, ...\mathbf{R_N}$ and velocities $\mathbf{v_1}, \mathbf{v_2}, ...\mathbf{v_N}$ uniquely define a microstate $\Gamma(t)$ in the 6N-dimensional phase space of the system. Generating trajectories is therefore equivalent to generate the time evolution of the microstate in the corresponding phase space. This is the basic ingredient for developing a theory based on statistical mechanics.

Let us consider a given system property (or observable) and let us define the corresponding microscopic (i.e. computable on the basis of particle positions and/or velocities) operator O. Then, if we know the microstate Γ we can evaluate the instantaneous operator value $O(\Gamma(t))$. In other words, we can compute the value assumed by the observable when the system is in that given microstate at time t. According to statistical mechanics, we therefore define the macroscopic (i.e. the experimentally measurable) value O_{macro} to be the time average $\langle O(t)\rangle_{t_{obs}}$.

$$O_{macro} = \langle O(t)\rangle_{t_{obs}} = \frac{1}{t_{obs}} \int_0^{t_{obs}} O(\Gamma(t))dt \tag{3.25}$$

where the time integral is performed over the observation time t_{obs}. In practice, the molecular dynamics run is performed over a finite number N_{steps} of time steps, so that

$$O_{macro} = \langle O(t)\rangle_{obs} = \frac{1}{t_{obs}} \sum_{i=0}^{N_{step}} O(\Gamma(t_i)) \tag{3.26}$$

The major conceptual steps explained above allow to set up the iterative scheme shown in Fig.3.1. This scheme permits to generate by computer simulation the time evolution of a system on which an observation procedure is performed.

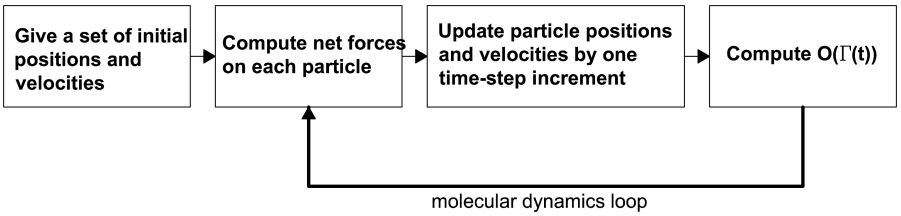

Figure 3.1: Iterative molecular dynamics loop which includes the evaluation of the instantaneous value of $O(\Gamma(t))$ of a given observable. One iteration corresponds to increasing time by an amount δt.

In order to implement the procedure, it needs just to choose the proper thermodynamical ensembles where time averages are performed and operationally select a subset of the phase space compatible with the imposed conditions of temperature, pressure (or stress), volume and so on. This formulation widely enlarges the playground for MD investigations of condensed-matter systems to including nearly any possible thermodynamical condition.

According to statical mechanics, keeping the system into the canonical ensemble means coupling it to an external thermal reservoir. Several algorithms are available to implement this concept.

Defining a canonical ensamble in MD simulation

If the temperature at time t is $T(t)$, multiplying the velocity by a factor λ will produce a temperature change:

$$T_{new} - T(t) = \Delta T = (\lambda^2 - 1)T(t) \tag{3.27}$$

Therefore the simplest way to control the temperature is to multiply the velocities at each time step by $\lambda = \sqrt{\frac{T_{req}}{T_{curr}}}$, where T_{req} is the required temperature and T_{curr} is the current temperature. A different approach adopted is the Nosé algorithm. This Nosé method is based on the use of an extended Lagrangian, containing fictitious coordinates and velocities additional to the

particle ones. In order to mimick the coupling to a thermal reservoir, a new fictitious degree of freedom s is added to the system and a classical Lagrangian is written as

$$L_{Nose} = \frac{1}{2}\sum_{\alpha=1}^{N} m_\alpha s^2 \dot{\mathbf{R}}_\alpha^2 + \frac{1}{2} m_s \dot{s}^2 - U(\mathbf{R}_1, ...\mathbf{R}_N) - g K_B T \ln s \tag{3.28}$$

where m_s acts as the effective mass associated to the new coordinate s and g is the number of degrees of freedom for the extended system. The Nosé Lagrangian allows for energy (i.e. heat) exchange between the physical system and the reservoir (described by s), the thermal inertia being described by the parameter m_s.

Nosé and Nosé-Hoover thermalization methods

The new extended system (i.e. The N particles plus the thermal bath) is microcanonical, while it can be proved that ensemble averages performed during a Nosé MD run reduce to canonical averages. The Nosé method can be generalized into the Nosé-Hoover chains approach: the original thermostat is now coupled to a series of other fictitious thermostas whose role is basically to allow for fluctuations of the variable s. The Nosé-Hoover method is proved to accurately generate a canonical distribution and to improve the ergodicity of the simulated system. In the next works I always use this two kinds of constant temperature algorithms.

After the explanation given above about the molecular dynamics simulations basic concepts, I would like now to explore how to use it to measure interesting properties of many-body systems. To measure an observable quantity in a molecular dynamics simulation, we have first of all to express it as a function of the positions and momenta of the particles of the system. Among the properties of the system that we can calculate by using an MD code there are:

- the thermodinamical properties such as temperature, pressure and heat capacity;
- the functions which characterize the local structure of the system, such as the radial distribution function;
- dynamic equilibrium properties.

As far as concerned temperature operative definition in molecular dynamics simulation, a convenient expression for T is used, based on the energy equipartition in classical many-body systems with N particles. This rapresents the link between classical mechanics and thermodynamics:

Operative temperature definition in MD simulation

$$T(t) = \sum_{i=1}^{N} \frac{m_i v_i(t)^2}{K_B N_f} \tag{3.29}$$

where N_f is the degrees of freedom (= 3N-1 for a system with fixed momentum). Since the total kinetic energy of a system fluctuates, to get an accurate estimate of the temperature, one should average over many fluctuations. The relative temperature fluctuations will be of order $\frac{1}{\sqrt{N}}$.

3.3 SYNOPSIS OF METHODS TO CALCULATE κ AND PHONON PROPERTIES BY MEANS OF MD

In the Section 2.1, I have previously exposed the thermal conductivity operative definition as well as its importance on the characterization of a material thermal behavior. In this Section, I will summarize the possible strategies used to calculate κ by using MD simulations. The two most popular techniques to model the heat transport by MD are equilibrium molecular dynamics (EMD) and non equilibrium (NEMD) or "direct" method. The first [70, 71] calculates the thermal conductivity at temperature T, in the framework of linear-response theory of transport coefficients, by using Green-Kubo formula:

Thermal conductivity evaluation by means of equilibrium Green-Kubo approach

$$\kappa_{\alpha\beta} = (k_B T^2 V)^{-1} \int_0^{+\infty} \langle \mathbf{J}_\alpha(t) \mathbf{J}_\beta(0) \rangle \, dt \tag{3.30}$$

where $\mathbf{J}_\alpha$ is the heat flux vector in the α direction, K_B is the Boltzmann constant, V is the system Volume and $\langle\rangle$ denotes the ensamble average. This approach, which can be used in different transport phenomena, is based on statistical mechanics fluctuation-dissipation theorem which relates a non-equilibrium transport coefficient (κ in the case of heat transport) to the equilibrium system properties trough the autocorrelation functions

of some specific variables (in this case heat fluxes). The advantages of the equilibrium method is that it allows to compute the full conductivity tensor from one simulation and that it does not suffer from severe finite size effects as NEMD (see after), mainly because in EMD the phonons are not strongly scattered by the boundaries of the simulation box. The main drawback is intrinsic to the method, as we need to probe small thermal fluctuations around equilibrium over long time scales, several statistical averages over different initial conditions are required. In addition, very long time needed to converge the current-current autocorrelation function. It has been recently shown [72] that as many as $O(10^6)$ atoms and several hundred thousands MD time-steps are indeed necessary to provide a fully converged value of lattice thermal conductivity in a system such as bulk crystalline silicon.

NEMD[73] instead, calculates κ in analogy to the experimental measurement, i.e. by means of the Fourier law (Eq.2.2) where the external perturbation and the system response are separately computed, eventually getting the thermal conductivity as the response-to-perturbation ratio:

Thermal conductivity evaluation by means of non equilibrium direct method

$$\kappa_{\alpha\beta} = - \lim_{\frac{\partial T}{\partial x_\beta} \to 0} \lim_{t \to +\infty} \frac{\langle \mathbf{J}_\alpha(t) \rangle}{\frac{\partial T}{\partial x_\beta}} \tag{3.31}$$

Practically, a thermal gradient is established by thermostating the two opposite terminal layers of a finite-thickness slab at different temperatures T_{cold} and T_{hot}, while its inner part is evolved microcanonically (see Fig.3.2). After a long enough simulation, a steady state thermal gradient is so generated and $\frac{\partial T}{\partial x}$ and J_x are computed.

This NEMD implementation is generally known as "direct method" of computing κ, in contrary of "inverse" Müller-Plate method[51]. This last reverses the usual cause and effect picture, by imposing an heat flux on the system and eventually measuring the temperature gradient from the simulation. More in detail, the periodically-repeated simulation box is divided into N_s slabs. Slab 0 is defined as the hot slab and slab $N_s/2$ is the cold slab. The heat flux is generated by exchanging the kinetic energy between the hottest atom in the cold slab and the coldest atom

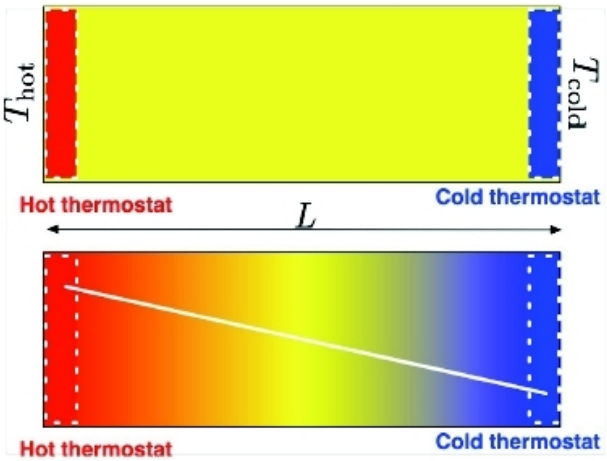

Figure 3.2: Schematic representation of NEMD "direct" method. The two opposite edges of a finite-thickness sample are termalized at T_{cold} and T_{hot} and a linear temperature gradient is established.

Thermal conductivity evaluation by means of non equilibrium Müller-Plate method

in the hot slab in order to decrease the temperature in the cold slab and increase it in the hot one. After a suitable number of exchanges, a non equilibrium steady state is eventually reached and both $\langle \mathbf{J}_x(t) \rangle$ and $\frac{\partial T}{\partial x}$ are easily computed. In order to calculate temperature gradient generally it is necessary to avoid the external regions, in which non-linear temperature profile is created as due to the non-Newtonian nature of the heat transfer (see Fig.3.3).

NEMD methods are mainly limited by the very long simulation time needed to establish a steady state condition, once that a given temperature gradient or heat current is imposed, with an advantage in the case of Müller and Plate technique which requires the sampling of rapidly converging temperature gradient rather than slowly converging heat flux.

Approach to equilibrium molecular dynamics

In order to overstep these limitations, in ref.[53, 74], the new AEMD approach is proposed, in which the simulation is performed in a transient thermal conduction regime. The method has been fully exploited to investigate the thermal transport properties of disordered and nanostructured silicon samples [52].

The two simulation cell halves are separately equilibrated in order to obtain an initial Heaviside-step temperature profile. The left side of the simulation cell is firstly equilibrated at T_1 by

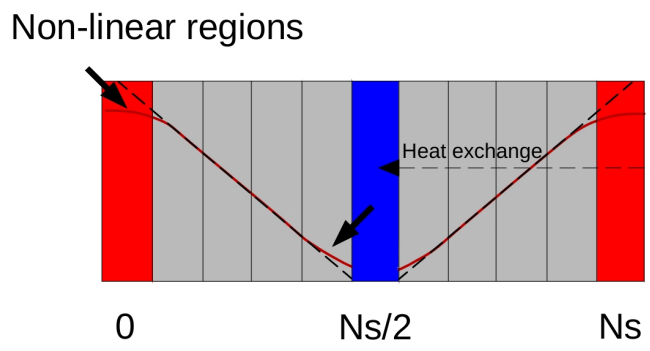

Figure 3.3: Schematic representation of the Müller and Plate method. The sample is divided in N slots and a flux exchange between the slot 0 and $N_{s/2}$ generates the showed temperature profile (black line) along the sample. The lateral regions presents non-linear profiles as effect of the artificial heat exchange.

keeping frozen all the atoms belonging to the right side. Then the same procedure is performed by equilibrating the right side at $T_2 < T_1$ and by keeping frozen the left side. In Fig.3.4 I show by stick and ball representation the simulation cell upon which the step-like temperature profile is imposed. The color map represents the different atomic temperatures showing a lower average temperature T_2 for the right side with respect to the left side temperature T_1.

The system is eventually left free to reach the thermal equilibrium under microcanonical (NVE) constraints. Therefore the total energy is conserved, and the system could reach an average temperature determined by the ratio of the total mass times the heat capacity of the two materials. The ensemble-averaged instantaneous temperature of each subsystem is recorded during the simulation and the decay of the temperature difference $\Delta T = T_1 - T_2$ can be estimated.

The formula

$$T(x,t) = a_0 + \sum_{n=1}^{\infty} [a_n \cos(\frac{2n\pi}{L}x) + b_n \mathrm{sen}(\frac{2n\pi}{L}x)] e^{-\alpha(\frac{2n\pi}{L})^2 t} \tag{3.32}$$

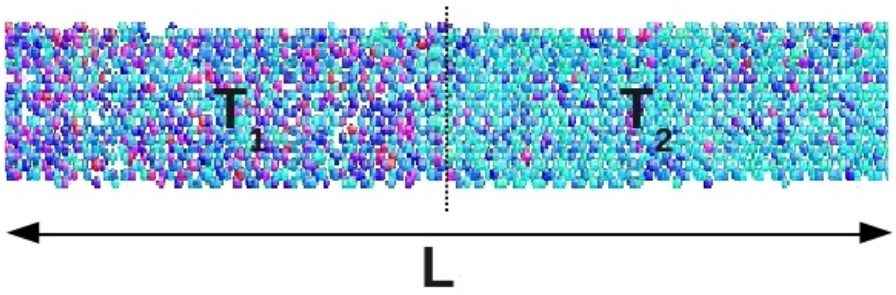

Figure 3.4: Simulation cell stick and ball representation together with color map showing the atomic temperatures along the sample. The right side average temperature T_2 is lower with respect to the left side temperature T_1.

can be calculated for the specific case of an initial temperature profile $T(x,0)$ having the shape of an Heaviside step function $H(x)$ as in the simulation:
$H(x) = T_1$ for $-L/2 < x < 0$
$H(x) = T_2$ for $0 < x < L/2$
We consider an interval for the x coordinate $I = [-L/2, L/2]$ with periodic-boundary conditions $T(-L/2,t) = T(L/2,t)$ and $T_x(-L/2,t) = T_x(L/2,t)$. In this case for the coefficients a_0,a_n and b_n we have:

$$a_0 = \frac{1}{L}\int_{-L/2}^{L/2} H(x)dx = \frac{T_1 - T_2}{2} \tag{3.33}$$

$$a_n = \frac{2}{L}\int_{-L/2}^{L/2} \cos(\frac{2n\pi}{L}x)H(x)dx \tag{3.34}$$
$$= \frac{2}{L}[\frac{L}{2n\pi}T_1 \sin(\frac{2n\pi}{L}x)]_{-L/2}^{0} + \frac{2}{L}[\frac{L}{2n\pi}T_2 \sin(\frac{2n\pi}{L}x)]_{0}^{L/2} = 0$$

$$b_n = \frac{2}{L}\int_{-L/2}^{L/2} \sin(\frac{2n\pi}{L}x)H(x)dx \tag{3.35}$$
$$= \frac{2}{L}[\frac{L}{2n\pi}T_1(-\cos(\frac{2n\pi}{L}x))]_{-L/2}^{0} + \frac{2}{L}[\frac{L}{2n\pi}T_2(-\cos(\frac{2n\pi}{L}x))]_{0}^{L/2}$$
$$= [(\frac{1}{2n\pi}\cos(2n\pi)(T_1 - T_2) + (T_2 - T_1)]$$

We can also estimate the time evolution of the temperature difference $\Delta T = T_1 - T_2$. We have that:

$$T_1 = \frac{2}{L}\int_{-L/2}^{0} T(x,t)dx \tag{3.36}$$

$$T_2 = \frac{2}{L}\int_{0}^{L/2} T(x,t)dx \tag{3.37}$$

and therefore:

$$\Delta T = \sum_{n=1}^{\infty} \frac{b_n}{\pi n}(2\cos(2\pi n) - 2)e^{-\frac{n^2\pi^2\alpha t}{L^2}} \tag{3.38}$$

Fig.3.5 shows the time evolution of the temperature profile $T(x,t)$ during the AEMD simulation on a graphene sample with L=500 nm and $\Delta T(0)$=200 K. We notice the same qualitative behavior as described by the analytical solutions (black lines) of the heat equation derived above. Starting from the initial Heaviside-step function the temperature profile evolves towards the first harmonic corresponding, reaching the constant value equal to the average $(T_2 + T_1)/2$. We can estimate the thermal diffusivity α of our system by fitting the numerical ΔT_{sim} with the analytical solution in Eq.3.38. Finally, using the so computed α we can calculate κ by using the formula $\alpha = \frac{\kappa}{C_V \rho}$. C_V is the volumetric heat capacity and in some cases, it can be approximated with the Dulong e Petit classic heat capacity (see Appendix).

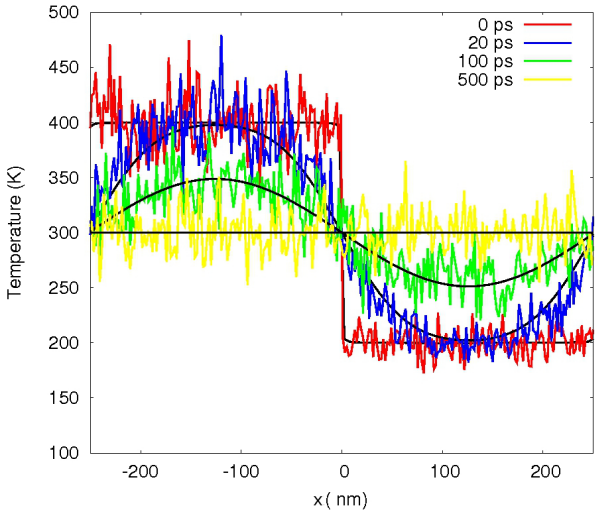

Figure 3.5: Temperature profile calculated in an AEMD simulation on a graphene sample at different time-steps (t=0, 20, 100, 500 ps) together with the corresponding analytical solutions.

Solving the Fourier heat equation to obtain Eq.3.38, we have assumed that κ is not dependent on the x position. Actually, in AEMD simulations, this assumption is indeed not strictly satisfied since κ is actually a function of temperature, which is in turn a function of x. However, in Ref.[74] has been proved that

by performing simulations where the initial temperature differences $\Delta T(0)$ between the hot and cold regions are different, no significant variation has been observed in the κ computed. For example Fig.3.6 (taken from Ref.[74]) shows κ calculated in the case of crystalline silicon sample, at six different initial $\Delta T(0)$ namely: 50 K, 100 K, 150 K, 200 K, 250 K and 300 K. No meaningful κ dependence on $\Delta T(0)$ has been observed. From one perspective, large initial temperature differences are favored since increasing $\Delta T(0)$ the error significantly decreases (see in Fig.3.6 the κ convergence to the value 18.5 ± 0.1 $Wm^{-1}K^{-1}$ for $\Delta T(0)$ greater than 150 K). On the other side, it needs to remark that Fourier heat equation is valid under the assumption of small temperature gradient in order to ensure the validity of linear response regime.

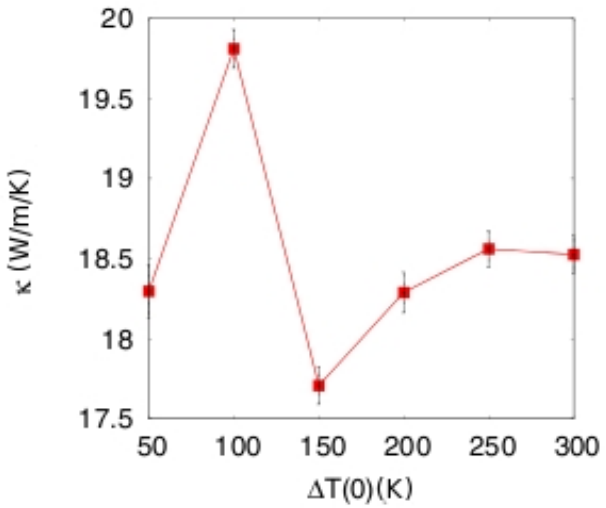

Figure 3.6: κ in a crystalline silicon sample with L=108.61 nm as function of the initial temperature difference between the hot and cold regions $\Delta T(0)$.

3.4 PHONON PROPERTIES DERIVED FROM MD SIMULATIONS

A very effective method for deriving phonon dispersion curves and vibrational density of states, valid for finite temperatures, is through molecular dynamics simulations of the modelled material. This method has certain advantages; anharmonic interactions between atoms are implicitly taken into account, since it is

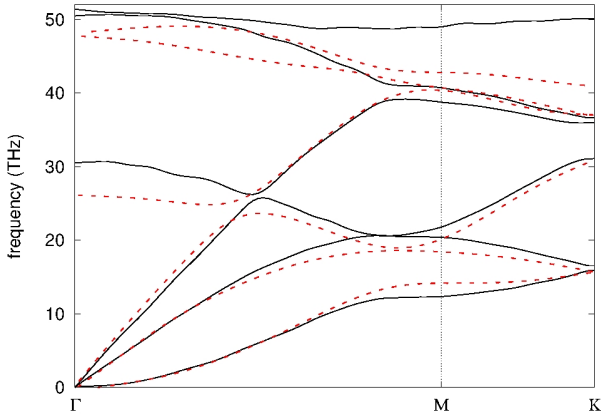

Figure 3.7: Comparison between phonon dispersions in graphene calculated with DFT (dashed red line) and REBO potential (solid black line)

based on processing of the atomic trajectories. Phonon frequencies are calculated by diagonalizing the dynamical matrix computed from molecular dynamics simulations based on fluctuation-dissipation theory for a group of atoms. In particular, we consider a crystal with N unit cells. Each unit cell contains K basis atoms labeled with the index $k = 1, 2, \cdots K$. Instead of calculating effective spring constants between individual atoms in real space, it is more efficient to assess the effective elastic coupling in reciprocal space.

Phonon dispersion based on Green's functions calculation

If $\mathbf{u}_{n,k}$ is a displacement vector of the atom k in the nth cell with equilibrium position $R^0_{n,k}$ in real space, its Fourier transform is defined as

$$\tilde{\mathbf{u}}_k(\mathbf{q}) = \frac{1}{\sqrt{N}} \sum_n \mathbf{u}_{n,k} exp(\mathbf{q}\mathbf{R}^0_{n,k}) \tag{3.39}$$

Based on fluctuation-dissipation theory, the force constant coefficients of the system in reciprocal space are given by [75**?**]

$$\Theta_{k\alpha,k'\beta}(\mathbf{q}) = K_B T \mathbf{G}^{-1}_{k\alpha,k'\beta}(\mathbf{q}) \tag{3.40}$$

where G is the Green's functions coefficients defined as

$$G_{k\alpha,k'\beta}(\mathbf{q}) = \langle \tilde{\mathbf{u}}_{k\alpha}(\mathbf{q}) \cdot \tilde{\mathbf{u}}^*_{k'\beta}(\mathbf{q}) \rangle \tag{3.41}$$

where $\langle\rangle$ denotes the ensemble average and $\tilde{\mathbf{u}}_{k\alpha}(\mathbf{q})$ is the α component of the atomic displacement of the kth atom of the unit cell in the q-vector reciprocal space.

In practice, the Green's functions coefficients can also be computed according to the following formula,

$$\mathbf{G}_{k\alpha,k'\beta}(\mathbf{q}) = \langle \mathbf{R}_{k\alpha}(\mathbf{q}) \cdot \mathbf{R}^*_{k'\beta}(\mathbf{q}) \rangle - \langle \mathbf{R} \rangle_{k\alpha}(\mathbf{q}) \cdot \langle \mathbf{R}^* \rangle_{k'\beta}(\mathbf{q}) \quad (3.42)$$

where $\mathbf{R}$ is the instantaneous positions of atoms in the reciprocal space, and $\langle \mathbf{R} \rangle$ is the averaged atomic positions. The inverse of the correlation matrix of atomic displacements divided by the thermal energy can be interpreted as the renormalized force constants in the reciprocal space.

Once the force constant matrix is known, the dynamical matrix D can then be obtained by

$$D_{k\alpha,k'\beta}(\mathbf{q}) = (m_k m'_k)^{-1/2} \Phi_{k\alpha,k'\beta}(\mathbf{q}) \quad (3.43)$$

whose eigenvalues are exactly the phonon frequencies at $\mathbf{q}$.

Applying the method outlined above, I calculate the dispersion curve of graphene by using the REBO potential. In Fig.3.7 the MD graphene phonon dispersions (solid black line) is compared with the ones calculated by *ab-initio* density functional theory (DFT) calculations (dashed red line)[76], testing also the REBO reliability in graphene. We observed a good description of the acoustic branches especially near Γ point. This is important in order to predict the transport properties in which acoustic phonons are mainly involved. On the other side, the REBO potential slightly underestimates the optical bands which are, however, barely involved in thermal transport.

Part III

THERMAL TRANSPORT IN PRISTINE MONOLAYER-GRAPHENE

In this part, I will present my molecular dynamics studies addressing thermal transport in pristine monolayer graphene. In particular, I will show two different developments of AEMD technique focusing on the thermal conductivity estimate. In the Chapter 4, I will disentangle the question about thermal conductivity length dependence. In Chapter 5, indeed, I will analyze the response to a laser thermal excitation in a transient regime, by distinguish the most probably phonon excited modes and decay channels.

4

UPPER LIMIT IN GRAPHENE INTRINSIC THERMAL CONDUCTIVITY

4.1 THEORETICAL INVESTIGATIONS ABOUT THERMAL CONDUCTIVITY IN GRAPHENE: STATE OF ART

As I explained in the previous Chapter 2, theoretical approach used to study graphene thermal transport involves the Boltzmann transport equation (BTE) which relates the overall κ to the material phonon properties, such as phonon equilibrium distribution, specific heat and group velocity. Generally, some approximations are widely used in phonon transport models to solve BTE equation e.g. the relaxation time approximation (RTA) [77, 33] or long-wavelength approximation (LWA) [78, 79, 80]. The former uses an approximated form for the deviation of phonon population with respect to the Bose-Einstein equilibrium distribution (function F_ν in Eq.2.24). In detail, a life-times τ_i for each phonon mode with the corresponding frequency ω_i has been considered, which is additive with respect to the different life-times $\tau_{i,j}$ corresponding to the various scattering processes: $\tau_i^{-1} = \sum_j \tau_{i,j}^{-1}$. On the other side, in the LWA the solid is represented as an elastic continuum in which acoustic branches with small frequencies are included.

RTA and LWA approximations in solving BTE

The potential anharmonicity permits phonon-phonon scatterings which are of two kinds: Normal scatterings (N) with wavevector conservation and Umklapp scatterings (U) with a momentum lose. These last actually provide heat flux dissipation. In Fig.4.1 the two kinds of phonon-phonon scattering are schematically shown: in N processes two initial phonons with wave vectors $\mathbf{q}_1$ and $\mathbf{q}_2$ create a phonon with wave vector $\mathbf{q}_3$, which is the vectorial sum of $\mathbf{q}_1$ and $\mathbf{q}_2$, while in U processes, the resulting momentum $\mathbf{q}_3$ is outside the first Brillouin zone, and

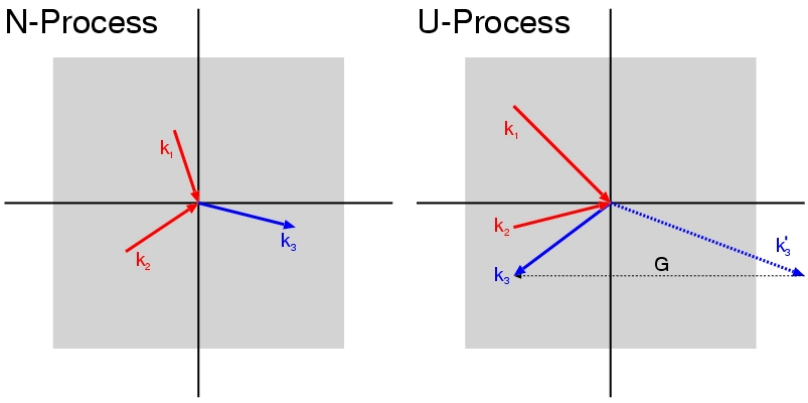

Figure 4.1: Schematic representation of Normal scattering N and Umklapp scattering U.

therefor is equivalent to a wave vector $\mathbf{q}_3'$ summed with a reciprocal lattice vector G.

Even if momentum conserving nature of N processes prevents them from dissipating heat-current, they are involved in transport phenomena in terms of rearrangement of phonon distribution and therefore they are fundamental in the estimation of the correct transport properties, included thermal conductivity evaluation.

Both the approximations cited before experience troubles in distinguish between Normal and Umklapp events. Moreover, these approximations totally neglect the right selection rule for three-phonon scatterings [30, 81], which has fundamental effects on graphene thermal transport by reducing the phase space of allowed scattering processes and then critically affecting the phonon population distribution.

Exact solution of BTE: complete scattering matrix

More rigorous approaches have been implemented to solve these problems. They are based on the exact solution of BTE, by taking into account the whole scattering matrix [41, 30] (see Chapter 2). In this latter, the only inputs to the calculation are harmonic and anharmonic interatomic force constants (IFC). The first enter in the dynamical matrix, which is the one used to compute phonon dispersions $\omega(\mathbf{q})$, while the second in the phonon-phonon scattering matrix to calculate phonon life-time $\tau(\mathbf{q})$. The IFC could be calculated using a force field [29], generally Tersoff

or Reactive Empirical Bond Order (REBO) potential (see Chapter 3), or by first principles approach (DFT or DFPT) [30].

In the framework of molecular dynamics simulations, EMD calculates the thermal conductivity κ at temperature T along a given x direction by using the equilibrium fluctuations of the heat current vector $\mathbf{J}$ through the current-current autocorrelation function [42]. NEMD, [45] instead, calculates κ in analogy to the experimental steady-state measurement, i.e. by means of the Fourier law and separately computing the external perturbation $\partial T/\partial x$ and the system response J_x (more in particular in Chapter 3).

Classification of different transport regimes

Finally, I want to underline that to analyze transport, especially in the specific case of 2D materials, it is important to distinguish between different phonon transport regimes. Here I report the different regimes classification according to the nomenclature of Guyer [82]. In the ballistic regime, the extrinsic scatterings with sample edges, grain boundaries and other defects dominate with respect to the phonon-phonon interactions. In the Poiseuille regime the N scattering events start to dominate even if the boundaries scatterings are still present. Differently, in the Ziman regime the N scatterings sustain the heat flux which is dissipated by resistive scatterings (U). Finally, in the kinetic regime intrinsic resistive processes (U) have highest probability.

4.2 THERMAL CONDUCTIVITY LENGTH DEPENDENCE

An exotic feature of graphene thermal transport, which has been predicted by several theoretical works [33, 41, 34, 45] and recently experimentally observed[43], is the κ dependence on the sample length L_x in the direction of the temperature gradient. At the moment different interpretations for such a κ length-dependence behaviour have been supplied. In molecular dynamics methods [42], the $\kappa(L_x)$ dependence is due to the simulations cell finiteness which hinders phonons having mean free path (MFP) greater than the actual cell length L_x. In principle, a reliable description of the intrinsic thermal conductivity, needs to achieve the diffusive regime by increasing the simula-

Simulating ballistic and diffusive transport regimes

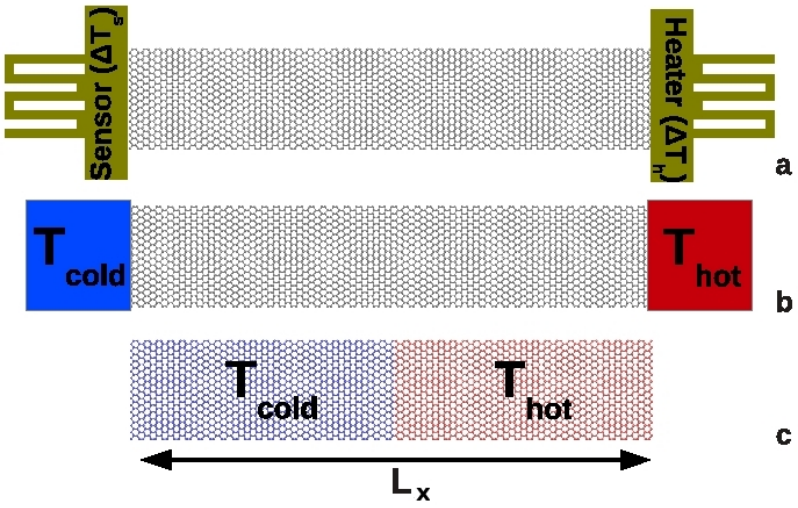

Figure 4.2: Schematic representation of the characteristic length L_x in case of different methodologies: (a) experimental thermal resistance measures [43]; (b) NEMD simulations [45]; (c) AEMD simulations [1].

tion cell length up to a critical length L_{diff}. L_{diff} is the length at which all the phonons become diffusive, which in graphene is reported to range between 1-10 µm [31]. In the case of non equilibrium molecular dynamics, besides the previously described phenomenon, the $\kappa(L_x)$ dependence is strengthen by the presence of the thermostats at the sample boundaries, which artificially scatter phonons [45] (see Fig.4.2).

Graphene thermal conductivity length dependence in LWA

On the other side in LWA approximations such as Klemens-like models, the $\kappa(L_x)$ dependence is artificially included by construction, through the low-frequencies cut-off $\omega_{min} \propto \sqrt{\frac{1}{L_x}}$ [77]. ω_{min} was first introduced by Klemens in the case of graphite, where the heat transport is approximately two-dimensional until a low-bound frequency, under which a strong coupling with cross-plane phonon modes appears and heat starts to propagate non only in the graphite planes but in all the directions. To adapt the thermal transport description given for graphite to graphene, in which the transport is intrinsically 2D even for small phonon frequencies, the low-bound cut-off ω_{min} in graphene is determined by the condition that the MFP cannot exceed the physical size L_x of the sample.

RTA approximation, on the other side, does not give any sizeable L_x dependence of κ, due to a Normal scattering overestimate.

As far as concerned the exact BTE solution, an empirical length-dependent rate is introduced to count boundary scatterings in a finite size sample [30].

Graphene thermal conductivity length dependence in experiments

Recently, a further evidence of thermal conductivity size dependence has been experimentally shown [43] by performing thermal resistance measurements on suspended single-layer graphene samples. In detail, a single-layer graphene was suspended between two SiN membranes, one used as an heater resistor R_h and other as a sensor R_s to measure the temperature rise at the end of the sample (see Fig.4.2). A μA-DC current was applied to R_h to produce Joule heat and therefore to increase the temperature with respect to the environment. In the meanwhile, an AC current is used to measure the resistance of the same R_h. The produced Joule heating gradually dissipates through the graphene sheet resulting in a temperature rise in the sensor resistor R_s. In the steady state, the thermal conductivity of the graphene sheet can be obtained by measuring the temperature rise in the R_h and R_s and the Joule heat Q_h applied to the heater.

A $\kappa(L_x)$ logarithmic dependence was observed for sample lengths up to 9 μm. I point out that no other experimental measures have been performed for longer length scales.

Fig.4.2 shows a schematic representation of the characteristic length L_x in the case of different methodologies. In the experimental thermal resistance measures (a) L_x is the sample length suspended between the two resistors [43]. In NEMD simulations (b), the L_x corresponds to the distance between the thermostats which artificially scatter the phonons [45]. In the AEMD simulation L_x is the actual cell dimension along x.

Extrapolation of graphene thermal conductivity for infinite sample

Even if both experiments and theory agree on the actual κ length-dependence, an active debate about a possible divergence of thermal conductivity for $L_x \to \infty$ is still open. In particular, theoretical models taking into account only in-plane phonon modes (i.e. by disregarding out-of-plane flexural modes), predict a $\kappa(L_x)$ logarithmic divergence at room temperature [77].

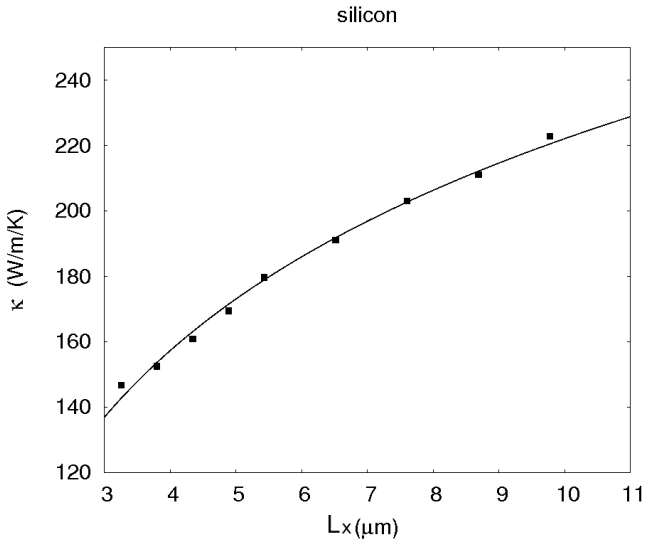

Figure 4.3: $\kappa(L_x)$ trend in Silicum up to L_x=10μm.

In fact, I have already cited in Introduction the importance of ZA modes in graphene since a non reliable description of thermal transport is obtained in the case in which these are not considered. In Ref.[43] the logarithmic divergence has been suggested based on NEMD and experiments performed on sample lengths up to 9 μm. The actual κ divergence was interpreted as due to the 2D nature phonons and their non equilibrium distribution. In particular, the authors showed that the differences in phonon populations between non equilibrium condition (such as NEMD) with respect to the equilibrium populations (EMD), promote the κ logarithmic divergence. However, the observed $k(L_x)$ logaritmic trend in lengths range up to 9 μm does not necessarily imply a divergent thermal conductivity for $L_x \to \infty$. For example, in the same length range, the logaritmic behavior is observed, by means of AEMD simulations with Tersoff empirical potential, even for a very well-known 3D material as Silicum (see Fig.4.3). This probably suggests that this $k(L_x)$ dependence, at least in the case of AEMD calculations, is not related to the particularity of 2D graphene nature, but it is indeed due to the specific regime in which the measures are performed.

The conclusions based on general arguments valid for 2D systems has been questioned in the specific case of graphene.

On the other side, in Ref.[41] it has been argued that, even by assuming $\kappa = \kappa(L_x)$ as due to a regime of ballistic phonon transport in samples with $L_x < L_{diff}$, an upper limit for thermal conductivity should be anyhow reached for long enough samples ($L_x > L_{diff}$), where a fully diffusive regime can be eventually reached. It has also been calculated that such a diffusive regime is reached only for mm-long samples that can accommodate not only single-phonon with typical MFP of $\sim$ 1 μm [31] but even collective excitations. They suggest the evidence of an hydrodynamic regime, in which how I explained before, the main phonon scattering mechanisms are the N events. The heat transport in this case is characterized by the creation of phonon packets that conserve to a large extend their momentum. Therefore, the typical heat diffusive behavior is altered until L_x is lower than the MFPs of these collective phonon excitations which are typically $\sim$ 100 μm [41]. The actual occurrence of a truly diffusive regime in mm-long systems has not yet been confirmed since both experiments and MD simulations (of any kind) explored so far much smaller samples.

4.3 AEMD SIMULATION ON INCREASING LENGTH GRAPHENE SAMPLES

In the work [1], I elucidate the present dilemma by performing "approach to equilibrium molecular dynamics" (AEMD) [74] simulations (see Chapter 3) on pristine graphene samples having L_x up to the unprecedent size of 0.1 mm. Our final goal is to unequivocally state whether an actual κ vs L_x divergence is present or whether a saturation occurs, revealing a diffusive regime achievement. The predicted behavior could be also a motivation to perform experimental measures for samples in this length-scale no yet explored.

4.3.1 *Computational details*

All the simulations presented in this Chapter are performed by using "Reactive Empirical Bond Order" (REBO) potential in its second generation form [68], whose reliability for graphene has been tested by comparing the graphene phonon dispersions with the ones calculated by ab-initio density functional theory (DFT) calculations as it has been shown in Chapter 3. Equations of motion are integrated by the velocity Verlet algorithm with 1.0 fs time-step. Thermal conductivities have been evaluated by fitting the computed time-dependent temperature difference between the left and the right side of the sample $\Delta T(t)_C$, recorded during a microcanonical run, with the analytical one $\Delta T(t)_A$. In particular, an initial temperature gradient has been imposed $\Delta T(0)$=200 K by thermalizing half of te sample at T_1=400 K and the other T_2=200 K by means of an atomic velocity rescaling performed every simulation step. We pointed out that the final results are independent on the initial ΔT in a range of 100-400 K, as it has been previously generally demonstrated as far as concerned AEMD methodology[52] (see Chapter 3). The fitting parameter is the thermal diffusivity α. The corresponding thermal conductivity has been evaluated as $\kappa = \alpha \rho C_V$.
In this work, we decided to use quantum corrections on the calculation of specific heat, C_V, in order to take into account the deviations from the Maxwell-Boltzmann distribution at room tempertaure, that is for graphene considerably below Debye temperature Θ_D (see Appendix).

I calculated graphene thermal conductivity on thirteen samples having periodically repeated simulation cells along the x and y directions (see Fig.4.2) with fixed lateral width L_y and length 0.83 $\mu m \leqslant L_z \leqslant$ 100 μm. The periodic boundary conditions enable to simulate an infinite sample in the lateral direction. The corresponding simulation cell spanned the range 24000-2880000 atoms, requiring different simulation times for the AEMD analysis extending from 0.411 ns to 10 ns.

With the aim of limiting the huge computational cost of MD simulations on such a mm-long samples, we had to reduce the

samples lateral size. In order to do this we at first needed to explore the $\kappa(L_y)$ dependence for a fixed L_x (for example I choose L_x=125.1 nm). In fact, Fig.4.4 demonstrates the κ independence on the sample width for L_x greater than 2.2 nm.

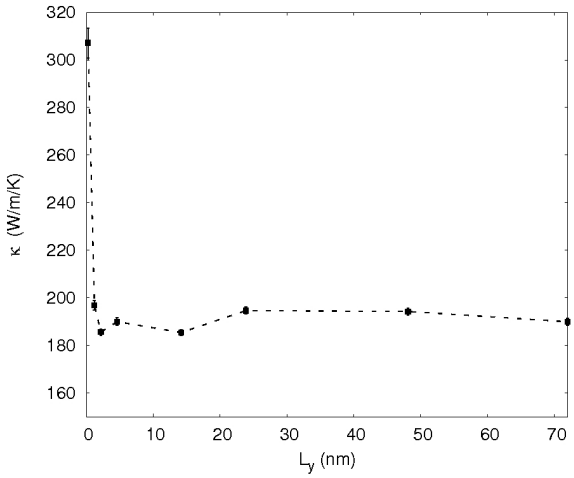

Figure 4.4: κ vs L_y for fixed L_x=125.1 nm and $\Delta T(0)$=200 K. The κ value is basically independent on the cross section for $L_x > 2.2$ nm.

Basing on this assumption, I initially calculated κ on samples having L_x=0.7 nm, and by means of a specific fitting function I estimated the corresponding κ values for L_x=2.2 nm. In detail, I compared the κ estimated values on 5 samples having $0.834\ \mu m \leqslant L_x \leqslant 20\ \mu m$ for both L_{y1}=0.7 and L_{y2}=2.2 nm. The ratio $R(L_x) = \frac{\kappa_{Ly1}}{\kappa_{Ly2}}$ have been calculated and fitted by means of the suitable function $f(L_x) = A * L_x^{0.4} + C$. The corresponding $R(L_x)$ values for $L_x > 20\ \mu m$ have been then extrapolated. Fig.4.5 represents the calculated values of $R(L_x)$ together with the corresponding fitting function.

In fact, for $L_x > 20\ \mu m$ we calculated κ_{Ly1} in samples with later size L_{y1}=0.7 nm and after we extrapolate κ_{Ly2} (which corresponds to the saturation thermal conductivity value with lateral dimension) by considering $R(L_x) \times \kappa_{Ly1}$. By means of the precedent procedure we are enable to reach simulations cell length for graphene that has never been atomistically described before.

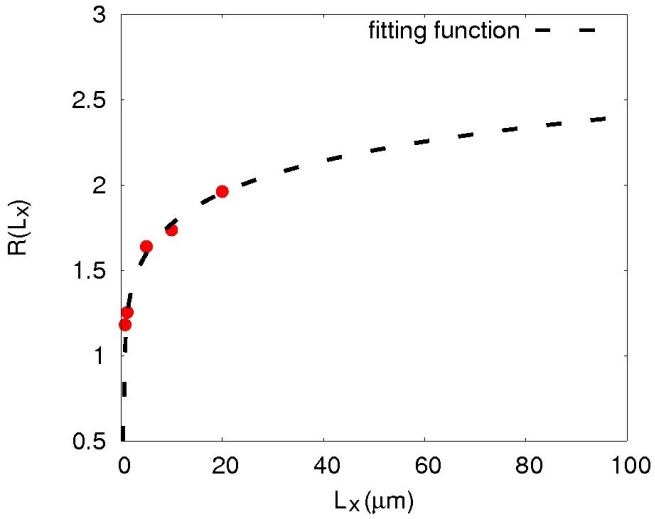

Figure 4.5: Calculated $R(L_x)$ values (red dots) together with the corresponding fitting function $f(x) = A * x^{0.4} + C$ (dashed black line). The fitting function has been used to extrapolate the κ values for L_{y2}=2.2 nm and $L_x > 20$ μm.

4.3.2 *Results and comparisons*

Graphene thermal conductivity length dependence: state of the art

In Fig.4.6 I compare our results with other works addressed to investigate the $\kappa(L_x)$ dependence both theoretically, by using NEMD with Rebo and Tersoff empirical potentials, and experimentally [45, 43]. I point out that the REBO potential strongly underestimate the overall κ values, both in the case of AEMD and NEMD calculations, with respect to DFT and Tersoff potential. However a perfect agreement is shown between our values and NEMD results which use the same Rebo potential, giving another prove of the AEMD technique reliability.

All the results are in agreement in to predict a logarithmic $\kappa(L_x)$ behavior in the length range up to 10 μm.

In order to asses that the κ absolute value differences have not physical reasons and depend only on the empirical potential chosen, in Fig.4.7 we compare our κ with experimental measures as normalized to their corresponding value calculated for a reference sample with L_x=10 μm. The overall agreement in the κ-vs-L_x trend is really remarkable, providing a convincing evidence about the reliability of the present simulations.

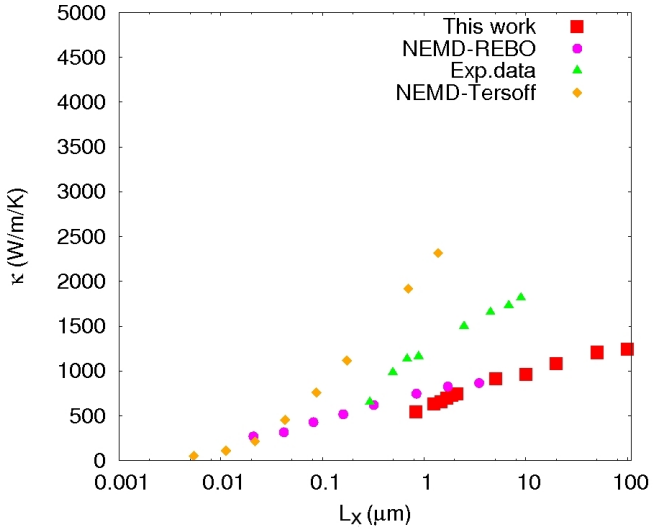

Figure 4.6: Thermal conductivity $\kappa(L_x)$ of monolayer graphene for increasing sample dimension L_x. Red squares: present AEMD results. Yellow diamonds: NEMD data taken from Ref.[43]. Magenta dots: NEMD data taken from Ref.[45]. Green triangles: experimental data taken from Ref.[43].

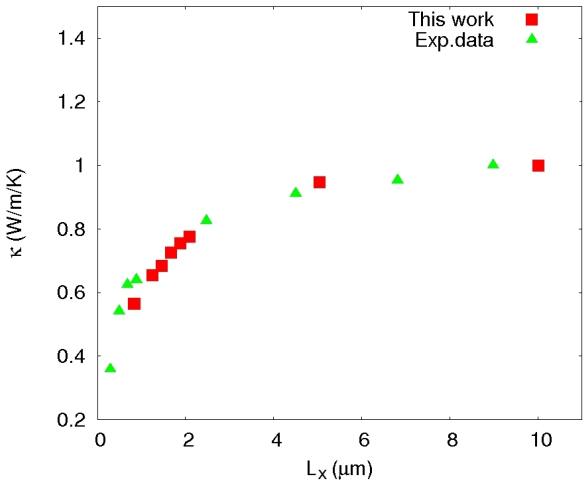

Figure 4.7: Comparison of our results with experimental data. Red squares: present AEMD results. Green triangles: experimental data taken from Ref.[43]. All thermal conductivity values are normalized to $\kappa(10\mu m)$, corresponding to a sample with size L_x=10 μm.

Since the only estimation of κ for sample dimensions greater than ~ 50 μm are based on the extract *ab initio* solution of the BTE [41], I directly compare AEMD and BTE results in Fig.4.8, in which, motivated by the previously described REBO potential

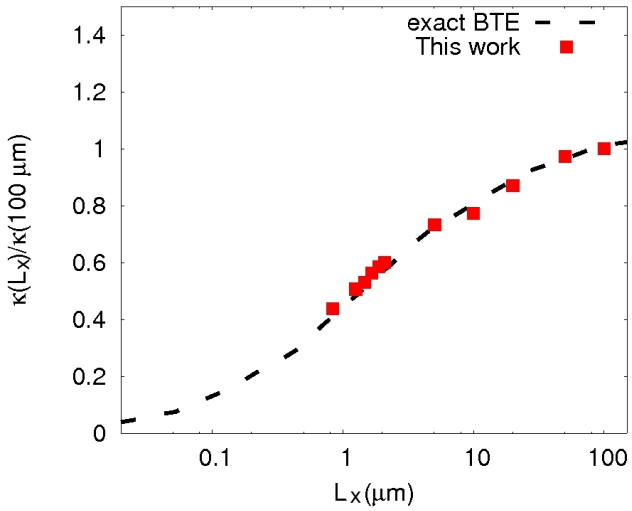

Figure 4.8: Thermal conductivity $\kappa(L_x)$ of monolayer graphene for increasing sample dimension L_x. Red squares: present AEMD results. Black dashed line: exact solution of BTE provided in Ref.[41]. For sake of comparison, all thermal conductivity values are normalized to $\kappa(100\mu m)$, corresponding to a sample with size L_x=100 μm.

limitation, I report both sets of κ data as normalized to their corresponding value calculated for a reference sample with L_x=100 μm.

In Ref.[41] the linearized BTE has been exactly solved by considering the complete matrix of scattering rates acting on the out of equilibrium phonon distribution, in which the inter-atomic force constants have been calculated by DFT. As far as concerned the extrinsic scattering with boundaries in a finite sample of length L_x, they introduced a rate proportional to $1/L_x$. The main result of this work is to state that in graphene, even at room temperature, collective hydrodynamic modes dominate the transport. These collective phonon excitations are characterized by comparatively larger MFP than single-phonon ones (λ=100 μm instead of 800 nm).

Fig.4.8 further confirms the reliability of our approach in the description of the κ-vs-L_x trend. The fact that two independent calculations of rather different nature predict the same saturation

trand provide clear evidence that $\kappa(L_x)$ has indeed an ultimate upper limit.

This result also confirms the assumption of Ref.[41] which identifies the importance of collective modes to properly define the critical sample length governing the ballistic-to-diffusive transport transition.

Moreover, Fig.4.8 shows that the $\kappa(L_x)$ trend change at L_x=0.1 mm, indicating that in this length range transport in graphene approaches to become diffusive. Even from this point of view, we are in quite agreement with Ref.[41], which indicates as the critical sample length above which is observed a truly diffusive phonon transport regime L_{diff}=1 mm.

Recent Monte Carlo simulations upon graphene samples in micron-range, proved that the ballistic-to-diffusive crossover is captured for a sample length of 0.1 mm [**?**]. More in detail, they used a full-dispersion phonon Monte Carlo simulation technique, which involves a stochastic solution to the phonon Boltzmann transport equation with the relevant scattering mechanisms (edge, three-phonon, isotope, and grain boundary scattering) taking into account the dispersion of all three acoustic phonon branches that are calculated from the fourth-nearest-neighbor dynamical matrix. This enable an efficient transport description (including inelastic and elastic scattering, as well as enabling the incorporation of real-space edge features) with an accurate account of phonon dispersions. The authors shown a thermal conductivity increase with increasing length up to 100 μm and they proved that 20% of phonons involved in heat transport have MFP longer than this length and more than 10% longer than 200 μm.

The length dependence which is empirically modelled in previous theoretical works, is actually directly observed in our calculations without any *a priori* assumption. Unfortunately for the big simulation effort, we could not further increase our sample size, and for this reason we could not obtain the intrinsic thermal conductivity absolute value.

In any case, even if Fig.4.6 does show a $\kappa \sim \log L_x$ trend in the range 1 μm $\leqslant L_x \leqslant$ 10 μm in agreement with the experi-

mental evidence [43], such a logarithmic dependence does not imply any divergent thermal conductivity for $L_x \to \infty$. The claimed $\kappa \sim \log L_x$ divergence does not in fact occur in our calculation. This could be due to the fundamental role of out-of-plane oscillations in graphene thermal transport. Interesting enough, this conclusion is fully consistent with EMD simulations [42], where such out-of plane modes were artificially hindered showing that, under such a condition, a divergence of κ-vs-L_x is indeed found.

In conclusion, these results are the first direct evidence that κ in graphene is upper limited and underlines that a reliable measure of thermal conductivity value needs samples long enough to allow pure diffusive heat transport either for single and for collective phonon excitations. Moreover, they suggest that the experimental measures conducted in smaller samples have been performed in a quasi-ballistic regime and therefore they could not estimate the upper limit of intrinsic graphene thermal conductivity.

I

5

HEAT PROPAGATION IN TRANSIENT REGIME IN GRAPHENE

5.1 COMPARISON BETWEEN MOLECULAR DYNAMICS AND EXPERIMENTAL RESULTS

I have previously underlined the wide interval of reported values for thermal conductivity in graphene, ranging from 600 to 5000 $Wm^{-1}K^{-1}$ [8, 9, 39, 83, 38], as due to the difference in the measurement techniques as well as different sample qualities related to the presence of defects, thickness non-uniformity, strain distribution and sample temperature. As far as it concerns the experimental investigations, I want to stress now their division into two different categories, respectively addressing a steady state or a transient thermal conduction regime. Optothermal micro-Raman spectroscopy belongs to the first category, where κ is estimated by measuring the Raman G peak shift due to a local temperature rise in response to heating [8, 9, 83] (see Introduction). Alternatively, temperature is measured by thermocouples and thermal bridges [38]. On the other side, methods addressed to a transient regime such as 3-ω technique, heat spreader methods [39] and pulsed laser-assisted thermal relaxation technique (PLTR) [40] measure thermal gradient as a function of time, enabling fast measurements of the thermal diffusivity α over large T ranges. The specific heat C_V and mass density ρ have to be determined independently to calculate κ since $\kappa = \alpha\rho C_V$.

Steady state or transient experimental investigations

I have also summarized the many theoretical models numerically implemented to compute κ [34, 41, 30]. In particular, equilibrium and non-equilibrium molecular dynamics (MD) simulations have been performed with this aim [42, 43]. Non-equilibrium MD is comparable to an experiment performed in a steady state regime, while approach to equilibrium MD (AEMD) [52], which

is based on the analysis of the system evolution towards equilibrium upon a thermal perturbation, is comparable to an experiment performed in a transient regime.

Both experimental methods rely on electrical means for supplying heating power and measuring T [43, 39, 38] or alternatively the power is provided by means of optical sources [8, 9, 83]. Recently, the thermal diffusivity of few-layer graphene has been measured by using a noncontact optical microscopy transient method based on a mode mismatched thermal lens technique in a pump-probe two-laser beams configuration [84] (see Introduction). Actually, these non-contact laser-based transient techniques are particularly suitable to investigate deviations from a purely diffusive thermal transport, which could lead to a non-Fourier description of the sample dynamical response to a heat pulse. In particular, the evidence of that kind of anomalous behavior has been recently argued in Ref.[41], where it has been guessed that in such materials as graphene, graphane and boron nitride at room temperature the typical diffusive behavior of heat is altered. In fact, in this case, the phonon gas experience the so-called hydrodynamic regime, similarly to the case of an ideal gas where particles scatter without dissipating momentum. Phonons in hydrodynamic regime form wave-packets which conserve to a large extent their momentum, leading to heat propagation by wave-like motion. This kind of effect is called "second sounds" and it has been observed experimentally just at cryogenic temperature (less than 100 K) in solid Helium [85] and in some dielectric solids such as Bi [86] and NaF [87]. In detail, second sound is a quantum mechanical phenomenon in which heat transfer occurs by dumped wave, rather than by the more usual mechanism of diffusion. Heat takes the place of pressure in normal sound waves. This leads to a very high thermal conductivity. It is known as "second sound" because the wave motion of heat is similar to the propagation of sound in air.

Evidence of second sounds: hydrodynamic regime

5.2 AEMD ON A RADIAL GEOMETRY GRAPHENE SAMPLE

5.2.1 *Method*

In order to disentangle this topic, I focus in this Chapter on the characterization by MD simulations of the transient response to a pulsed laser focused on a free standing graphene layer. In particular, we directly observe by atomistic simulations the time evolution of the temperature profile initially generated by the laser pulse by taking into account different phonon-mode excitations and their subsequent relaxation toward the equilibrium distribution.

In the paper [4], indeed, I performed AEMD simulations in a pristine circular graphene sample with radius R_{sample}=248.1 nm (see Fig.5.1) and a total number of atoms as large as 7192979. The heat absorption due to a laser spot focused in the centre of the sample has been mimicked by thermalizing a central concentric region with radius R_{spot}=49.6 nm.

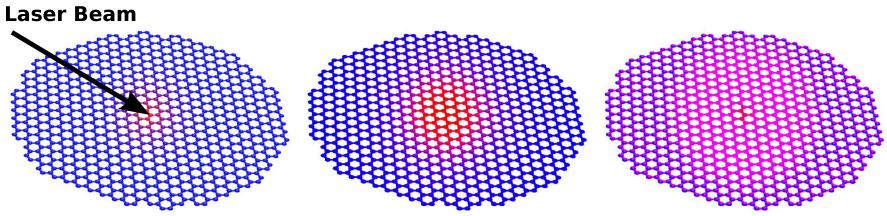

Figure 5.1: Schematic representation of the temperature time evolution in a circular graphene sample. At t=0 (left) a central circular spot has been heated-up mimicking a pulsed laser assisted laser experiment.

In particular, R_{sample}, R_{spot} as well as their ratio have been chosen as in Ref.[8] where the graphene thermal conductivity has been measured for the first time by optothermal Raman spectroscopy.

All the simulations have been performed by using Tersoff empirical potential which has been optimized to describe phonon thermal transport in graphene. The equations of motion have been integrated by the velocity Verlet algorithm with 1.0 fs timestep (see Chapter 3).

I studied the system at two different initial temperatures $T_1^{(0)}$=100 K and $T_2^{(0)}$=300 K by thermalizing the whole sample by means of the Nosé-Hoover thermostat using a damping parameter of 100.0 fs for 55 ps. In both cases, an initial step-like temperature profile has eventually been imposed by thermalizing the central spot at $T_{1,spot}^{(0)}$=115 K and $T_{2,spot}^{(0)}$=345 K, respectively for other 55 ps. Next the system was aged in a microcanonical run during which the radial temperature profile was recorded until the temperature was uniformly distributed along the sample. The overall procedure has typically taken about 20 ps. In order to reduce the numerical noise, I chose a suitable combination of time and space-average on temperature profiles. In detail, the temperature has been recorded on 10000 concentric rings of increasing radius and then averaged-out every 40 rings resulting in a profile with 250 points. We further time-averaged the temperatures every 1 ps in such a way to preserve the information concerning its time evolution and to reduce the noise, obtaining a temperature profile $T_{sim}(R_i, t)$ with $1 \leqslant i \leqslant 250$.

Fourier heat equation in radial simmetry

The heat transport in the transient condition is described through the radial heat equation:

$$\frac{\partial^2 T(r,t)}{\partial^2 r} + \frac{1}{r}\frac{\partial T(r,t)}{\partial r} = \frac{C_V \rho}{\kappa}\frac{\partial T(r,t)}{\partial t} \tag{5.1}$$

I numerically solved Eq.5.1 obtaining the temperature profile $T_{theo}(R,t)$. By fitting $T_{sim}(R_i,t)$ with $T_{theo}(R,t)$ we extract the system thermal diffusivity α and the thermal conductivity κ.

The fitting procedure used is based on the minimization of the χ^2 function:

$$\chi^2 = \sum_{i,t} p_i^2 (T_{sim}(R_i,t) - T_{theo}(R_i,t))^2 \tag{5.2}$$

in which i is the ring index and t the simulation time step. In $T_{theo}(R_i,t)$ is included the κ parameter that we are interested to calculate trough the χ^2 minimization. Each temperature value $T_{sim}(R_i,t)$ was weighted with $p_i = 1/\sigma_i$ where σ_i is the corresponding standard deviation of temperature which depends on the number of atoms N_i contained in each ring as $\sigma_i \sim \frac{1}{\sqrt{N_i}}$. For first, I analyzed the dependence of error in the ring temperature on the number of atoms N_i contained in that ring to

obtain the constant of proportionality in the previous relation. By performing a canonical (NVT) run, I just recorded the temperature fluctuation during 10000 time steps at both $T_1^{(0)}$=100 K and $T_2^{(0)}$=300 K in each ring without any perturbation i.e. with no laser beam excitation. The average temperature, as well as the temperature standard deviation σ_i for each ring has been then calculated. Fig.5.2 shows, for example, the σ_i VS N_i behavior in the case $T_1^{(0)}$=100 K. Data have been fitted by the function $f(x) = a\frac{1}{\sqrt{x}}$, in order to obtain a. The same procedure has been repeated for $T_2^{(0)}$=300 K. By using the so-obtained weights p_i and by means of the χ^2 minimization technique, we obtained κ values for both temperatures.

During the fitting procedure, the χ^2 function has been evaluated in a grid of discrete points in order to find its minimum. As far as concerned the errors in the thermal conductivity obtained by the fit procedure, we considered the difference between κ values corresponding to the increment and decrement of the χ^2 minimum by a quantity equal to the grid resolution.

5.2.2 *Results*

Fig.5.3 top (bottom) shows an example of the time evolution of the simulated temperature profile (red symbols) for both cases discussed above, together with the fitted solution of Eq.5.1 $T_{theo}(R,t)$ (black lines). The κ resulting from fitting procedure are 752 ± 6 and 621 ± 5 W m^{-1} K^{-1} in the case of $T_1^{(0)}$=100 K and $T_2^{(0)}$=300 K, respectively.

As a proof of validity of this methodology, I compared these results with the thermal conductivities calculated by means of AEMD method in its standard implementation (see Chapter 3) i.e. by fitting the temperature difference between two sample sides (right and left) in a rectangular geometry instead of the circular one considered in this Chapter. Upon the sample, whose length L=517.8 nm has been chosen similar to the diameter of the precedent samples, an initial step-like temperature profile has been imposed maintaining, of course, the same initial tem-

Comparison with the rectangular geometry

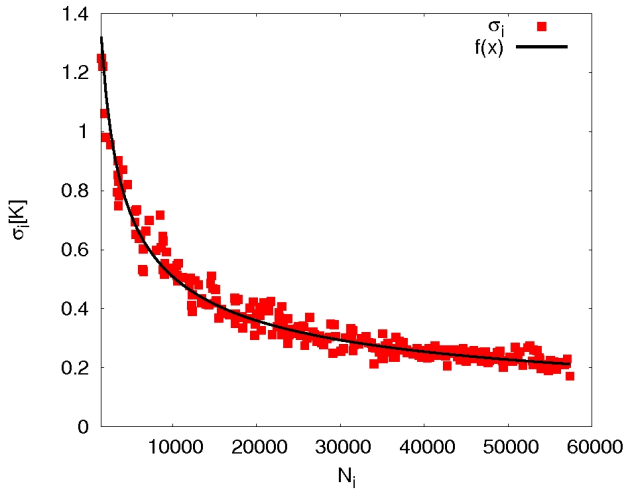

Figure 5.2: Temperature standard deviation σ_i in the i ring calculated in the case of $T_1^{(0)}$=100 K during a canonical run of 10000 time steps versus the number of atoms in the corresponding ring N_i (red squares). Fitting function $f(x) = a\frac{1}{\sqrt{x}}$ (black line).

perature differences ΔT_1=15 K and ΔT_2=45 K for the two cases here considered. The κ obtained are 863 ± 13 and 687 ± 8 in the case of $T_1^{(0)}$=100 K and $T_2^{(0)}$=300 K, respectively, in well agreement with the new method findings.

5.3 SIMULATING A TRANSIENT RESPONSE TO A LASER PULSE

5.3.1 *Method*

Laser photo-excitation and optical phonon modes

A more realistic simulation of the spot heating by a laser pulse must take into account that the laser pulse photo-generates electrons and holes that eventually cool down by interacting with optical phonons [88, 35]. In fact, the laser pulse, depending on the pump photon energy, creates electrons and holes which immediately after photo-excitation, thermalize with each other and with the existing carriers, thereby acquiring Fermi-Dirac distributions with high temperatures. The thermalization times for the photo-excited carriers are supposed to be extremely short and in the 20-40 fs range. The thermalized electron and hole distributions then lose most of their energy to the optical phonons

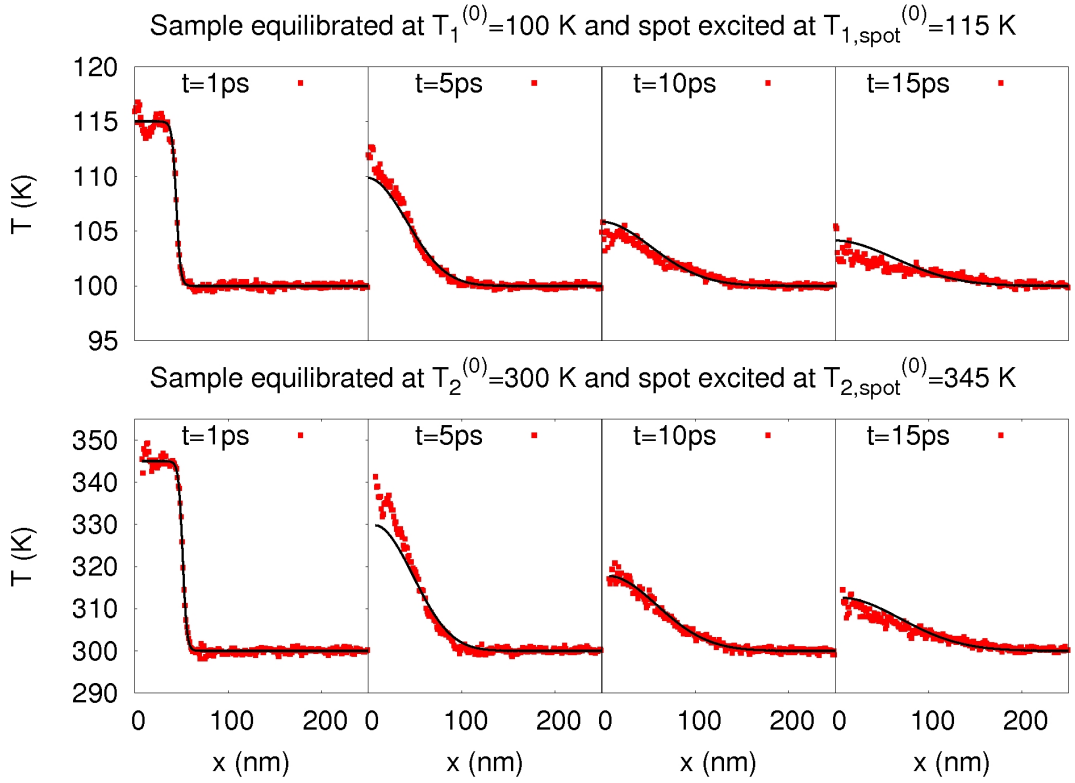

Figure 5.3: Time evolution of the temperature profile for an hot spot at $T^{(0)}_{1,spot}$=115 K (top) and $T^{(0)}_{2,spot}$=345 K (bottom) excited in a sample initially equilibrated at $T^{(0)}_{1}$=100 K (top) and $T^{(0)}_{2}$=300 K (bottom). Red symbols: AEMD simulations. Black lines: solution of the radial heat equation.

in about 500 fs after photo-excitation. For this reason the electron temperature rapidly decreases and correspondingly the phonon temperature rapidly increases. It has been argued that the two phonon modes with the strongest electron-phonon coupling in graphene are the optical $K-A_1'$ and $\Gamma-E_{2g}$ (described in Fig.5.4) at frequencies of 1172 cm^{-1} and 1588 cm^{-1} [89], respectively. In particular, the electron-phonon scatterings can be intravalley in the case of the E_{2g} phonons at Γ point, or intervalley due to the A_1' mode at K point. Optical excitations in fact can induce a non-equilibrium phonon distribution, with significant overpopulation of these phonon modes. Such optical vibrations eventually thermalize into acoustic modes by means of anharmonic phonon-phonon interactions, following different decay channels. Actually, to describe heat transport in the case of a response to a laser pulse, it could be crucial to focus on

the analysis of the anharmonic phonon processes by considering the different decay channels for the modes described above. Moreover, it could be important to compare the overall simulation time, determined for example on the specific features of the experiments considered (sample size, observation time, magnitude of initial perturbation), with the typical phonon anharmonic life-time τ_{ph-ph}. The values of the optical phonon thermalization time, for example, has been estimated of about 7ps in graphite from time-resolved terahertz spectroscopy [90]. While in Ref.[31] they obtained by means of *ab-initio* calculations $\tau_{K-A_1'} \sim 8$ ps at 100 K and ~ 5 at 300 K and $\tau_{E_{2g}} \sim 3.5$ ps at 100 K and little less at 300 K.

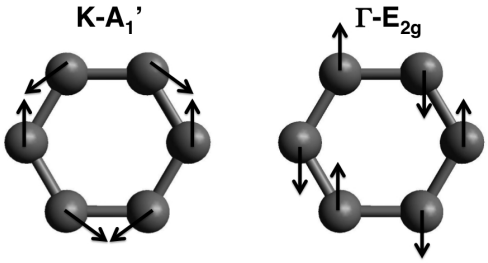

Figure 5.4: Excited atomic displacements corresponding to the K-A_1' and Γ-E_{2g} optical phonon modes.

In order to reproduce such phenomenon starting from the thermalized samples at $T_1^{(0)}$=100 K and $T_2^{(0)}$=300 K , we excited in the spot region just one single optical phonon mode by performing a velocity rescaling (which acts on both the modulus and the direction of the atomic velocities) according to the specific atom displacement pattern of the $K - A_1'$ and $\Gamma - E_{2g}$ modes (shown in Fig.5.4). Fig.5.5 shows what happens in this case when $T_{2,spot}^{(0)}$=345 K. By the following velocity rescaling procedure we are able to actually reach the spot target temperature in 1 ps . In detail, for 1000 time-steps at each current atomic velocity a velocity vector have been added with the specific direction θ corresponding to the pattern in Fig.5.4 and a modulus ϵ.

$$\mathbf{v}_x^{new} = \mathbf{v}_x^{old} + \epsilon cos(\theta) \quad \mathbf{v}_y^{new} = \mathbf{v}_y^{old} + \epsilon sen(\theta) \tag{5.3}$$

This last has been chosen by means of a trial and error approach in such a way that the overall temperature computed

in the spot by averaging the atomic kinetic temperatures of the atoms inside this region reaches the decided value, in this case $T^{(0)}_{2,spot}$=345 K. Fig.5.6 shows the dependence of the $T^{(0)}_{2,spot}$ temperature obtained developing the precedent procedure on the magnitude of the velocity scaling vector ϵ. For example, in this case I choose ϵ=4.21.

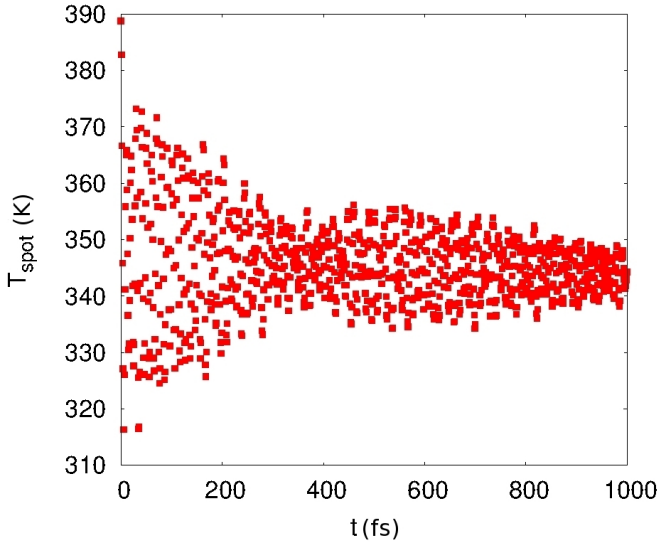

Figure 5.5: $T^{(0)}_{2,spot}$ during the 1 ps of thermalization procedure. The spot temperature reached is 345 K.

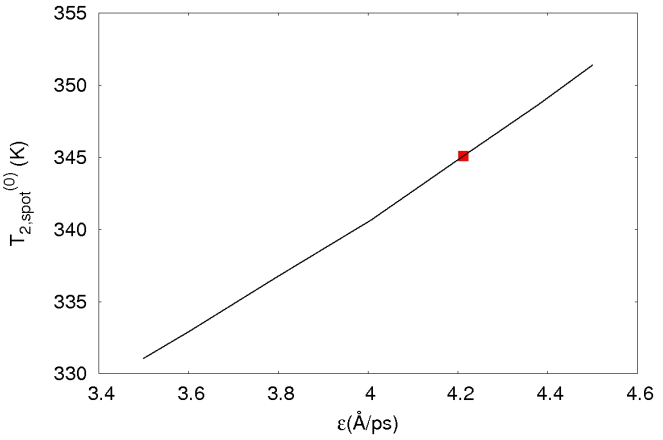

Figure 5.6: ϵ used in Eq.5.3 versus $T^{(0)}_{2,spot}$ after 1 ps of thermalization procedure.

$T^{(0)}$	κ_{white}	$\kappa_{K-A_1'}$	$\kappa_{\Gamma-E_{2g}}$
100 K	752±6	487±2	514±3
300 K	621 ±5	497±3	520±3

Table 5.1: Thermal conductivities (in unit of W m^{-1} K^{-1}) estimated at $T_1^{(0)}$=100 K and $T_2^{(0)}$=300 K in the case of white and colored ($K-A_1'$ and $\Gamma-E_{2g}$ modes) thermalizations.

5.3.2 *Results*

By means of the procedure described above, we performed AEMD simulations for the two initial sample temperatures $T_1^{(0)}$=100 K and $T_2^{(0)}$=300 K by considering three different hot spot excitations, namely:

- a white thermalization where we act on all the spot degrees of freedom;
- a colored thermalizations where just the atom's displacement of the $K-A_1'$ modes is excited;
- a colored thermalizations where just the atom's displacement of the $\Gamma-E_{2g}$ modes is excited.

Fig.5.7 compares the temperature profile evolution for the case of white (first line), colored $K-A_1'$ (second line) and colored $\Gamma-E_{2g}$ (third line) thermalizations (red dots) in the case $T_1^{(0)}$=100 K, while Fig.5.8 shows the profile for the same kinds of thermalization procedures but in the case $T_2^{(0)}$=300 K. All the simulation profiles have been fitted with the solution of the radial heat equation in order to estimate the corresponding κ (see Table5.1).

Table5.1 shows that in the case of a white thermalization we obtain thermal conductivity values much larger than exciting single modes. Another interesting result shown in Table5.1 is the lack of temperature dependence of thermal conductivity in the case of colored thermalizations. It is instead well-known that thermal conductivity in graphene strongly depends on temperature as in fact observed for the white thermalization.

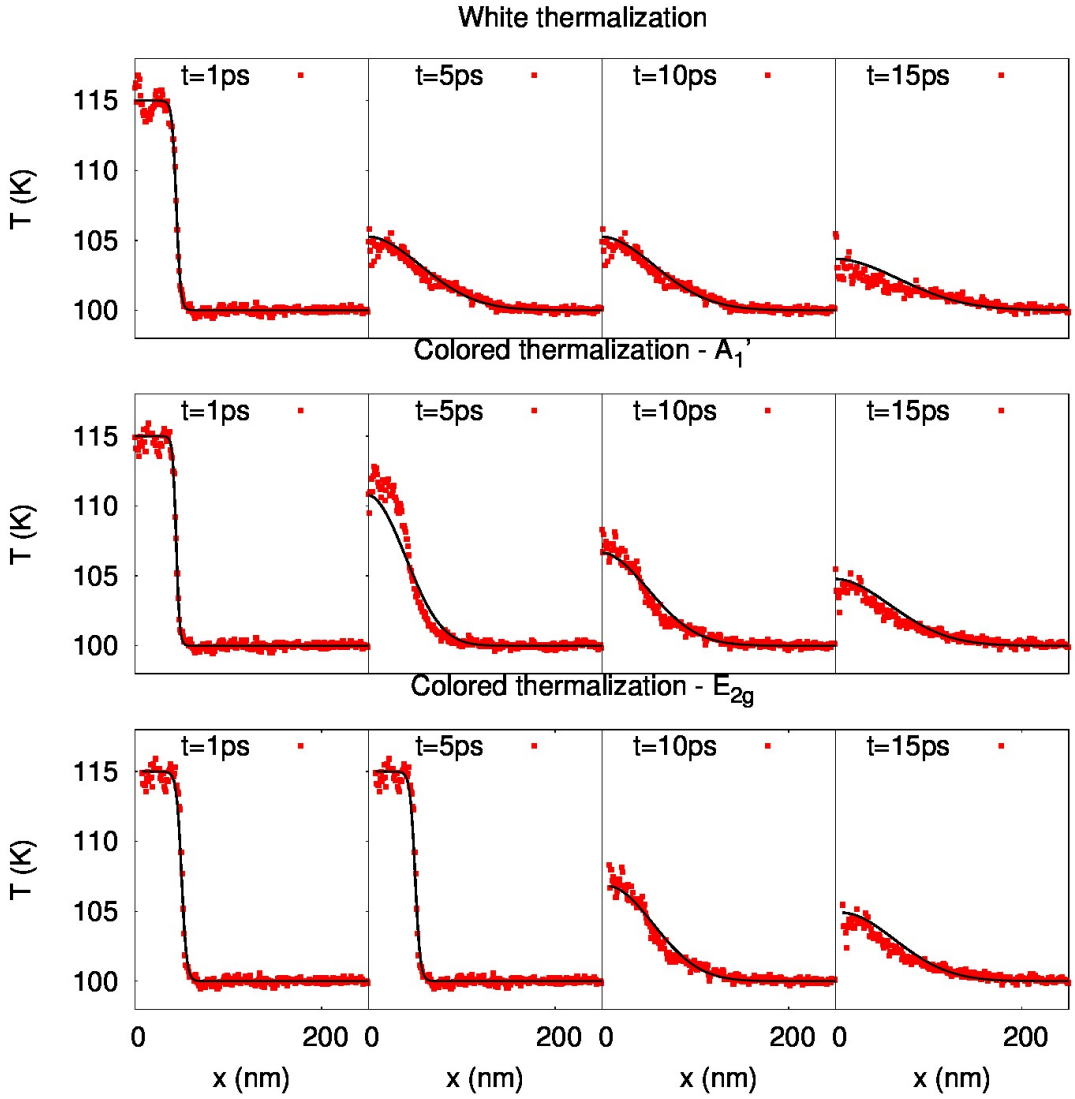

Figure 5.7: Temperature profile evolution in the case of white (first line), colored $K - A_1'$ mode (second line) and colored $\Gamma - E_{2g}'$ mode thermalizations (third line) where $T_1^{(0)}$=100 K. Black lines represents the solution of Eq.5.1, $T_{theo}(R,t)$ which has been used to fit $T_{sim}(R,t)$ in order to obtain α.

A further prove of the different transient thermal behavior between white and colored thermalizations is given by Fig.5.9, where the time evolution of the temperature difference $\Delta T(t)$ between the spot and the rest of the sample is shown. In this case we observe a slower $\Delta T(t)$ decrease in the case of the colored ($K - A_1'$ mode) thermalizations indicating an overall thermal conductivity reduction. Fig.5.9 also shows that the solutions of Eq.5.1 are not able to accurately fit $\Delta T(t)$. In particular the an-

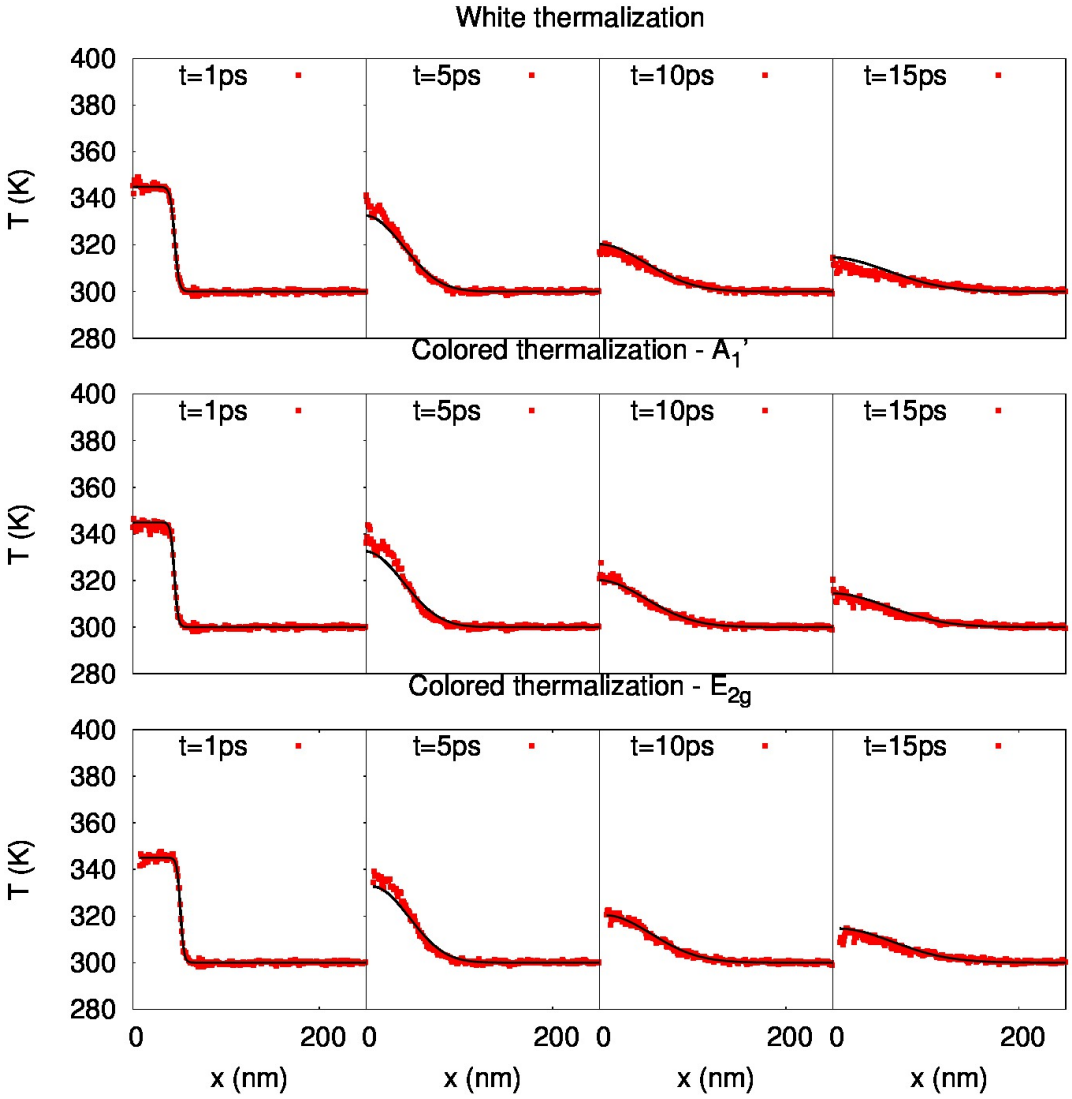

Figure 5.8: Temperature profile evolution in the case of white (first line), colored $K - A_1'$ mode (second line) and colored $\Gamma - E_{2g}'$ mode thermalizations (third line) where $T_2^{(0)}$=300 K. Black lines represents the solution of Eq.5.1, $T_{theo}(R,t)$ which has been used to fit $T_{sim}(R,t)$ in order to obtain α.

alytical fitting curve (continuous lines) during the first few ps decreases much faster with respect to the $\Delta T(t)$ coming from the simulations, while it underestimates the simulation curve decreasing velocity in the final time-steps. Actually, these effects compensated one to each other, resulting in an overall reliable estimate for κ coefficient. The discrepancies could be explained in terms of non diffusive thermal conduction in graphene which has been previously discussed by Ref.[41]. For future purpose,

I could try to fit the evolution of the temperature profile by using the hyperbolic hydrodynamics heat conduction equation instead of the common parabolic one (Eq.5.1):

Hyperbolic hydrodinamic heat equation

$$\frac{\partial^2 T(r,t)}{\partial^2 r} + \frac{1}{r}\frac{\partial T(r,t)}{\partial r} = \frac{C_V \rho}{\kappa}\frac{\partial T(r,t)}{\partial t} + \frac{1}{C^2}\frac{\partial^2 T(r,t)}{\partial^2 t} \quad (5.4)$$

where C is called the speed of second sound and the other quantities defined as in Eq.5.1.

However, in Ref.[91], in which such non diffusive anomalies have been analyzed, it has been demonstrated that thermal transport in graphene is anyway dominated by a Fourier-diffusive behavior. This statement enables us to use Eq.5.1 and justifies the corresponding analysis.

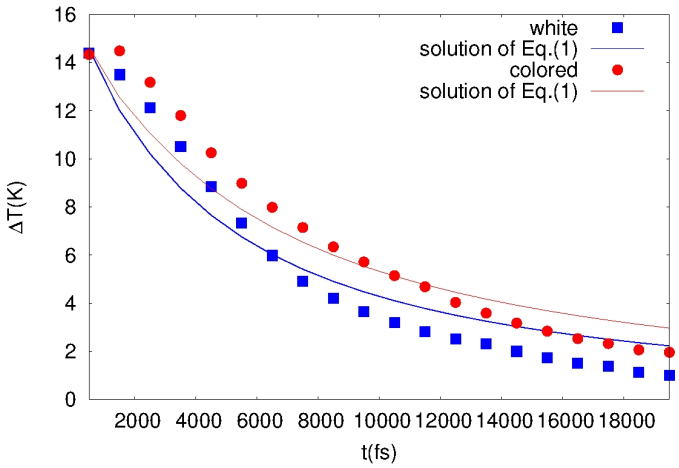

Figure 5.9: $\Delta T(t)$ fitted with the solutions of the radial heat equation for the white and the colored ($K - A_1'$ mode) thermalizations.

5.4 ADDRESSING THERMAL CONDUCTIVITY LENGTH DEPENDENCE

I previous showed in Chapter 4 that graphene experiences a pronounced length-dependence thermal conductivity up to lengths $L \sim 0.1$ mm [41, 2]. We explore wether such a length-dependence is still present in the case of both white and colored thermalizations by doubling R_{sample} from 248.10 nm to 431.63 nm, reaching a total number of atoms equal to 20659238. Table5.2 shows the estimated thermal conductivities at $T_1^{(0)}$=100 K and

$T^{(0)}$	R_{sample}	κ_{white}	$\kappa_{K-A_1'}$
100 K	248.10 nm	752±6	487±2
	431.63 nm	865±20	652±5
300 K	248.10 nm	621±5	497±3
	431.63 nm	670±13	508±3

Table 5.2: Thermal conductivities estimated (W m^{-1} K^{-1}) at $T_1^{(0)}$=100 K and $T_2^{(0)}$=300 K in the case of white and colored ($K-A_1'$) thermalizations.

$T_2^{(0)}$=300 K in the case of white and colored ($K-A_1'$) thermalizations. At $T_1^{(0)}$=100 K we observe, for both thermalizations, an actual thermal conductivity length-dependence which is more pronounced than at $T_2^{(0)}$=300 K. Moreover, by the increasing of the sample size the expected temperature dependence of thermal conductivity is recovered.

5.5 ANALYZING THE TIME EVOLUTION OF THE VIBRATIONAL DENSITY OF STATES

To the aim of further investigating the different phonon transport properties observed in the case of the colored and white thermalizations, resulting in (i) a different κ values and (ii) different κ dependence on T, I focused on the time evolution of the vibrational density of states (VDOS). The VDOS has been calculated as the Fourier transform of the velocity autocorrelation function, where the atomic velocities have been collected on the central spot during the microcanonical run following the initial colored ($K-A_1'$) thermalization at $T_{1,spot}^{(0)}$=115 K.

Vibrational properties and autocorrelation velocity function

Actually, the velocity autocorrelation function is usually calculated when one wishes to analyze the vibrational or diffusive properties of a system. If the velocity vector for a group of atoms is $\mathbf{v}$, then the velocity autocorrelation can be written as

$$VACF(t) = \frac{\langle \mathbf{v}(0) \cdot \mathbf{v}(t) \rangle}{\langle \mathbf{v}(0) \cdot \mathbf{v}(0) \rangle} \tag{5.5}$$

If the motion of the atoms tends to an oscillatory pattern, the VACF will characterize the oscillations because the velocity of the atoms will self-correlate in a periodic fashion. Similarly, if the velocity of atoms tends to one direction, then the VACF will gradually grow in magnitude characterizing the diffusion of the atoms. In this case we are interested on using the VACF to calculate the vibrational spectrum of the system, which is found by taking the Fourier transform of the VACF as:

$$F(\omega) = \frac{1}{\sqrt{2\pi}} \int_{-\infty}^{\infty} dt e^{i\omega t} VACF(t) \tag{5.6}$$

The vibrational density of states (VDOS) is then $\Phi(\omega) = F(\omega)^2$.

In detail, the LAMMPS code provides a computation that calculates the velocity auto-correlation function (VACF), averaged over a group of atoms. Each atom's contribution to the VACF is its current velocity vector dotted into its initial velocity vector at the time the compute has been specified. Thereafter, the VACF have been Fourier transformed obtaining a VDOS for the specific atom region.

A Gaussian low pass filter with a width of 41.7 cm^{-1} has been applied to reduce the noise of the data. The accuracy of this method has been compared to results obtained from density functional theory (DFT) calculations through the diagonalization of the dynamical matrix and have been shown to be in general agreement.

Fig.5.10 (top) shows the time evolution of the colored VDOS (t=5, 20, and 270 ps) (projected in the central spot) during the microcanical run following the initial spot thermalization at $T^{(0)}_{1,spot}$=115 K according to the $K - A_1'$ mode. Fig.5.10 (bottom) shows instead the corresponding "equilibrium" VDOS calculated during a microcanonical run in which the whole sample was thermalized by means of the Nosé-Hoove scheme T=100 K.

During the first few ps, we observed significant differences between the colored (top) and the "equilibrium" VDOS as far as it concerns the position as well as the intensity of the main peaks. In particular, in the colored VDOS (top) we clearly observe the presence of the characteristic $K - A_1'$ peak at a frequency 1172

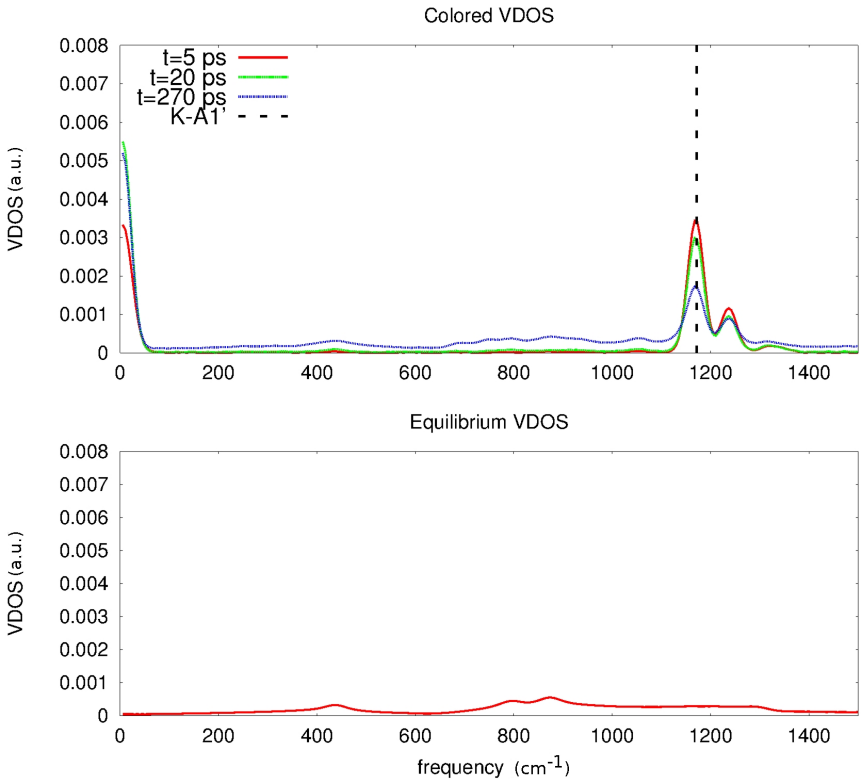

Figure 5.10: (Top: vibrational density of states (VDOS) projected on the central spot estimated at different times (t=5, 20, and 270 ps) in the case of the colored $K - A_1'$ thermalization. Bottom: VDOS projected on the central spot estimated in the case of thermal equilibrium condition at $T_1^{(0)}$=100 K . The dashed line represents the frequency of the $K - A_1'$ mode.

cm $^{-1}$, that we intentionally activate, which is absent in the equilibrium VDOS (bottom).

Moreover, during the first 5 ps we observed a depopulation of the $K - A_1'$ peak which decays into one couple composed by LA and LO phonons and another couple of acoustic modes TA and LA which generate the two observed peaks at frequencies of $\sim$ 50 cm $^{-1}$ and $\sim$ 1250 cm $^{-1}$. Such decay channels have been previously identified in Ref.[88], by means of explicit calculations of phonon-phonon and electron-phonon interactions by DFPT, as the most probable $K - A_1'$ decays with an overall probability of 55%. This mechanism is still present after 20 ps (time needed to flat the initial temperature step) since the $K - A_1'$ peak intensity further decreases while the intensity of

the TA-LA peaks increases. In the period between 20 and 270 ps we observed the presence of other $K - A_1'$ decay channels identified by the appearance of two additional peaks at frequencies of ~ 400 cm $^{-1}$ and ~ 800 cm $^{-1}$ corresponding to the decays into the TA-TA and TA-LA modes.

This analysis suggests that in the period of 20 ps after the colored thermalization, the phonon population distribution is far from the equilibrium, being characterized by only few specific sharp phonon peaks. This gives rise to a completely different thermal transport mechanism with respect to the white case in which all the phonon modes were initially occupied, resulting in an overall thermal conductivity reduction.

In conclusion, in the work [4] I have introduced a novel methodology to analyze the transient heat transport regime in the case of a laser pulse excitation on a graphene sample by explicitly reproducing the excitation of the $K - A_1'$ and $\Gamma - E_{2g}$ optical phonon modes which are the ones strongly coupled with photogenerated electrons. In detail, in order to estimate thermal conductivities in a transient regime, we initially create a step-like temperature gradient by means of two different thermalization procedures i.e a white where all the vibrational modes were initially excited and a colored one where only one of the $K - A_1'$ and $\Gamma - E_{2g}$ was initially excited. The thermal conductivity, estimated by using the numerical solution of the radial heat equation, shows a strong dependence on the kind of thermalization i.e. in the case of both colored thermalization κ is dramatically reduced with respect to the white one. Moreover we observed that κ is much less sensitive to temperature in the case of the colored thermalization. We interpret such different thermal conduction behavior by analyzing the time dependent vibrational density of states in both cases. In particular we observe that the colored phonon population remains far from the equilibrium during the whole simulation giving rise to a completely different thermal transport mechanism and more importantly we can identify the optical phonons decay channels into the acoustic phonons.

Part IV

TAYLORING THERMAL PROPERTIES BY HYDROGENATION

In this part, I will address the hydrogenation effect on graphene thermal transport. In chapter 6, I will show the results concerning the thermal conductivity measure in graphane by explaining the mainly reasons behind its dramatic κ reduction with respect to the pristine graphene. On the other side, in Chapter 7 I will design a new graphane/graphene thermal diode analyzed by means of NEMD calculations.

6

THERMAL CONDUCTIVITY IN HYDROGENATED GRAPHENE

6.1 INTRODUCTION TO HYDROGENATED GRAPHENE

Both chemical and/or physical strategies have been proposed to tune graphene thermal transport, which could be useful in nanoscale engineering and heat management.

For instance, one can imagine atoms or molecules being attached to the atomic scaffold in a strictly periodic manner, which should result in a different electronic structure and, essentially, a different crystalline material.

The idea of attaching atomic hydrogen to each site of the graphene lattice, has been at first theoretically introduced by Sofo et al. [58] and Boukhvalov et al. [92].

Orderly hydrogen decorating graphene: graphane synthesis

In 2009 for the first time Elias et al. synthesized this hydrogenated graphene referred to as graphane[59]. Hydrogenation procedure has been performed on graphene crystals prepared using micromechanical cleavage of graphite on top of an oxidized Si substrate as well as on free-standing graphene membranes. After an initial annealing at 300°C for the duration of 4 hours in argon atmosphere in order to remove any possible contamination, they have been exposed to a cold hydrogen plasma. In particular, it has been used a low-pressure (0.1 mbar) hydrogen-argon mixture with dc plasma ignited between two aluminum electrodes for a two hours long treatment. In this way, stable hydrogenated graphane samples at room T have been obtained, which showed the same characteristics during repeated measurements for many days. More recently, a systematic study by Wen et al. [93] has proved that actually there exist eight graphane isomers. They all correspond to covalently

bonded hydrocarbons with a C:H ratio of 1. Interesting enough, four isomers have been found to be more stable than benzene.

The attractive feature of graphane is that by variously decorating the graphene atomic lattice with hydrogen atoms, creating the different isomer configurations, it is possible to generate a set of two dimensional materials with new physic-chemical properties [76].

For instance, it has been calculated that graphane, differently to graphene which is a highly conductive semi-metal, is an insulator with an energy gap as large as ~6 eV [76], making it interesting in naturenoelectronic field. As far as the elastic behavior is concerned, it has been proved that hydrogenation largely affects the elastic moduli as well: the in-plane stiffness and Poisson ratio of graphane are smaller than those of graphene.

Main graphane properties

All these differences between graphane and graphene, are mainly due to the change in the carbon atoms hybridization from sp^2 to sp^3 upon hydrogenation. This bounding transition removes the conducting p-bands opening the energy gap. In addition, it enables lattice deformations by variations of the tetrahedral angles (on the contrary of the strength carbon-carbon bonds in flat sp^2 hexagonal lattice), decreasing the Young modulus.

Moreover, graphene hydrogenation has been shown to be very effective on controlling thermal conductivity. In Ref.[47] theoretical NEMD calculations demonstrated that by randomly adding as few as 10% hydrogen atoms on top of pristine graphene a dramatic reduction of thermal conductivity has been observed. Moreover, they studied the case where hydrogen atoms are arranged in regular stripes perpendicular or parallel to the heat flux, obtaining that for the former a small coverage causes a sharp thermal conductivity drop while in the latter thermal conductivity gradually decreases with the increase of coverage from 0% to 100%.

In contrast to the large variety of experimental and theoretical works on graphene thermal properties, few information are available on graphane. In particular, to the best of our knowledge, no experimental works have been published yet on graphane thermal conductivity.

On the other side, as concerned theoretical investigation, in Ref.[94] a molecular dynamics study about graphene and C-graphane κ dependence from shear strain has been presented. The authors performed EMD simulations by using Tersoff potential on simulation cells having an area of 5.4×13 nm^2, much more smaller with respect to our samples. They observed that under the same shear strain, the graphane sheet has much lower thermal conductivity than the graphene one and measured for not strained samples $\kappa \simeq 625$ Wm^{-1}K^{-1} and 380 Wm^{-1}K^{-1} for graphene and C-graphane respectively.

More recently, another paper addresses the thermal transport in graphane nanoribbons (GANRs) by using non equilibrium Green function method to calculate phonon transmission in the framework of Landauer approach[95]. In this case, they have found that the (GANRs) thermal conductivity is reduced of about 40% with respect to the case of the graphene ribbons.

Motivated by this scenario, as well as by the need to improve our basic understanding of thermal transport properties in 2D carbon sheets already addressed in the previous Chapter, I present in this Chapter a through investigation of thermal conductivity in graphane.

Between the eight different graphane isomers identified so far, the most stable ones are three conformers referred to as chair (C-graphane), boat (B-graphane) or washboard (W-graphane) [93, 76]. In C-graphane the hydrogen alternate on both sides of the carbon sheet, in B-graphane pairs of hydrogen atoms alternate along the armchair direction of the carbon sheet, finally in W-graphane double rows of hydrogen are aligned along the zigzag direction of the carbon sub-lattice and alternate on both sides of the carbon sheet. According to first principles calculations, C-graphane is the most energetically favorable conformer followed by W- and B-graphane [76, 96].

6.2 MD SIMULATION ON GRAPHANE

In the work [1], I studied thermal conductivity of these graphane isomers by means of "approach to equilibrium molecular dynamics" (further details in Chapter 3).

Basing on the previously proved assumption that the method is invariant with respect to the initial temperature gradient value (see Chapter 3), we imposed an initial temperature gradient $\Delta T(0)$=200 K by thermalizing half of the sample at T_1=400 K and the other at T_2=200 K in both graphene and graphane isomers case by using a velocity rescaling. The equations of motion are integrated by the velocity Verlet algorithm with 1.0 fs timestep. As I have already explained in Chapter 3, the periodic boundary conditions applied to the simulation cell during the calculations, enable to simulate an infinite sample in the lateral directions.

6.2.1 *Structural feature prediction*

All the simulations are performed as in Chapter 4 with the "Reactive Empirical Bond Order" (REBO) potential in its second generation form [68], needed to investigate hydrocarbon materials such as graphane.

An important issue we need to address is the reliability of REBO potential for the description of the graphane structural features. To this aim, starting from the orderly hydrogenated planar graphene, we performed a geometry optimization by means of the conjugate gradient algorithm (CG). Actually the procedure is aimed at the minimization of the total potential energy of the system as a function of the N atom coordinates:

$$\begin{aligned} E(\mathbf{R}_1, \mathbf{R}_2, ...\mathbf{R}_n) &= \sum_{i,j} E_{pair}(\mathbf{R}_i, \mathbf{R}_j) + \sum_{i,j} E_{bond}(\mathbf{R}_i, \mathbf{R}_j) \\ &+ \sum_{i,j,k} E_{angle}(\mathbf{R}_i, \mathbf{R}_j, \mathbf{R}_k) + \sum_{i,j,k,l} E_{dihedral}(\mathbf{R}_i, \mathbf{R}_j, \mathbf{R}_k, \mathbf{R}_l) \end{aligned} \tag{6.1}$$

where the first term is the sum of all non-bonded pairwise interactions, including long-range Coulomb interactions, while the

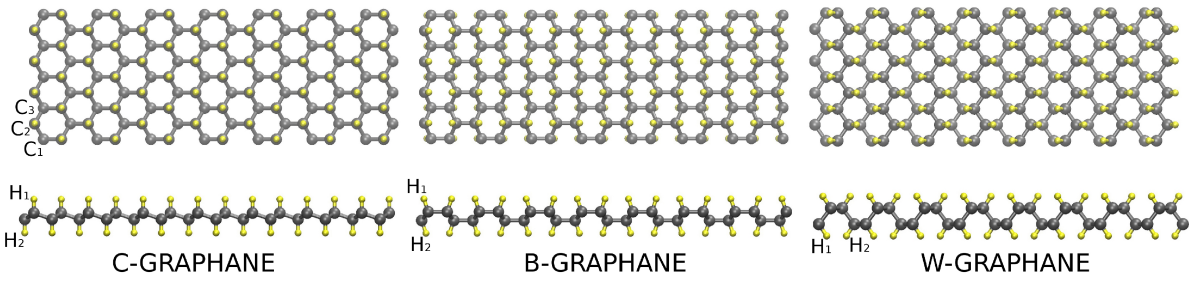

Figure 6.1: Stick and ball representation of the top and side views of the three C-, B-, and W-graphane isomers. For visualization reasons, we represent simulation cells much smaller with respect to the ones used for the AEMD calculations.

others terms are bond, angle, and dihedral interactions, respectively. The starting point for the minimization is the current configuration of the atoms. In order to find the configuration corresponding to a local potential energy minimum, atom coordinates are iteratively adjusted until one of the following stopping criteria is satisfied: i) the change in energy or in force gradient between outer iterations is less than a certain tolerance, ii) the search does not reduce more the energy because even the maximum atom displacement is tiny compared to typical atom coordinates precision and iii) the number of outer iterations or the number of total force evaluations exceed a maximum value set. At each iteration the force gradient is combined with the previous iteration information to compute a new search direction perpendicular (conjugate) to the previous search direction. In particular, I used the Polak-Ribiere (PR) version of the algorithm which is thought to be the most effective CG choice for many problems. The PR variant generalizes the CG method to a non-linear optimization which affects how the direction in the minimum searching is chosen.

Graphane structural features predicted by REBO potential

Fig.6.1 shows the structural minima for the three graphane isomers under investigation: all the structural parameters are in good agreement with previous DFT calculations [76], as shown in Table6.1. Here we observed angle and bond deviations below 2% and dihedral deviations below 12%. As far as concerns the stability, we remark that the REBO potential predicts, similarly to DFT calculations, the three isomers to be almost isoener-

Table 6.1: C_1-C_2 and C-H bond lengths (see Fig.6.1), $C_1C_2C_3$ angles and $H_1C_2C_3H_2$ dihedral angles for C-graphane, B-graphane, W-graphane systems obtained using REBO potential or by DFT calculations.

DFT	C-Graphane	B-Graphane	W-Graphane
C_1-C_2	1.54 [Å]	1.54 [Å]	1.54 [Å]
C-H	1.09 [Å]	1.09 [Å]	1.09 [Å]
$C_1C_2C_3$	111.5°	110.7°	111.2°
$H_1C_2C_3H_2$	180°	180°	58°
REBO	**C-Graphane**	**B-Graphane**	**W-Graphane**
C_1-C_2	1.54 [Å]	1.54 [Å]	1.54[Å]
C-H	1.09 [Å]	1.09 [Å]	1.09[Å]
$C_1C_2C_3$	110.2°	110.2°	110.2°
$H_1C_2C_3H_2$	180°	180°	51°

getic (although DFT predicts a small energy difference which is likely not captured by REBO due to the lack of dispersive and torsional interactions of the REBO potential).

6.2.2 *Comparison between graphene, C-,B-, and W-Graphane thermal conductivities*

By considering the graphene honeycomb structure, there may be two different edge shapes when they are cut, namely: armchair edge and zigzag edge (see Fig.6.2). For all the samples, I analyzed the thermal transport by considering heat flux flowing in both armchair and zigzag directions because in principle we can not *a priori* guess that the transport properties are isotropic in such materials.

As a benchmark calculations, I report in Fig.6.3 thermal conductivity values (calculated by using the same procedure of Chapter 4) in armchair and zigzag directions for graphene samples with $125.8 \leqslant L_x \leqslant 2096.5$ nm and $145.0 \leqslant L_x \leqslant 2420.6$ nm, re-

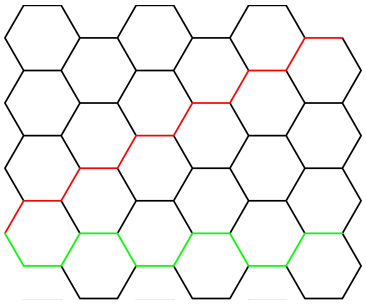

Figure 6.2: κ Armchair (red) and zigzag (green) directions in graphene honeycomb.

spectively, and with fixed lateral width L_y=2.2 nm, which is the minimum lateral size for which κ has been demonstrated to be independence on the sample width (see Fig.4.4 Chapter 4).

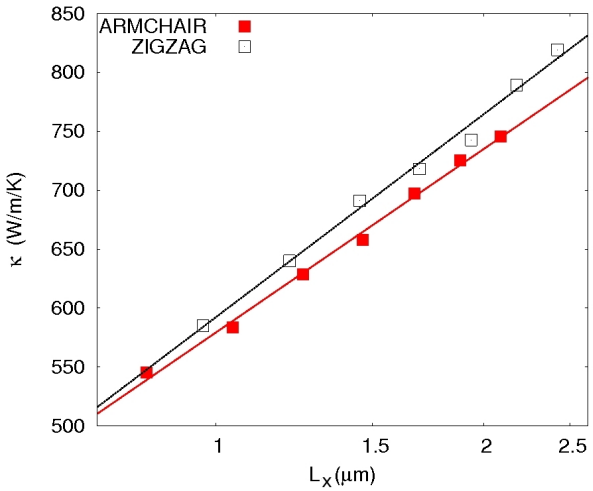

Figure 6.3: κ vs. L_x plot for graphene in armchair (red) and zigzag (black) directions at 300 K.

The $\kappa(L_x)$ values for the largest simulation cells with L_x=1672.6 nm and L_x=2178.5 nm are 697.2 ± 0.4 and 789.3 ± 0.3 W m^{-1} K^{-1} for armchair and zigzag directions, respectively. The small armchair-zigzag anisotropy in thermal transport we found (thermal conductivity along zig-zag direction slightly higher than the one along armchair direction) has been already pointed out by previous MD investigations [47, 48]. It has been known that such anisotropy is due to the simulation cell length finiteness and it tends to vanish in longer samples, coherently with the expected graphene symmetric behavior. Our κ values are in

very good agreement with previous results obtained by solving Boltzmann transport equation in relaxation time approximation (BTE-RTA) using the same REBO potential [34]. On the other hand, the present $\kappa(L_x)$ values are underestimated with respect to state-of-art experiments [8, 97], as likely due to the small REBO underestimation of the acoustic phonon group velocities with respect to other potentials such as Tersoff. The choice of the present interatomic potential is nevertheless justified by the need to simulate hydrocarbons such as graphane. Since BTE represents the most reliable theoretical tool for thermal transport estimations, the excellent agreement with such methodology is a further clear validation of the AEMD method.

Similarly to what has been done with graphene, I calculated the thermal conductivity of the three C-, B- and W-graphane isomers in both the armchair and zigzag directions. Actually we don't know the graphane thermal conductivity dependence upon sample length, but basing on the previous observed graphene case, we performed AEMD simulations on graphene, C-, B- and W-graphane with periodically repeated simulation cells having $108.9 \leqslant L_x \leqslant 1754.2$ nm and the same fixed lateral width L_y=2.2 nm.

Fig.6.4 represents the C-, B- and W-graphane thermal conductivities along the armchair direction together with the one of graphene for comparison. It is important to remark that, for the range of L_x values of interest for the present investigation, it is definitely true that $\kappa(L_x) \sim \log(L_x)$ for both graphene and graphane.

Thermal conductivities are always significantly smaller than the one of graphene. Differently to graphene, in graphane we observe a rather weak κ dependence from L_x suggesting a different distributions in phonons mean free path (MFP). In particular, we observe a κ convergence for samples having $L_x \sim 500$ nm suggesting that the thermal transport in graphane is characterized by phonons with smaller MFP than graphene. The $\kappa(L_x)$ values for the biggest simulation cells with L_x=1754.2 nm, L_x =1661.6 nm, L_x=1452.6 nm are 79.3 ± 0.5, 38.3 ± 0.2, 30.8 ± 0.4 for C-, B- and W-graphane respectively.

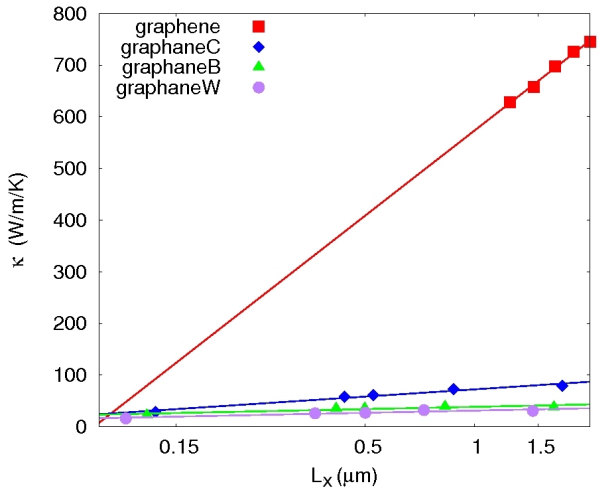

Figure 6.4: κ vs. L_x plot for C-, B- and W-graphane and graphene in armchair direction at 300 K.

Fig.6.5 represents the C-, B- and W-graphane thermal conductivities along the zig-zag directions together with the one of graphene for comparison. We considered simulation cells with $151.7 \leqslant L_x \leqslant 2025.3$ and the fixed lateral width $L_y = 2.0$ nm, 2.1 nm and 1.8 nm for C-, B- and W-graphane respectively. Also in this case the logaritmic dependence is lower respect to the case of graphene. The $\kappa(L_x)$ values for the biggest simulation cells with L_x=2025.3 nm are 78.0 ± 0.1, 64.1 ± 0.2, 86.2 ± 1.6 for C-, B- and W-graphane respectively. Table6.2 summarizes the κ results corresponding to the biggest simulation cells for all the systems here considered, showing that the $\kappa(L_x)$ calculated for all the graphane isomers are at least one order of magnitude smaller than the ones for graphene having similar cell-lengths in both armchair and zigzag directions.

6.3 DISCUSSION ABOUT THERMAL CONDUCTIVITY REDUCTION UPON HYDROGENATION

In order to elucidate the dramatic reduction of graphane thermal conductivity with respect to pristine graphene, we compared the phonon dispersion curves and the phonon density of state (PDOS) of graphene and C-graphane.

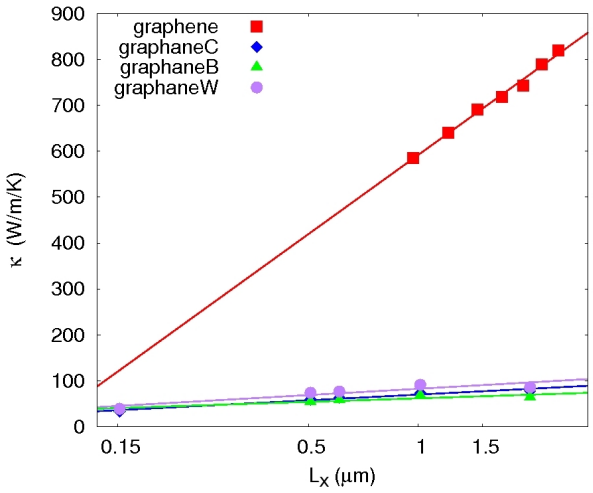

Figure 6.5: κ vs. L_x plot for C-, B- and W-graphane and graphene in zig-zag direction at 300 K.

Table 6.2: Thermal conductivity values for graphene with length L_x=1672.6 nm, C-graphane with L_x=1754.2 nm, B-graphane with L_x=1661.6 nm, W-graphane with L_x=1452.6 nm in armchair direction and for graphene with length L_x=2178.5 nm, C-, B-, W-graphane with L_x=2025.3 nm in zigzag direction (units of $Wm^{-1}K^{-1}$).

κ	Graphene	C-Graphane	B-Graphane	W-Graphane
ac	697.2±0.4	79.3±0.5	38.3±0.2	30.8±0.4
zz	789.3±0.3	78.0±0.1	64.1±0.2	86.2±1.6

Phonon properties analysis in graphane

These two quantities are calculated directly from molecular dynamics simulations by constructing the dynamical matrix based on fluctuation-dissipation theory (see Chapter 3)[75, 80]. Fig.6.6 (right) shows the comparison between graphene (solid red line) and C-graphane (dashed blue line) PDOS. We observed a significant variation of the peak positions as well as their intensities upon the graphene hydrogenation. We focused in particular on the acoustic range of the PDOS (up to ~ 30 THz) since thermal conductivity of graphene is largely dominated by these phonons [98]. In this range we observed a significant shift of the C-graphane PDOS by ~ 10 THz together with a reduction of the peaks intensity. This can explain the reduced thermal

conductivity of graphane with respect to pristine graphene. In addition, we observed a general broadening of the C-graphane peaks with respect to graphene. This can suggests an overall lifetime reduction of the corresponding modes which is again related to a reduced thermal conductivity.
Fig.6.6 (left) shows the phonon dispersion curves for graphene (solid red line) and C-graphane (dashed blue line). In the case of C-graphane we observed a reduction of the slope of the acoustic TA and LA branch with respect to graphene indicating an overall reduction of the corresponding TA and LA group velocities. Several previous papers [78, 33, 79] underlined the importance of the TA and LA modes for graphene thermal conductivity for this reason a significant reduction of their group velocities can explain the suppression of thermal conductivity observed in the case of graphane.

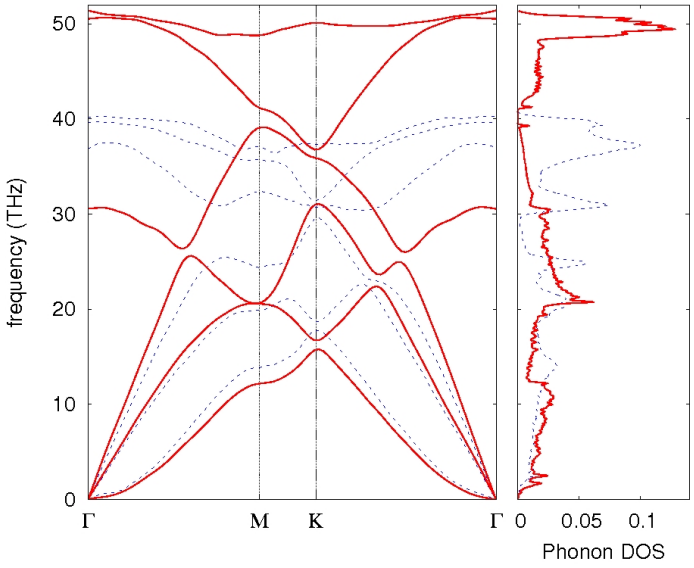

Figure 6.6: Vibrational density of state (right) and dispersion curves (left) of graphene (solid red line) and C-graphane (dashed blue line).

Another important issue related to the thermal conductivity decrease is the significant reduction of all the elastic constant of graphane with respect to graphene[76] as due to the sp^2 to sp^3 transition. This reduction can give rise to an increase in the graphane roughness, which affects the overall thermal transport. In order to further explore this feature, we estimate the

Evidence of increased roughness in graphane

graphane maximum out-of-plane oscillation amplitudes Δz during a NVT simulation performed at 300 K for 1.0 ns. Table6.3 shows the calculated Δz values together with the corresponding $\kappa(L_x)$ for graphene and graphane. We observed that κ is correlated to the inverse of Δz: the increase of the out-of-plane oscillation amplitudes hinders the overall thermal transport.

Table 6.3: Maximum out-of-plane oscillation amplitudes (units of nm) and κ values (units of $Wm^{-1}K^{-1}$) for graphene with L_x=146.3 nm, C-graphane with L_x=131.6 nm, B-graphane with L_x=124.6 nm, W-graphane with L_x=108.9 nm samples

	Graphene	C-Graphane	B-Graphane	W-Graphane
κ	657.70±0.41	28.58±0.05	22.74±0.04	16.18±0.02
Δz	1.25	1.98	2.09	2.91

In fact, it is reasonable that the differences in the elastic behaviour between graphene and graphane reflect in the different thermal transport behaviour of the two materials. The increasing in the out-of-plane bending movement of graphane should affect especially flexural phonon modes[99]. In particular, the first flexural mode is closely related to the Young's modulus, which is reduced in the case of graphane with respect to graphene[100]. In this perspective, the reduction of phonon life-times that I described before is related to the substantial increase of the graphane flexural modulus with respect to graphene, which makes the anharmonic decay into two lower-energy phonons much easier. Unfortunately, this change in the flexural dispersion slope is not so clear in Fig.6.6 (left) as due to the simulation cell size, which affects especially the phonon band near Γ point.

In conclusion, thermal conductivity of three hydrogenated graphene isomers (B-,C-, and W-graphane) has been calculated by means of the approach to equilibrium molecular dynamics methodology. The overall graphane thermal conductivity is dramatically reduced with respect to pristine graphene by more than one order of magnitude. We explained this reduction in terms of

different vibrational density of states and dispersion curves. In particular, we observed a reduced PDOS peaks intensity in the acoustic range in the case of graphane together with a reduce group velocity of the TA and LA acoustic modes. In addition we correlated the κ decrease with the increasing out-of-plane oscillation amplitude, due to the $sp^2 - sp^3$ transition. The observed dramatic reduction of thermal transport upon hydrogenation in graphene, could be explored as a way to tune thermal transport in graphene for phononic applications such as thermal diodes.

7

EXPLOITING HYDROGENATION FOR THERMAL RECTIFICATION IN GNS

7.1 INTRODUCTION TO THERMAL RECTIFICATION

It is well-known that tailoring heat flux could be very useful for thermal management improvement in nano-devices, such as on-chip cooling and energy conversion, as well as to create thermal circuits using phonons as information carriers in logic-devices [56, 55, 101] and in this framework an important role is played by possible thermal devices which experience thermal rectification. We will refer to such devices as thermal diodes (TDs).

Thermal rectification (TR) is a phenomenon in which thermal transport along a specific axis is dependent upon the sign of the temperature gradient or heat current (hereafter referred to as thermal bias). This non linear response to a thermal perturbation has been a topic of great interest, as concerned theoretical explanations as well as possible applications. For this reason, activity in this area has been largely increased in the last decade.

First attempt to design solid state TDs

Several theoretical studies focused on thermal rectification have proposed alternative systems such as: non-linear lattices [102], asymmetric shape samples [103, 104] and interfaces between different materials [105, 106, 107]. As far as concerned the first, for example, Terraneo et al. demonstrated theoretical rectification behavior using a nonlinear one-dimensional chain of atoms between two thermostats at different temperatures. In their system, they were able to change the chain from a normal conductor in one direction to a nearly perfect insulator in the other direction by exploiting the non-linearity of the potential. In Ref.[55], on the other side, a TR value 100 times larger has been achieved by coupling two nonlinear lattices.

TD based on two different materials

For technological applications, the key issue is to suitably design the TD device in order to enhance the overall thermal rectification. Thermal diodes formed by a junction between two different bulk materials have been proposed, such as for example junctions between two different perovskite cobalt oxide, Silicon and Germanium or Silicon and amorphous polyethylene. However, it has been shown [103] that these two-segment TDs experience a large interface contact resistance which limits the resulting TR efficiency. In fact, the design of one-material based thermal diodes seems to be a crucial issue in the perspective to enhance TD's efficiency.

On the other side, the first experimental evidence of a solid state thermal rectifier has been obtained in 2006 by Chang et al.. They analyzed carbon nanotubes (CNT), where the mass distribution was suitably modulated along the CNT axis by a non-uniform deposition of $C_9H_{16}Pt$ molecules [108]. The resulting nanoscale system yields asymmetric axial thermal conductance. In particular, by means of a thermal bridge-like experiment (see Introduction), greater heat flow in the direction of decreasing mass density has been measured.

TD based on low dimensional systems

An alternative approach is to use one dimensional (1D) systems (i.e. nanotubes or nanowires) where the 1D intrinsic nature enhances non linear thermal effects such as TR [55, 109, 110]. Eventually, the link between low-dimensionality and non-linear thermal effects has motivated the investigation of 2D systems such as graphene. TDs made of graphene nanoribbons (GNR) have been recently proposed, where different asymmetric shapes, thickness and folding, as well as non-uniform distributions of defects have been investigated [105, 111, 112, 48, 113, 114]. In particular, a TR as large as $\sim 350\%$ has been estimated by means of Non Equilibrium Molecular Dynamics simulations (NEMD) in triangular and T-shaped GNRs [115].

7.2 EXPLOITING HYDROGENATION TO CONTROL HEAT FLUX

The previous chapter deals with the strong hydrogenation effects on graphene thermal properties. In particular, the κ reduc-

tion has been observed both in randomly H-decorated graphene samples [47] and in the most stable graphane isomers, as I proved in Ref.[1]. Motivated by these results, in this Chapter I present a molecular dynamics study aimed at exploring hydrogenation in graphene as a possible strategy to design efficient TDs which can be in principle synthesized by cold hydrogen plasma exposure using pattern-masks of different shapes [59]. A first attempt to identify possible TR effects in graphane/-graphene NRs has been previously studied by means of NEMD [112], where a simple planar graphane/graphene junction was analyzed. In such a system, a TR as large as $\sim$ 20% was predicted for infinite extended junctions. In details, they used a definition of TR coefficient based on the so-called interface thermal resistance (ITR). ITR, also known as thermal boundary resistance, or Kapitza resistance, is a measure of an interface resistance to thermal flow. This exists even at atomically perfect interfaces. In fact, due to the differences in electronic and vibrational properties in different materials, when an energy carrier (phonon or electron, depending on the material) attempts to traverse the interface, it will scatter through it. In the case of phonon heat transport, the probability of transmission after scattering will depend on the available phonon energy states on the two sides of the interface. In Ref.[112], the authors imposed a fixed heat flux (in one direction and after in the opposite one) and measured the ITR at graphane/graphene interface, which eventually has been used to compute TR. Anyway, the unreliable larger TR up to 20% for temperature gradient (about $\sim$ 30 K) much smaller than the ones we tested, is due to the supposed infinite extension of the graphane/graphene interface, that they obtained by imposing periodic boundaries condition in the direction along the interface.

I further explore the role of graphane/graphene interfaces in providing a rectification mechanism by considering more complex junctions, namely: vertical, triangular and T-shaped. Among all possible graphane isomers, I considered the *W* graphane, which shows the largest κ reduction with respect to pristine graphene, as it has been proved in Chapter 6 [1].

Having assessed in the previous Chapter the reliability of such a potential for the description of thermal transport in graphene-based systems, as well as for the graphane configuration features, the present simulations have been performed by using the "Reactive Empirical Bond Order" (REBO) potential in its second generation version[68].

7.2.1 *Sample preparation and method*

As mentioned above, I studied three kinds of nanoribbons, namely: sample A with a vertical graphane/graphene junction, sample B with a triangular-like junction, and sample C with a T-shaped junction. They are shown in Fig.7.1. We considered sample sizes with 30.8 nm$\leqslant L_x \leqslant$ 123.4 nm and 23.8 nm$\leqslant L_y \leqslant$ 95.8 nm and in this case, differently from the precedent ones, no periodic boundary conditions have been set to properly describe a finite width nanoribbon. The three samples have been generated by decorating along the armchair direction a graphene nanoribbon according to the following specific motifs:

- Sample A has been obtained by simply hydrogenating half of the GNR length along the heat transport direction x (see Fig.7.1, a).
- Sample B has been generated so as to obtain an inner triangular region of pristine graphene with a vertex angle θ (see Fig.7.1, b).
- Sample C has been obtained by hydrogenating half of the GNR along x, leaving a pristine graphene channel of width d=3 nm (see Fig.7.1, c).

All samples have been carefully relaxed by means of a combination of conjugate-gradient total energy minimization (see Chapter 6), followed by a 0.1 ns low-temperature (10 K) MD simulated annealing, and a further conjugate-gradient minimization. The NEMD simulations presented in Ref.[3] have been performed by thermostating the system by means of the Nosé-Hoover scheme (see Chapter 3) using a damping parameter of 100.0 fs and time step as small as 0.2 fs.

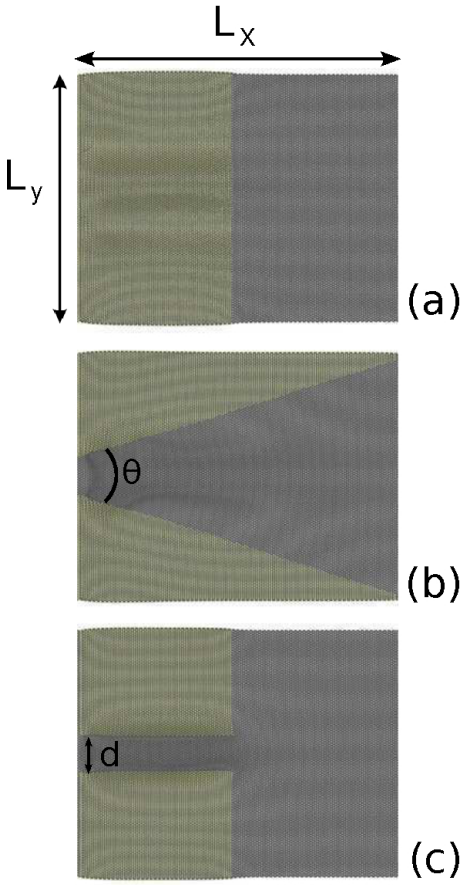

Figure 7.1: Stick and ball representation of the three graphane/graphene TD samples discussed in the text. The carbon (hydrogen) atoms are colored in gray (yellow).

In order to evaluate and quantify any possible rectification phenomena, it needs at first to generate a stationary thermal conduction regime along the sample. With this aim, two regions L and R on the opposite samples edges along the x direction have been eventually coupled to Nosé-Hoover thermostats set at unlike temperatures T_L and T_R respectively, to run the following NEMD simulations (see Fig.7.2).

By using the LAMMPS code command to perform time integration on Nose-Hoover style, in fact, it is possible to compute a global scalar which is extensive and represents the cumulative energy changed during the performed canonical (NVT) run. This cumulative injected (extracted) energy corresponds to the work done by the hot (cold) thermostat during the NEMD simulation. Eventually, we calculated the corresponding heat flux

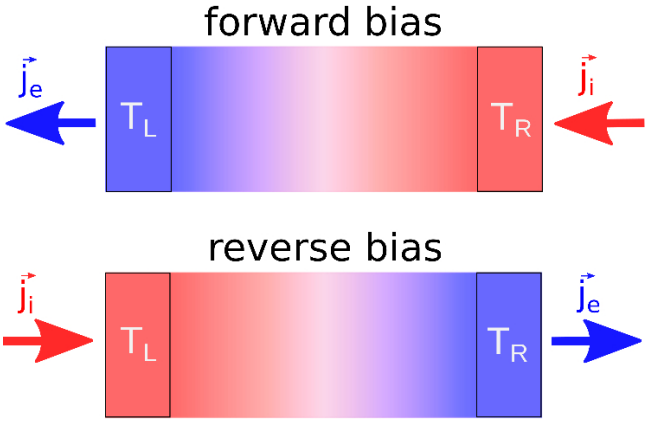

Figure 7.2: Schematic view of the simulation set-up used to estimate thermal rectification. The temperatures of the two thermostated regions are $T_L < T_R$ ($T_L > T_R$) for the forward (reverse) bias respectively. The corresponding heat fluxes injected into ($\mathbf{J}_i$) and extracted from ($\mathbf{J}_e$) the sample are indicated in both cases.

modulus as the numerical time derivative of the energy injected into (extracted from) the sample per unit cross-sectional area. We underline that, by means of the present procedure, we can estimate heat fluxes without any reference to the Fourier formalism, whose validity is still debated in the case of strong perturbations such as large thermal gradients.

In order to ensure that a non-equilibrium stationary state condition is properly set, we exploit the fact that in this condition the modulus of the heat flux injected into $|\mathbf{J}_i|$ and extracted from $|\mathbf{J}_e|$ the sample must be equal. For this reason, we monitored the relative difference $\frac{|\mathbf{J}_i|-|\mathbf{J}_e|}{|\mathbf{J}_i|}$, until such a quantity was negligibly small. Deviations from the asymptotic average zero value are considered as the error estimate in our heat flux.

Among the different definitions of thermal rectification (involving for example the estimate of thermal conductivity [107] or the ratio between the forward (*for*) and reverse (*rev*) thermal bias conditions [104]) we consider the most frequently one used in Literature [106, 110, 112, 48, 113, 114], namely

Thermal rectification definition based on heat fluxes

$$TR = \frac{|\mathbf{J}_{for}| - |\mathbf{J}_{rev}|}{|\mathbf{J}_{rev}|} \tag{7.1}$$

where the forward and reverse fluxes ($\mathbf{J}_{for}$ and $\mathbf{J}_{rev}$, respectively) are calculated as the average between the injected and

extracted flux in the corresponding thermal bias condition. In order to calculate TR we have to perform two simulations for each sample: (i) the left thermostat is initially set at temperature T_L while the right thermostat at temperature T_R, with $T_L < T_R$; (ii) the temperature gradient is inverted and the calculation is repeated for such an opposite bias condition. Fig.7.3 shows an example of the procedure we used to estimate TR in the case of sample B with $\Delta T = T_L - T_R$=100 K. The top panel shows in red (green) the energy injected (extracted) into (from) the sample by the hot (cold) reservoir. The middle panel shows the corresponding heat fluxes obtained as the time derivative of the energy divided by the cross-sectional area. The bottom panel shows the relative difference between the extracted and injected heat fluxes. Dashed black lines represent the time-average of all the corresponding quantities actually used to calculate TRs. Fig.7.3 clearly proves that a stationary regime of thermal conduction is eventually reached.

7.2.2 *TR in graphane/graphene nanoribbons*

By means of the procedure described above, we calculated thermal rectifications as a function of ΔT keeping the average temperature of each sample always at T=300 K. In detail, we set ΔT=100 K (T_{hot}=350 K and T_{cold}=250 K), 200 K (T_{hot}=400 K and T_{cold}=200 K), 300 K (T_{hot}=450 K and T_{cold}=150 K) and 400 K (T_{hot}=500 K and T_{cold}=100 K).

Fig.7.4 shows TR dependence on ΔT for sample A (black squares), B (blue circles) and C (red triangles) which by construction have the same dimension 30.8×23.8 nm^2. In all cases we observe a monotonic TR increase with respect to ΔT. Such a trend, which has been previously identified in many cases of shaped GNR (with no hydrogen) [115, 104], is analogous to the behaviour predicted by the nonlinear I-V characteristic curve in electric diodes. Stronger is the perturbation (in this case the temperature gradient), stronger is the non linear effect (in this case TR).

The maximum values of TRs, obtained for ΔT=400K, are $15.1 \pm 0.1\%$ for sample A, $20.1 \pm 0.2\%$ for sample B and $14.1 \pm 0.1\%$ for

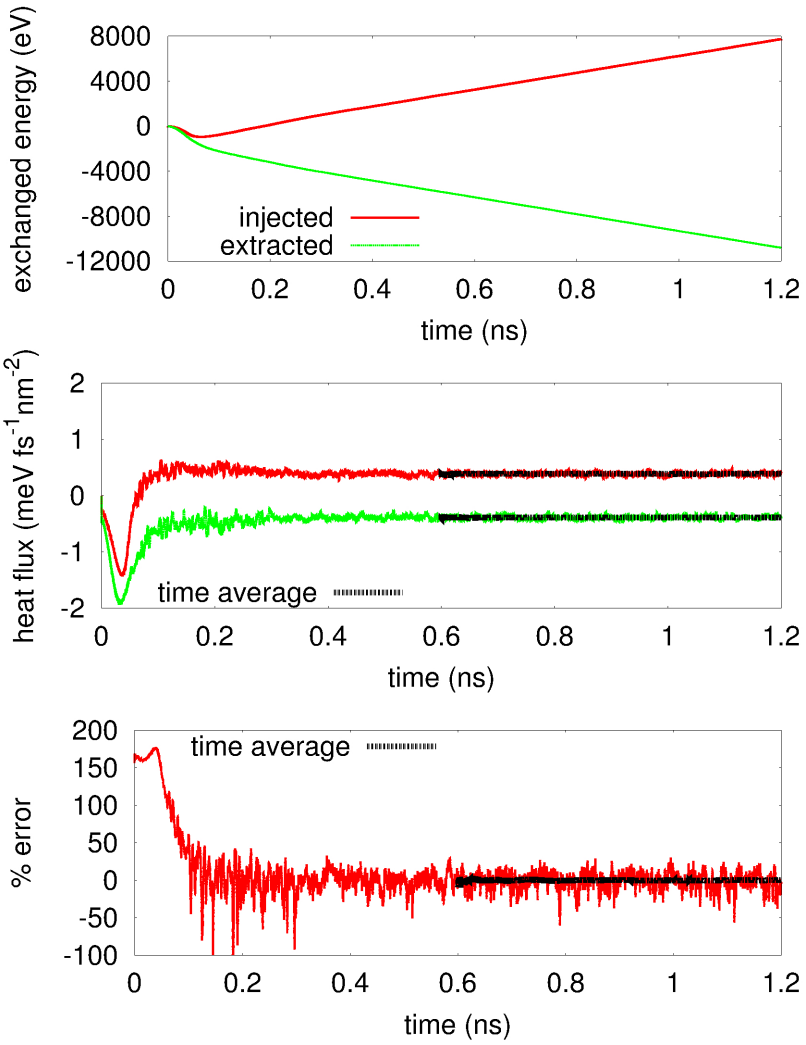

Figure 7.3: Top: injected (red) and extracted (green) energy in the case of sample B with $\Delta T = T_L - T_R$=100 K. Middle: time numerical derivative per unit cross-sectional area (heat fluxes) of injected (red) and extracted (green) energy. Bottom: relative difference between the extracted and the injected heat flux. Dashed black lines represent the time-average of all the corresponding quantities.

sample C. The present results show that the triangular graphane/-graphene nanoribbons are the best thermal rectifiers, similarly to previous findings on different shape asymmetric graphene nanoribbons[115].

Since the triangular junction shows the largest TR, we investigated its dependence upon sample size and vertex angle θ (see Fig.7.1, b). In detail, we considered a sample set with increasing length in the range 30.8 nm$\leqslant L_x \leqslant$ 123.4 nm, by preserving

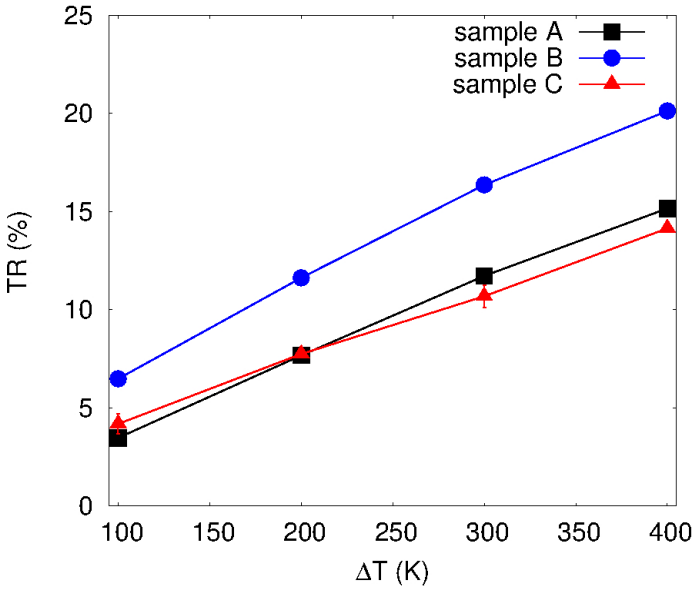

Figure 7.4: TR vs. ΔT for sample A (black squares), B (blue circles) and C (red triangles). The sample area is 30.8×23.8 nm^2.

the same aspect ratio. The vertex angle has been fixed to θ=40° and ΔT=400 K. The maximum number of atoms considered was $\sim 7 \times 10^5$.

Fig.7.5 (green triangles) shows the total rectification as a function of the sample length L_x. A linear relationship is observed in the length range explored, bringing to the highest rectification value TR=54 ± 4% for L_x=123.4 nm. Interestingly enough, sample A does not show a similar behavior: as a matter of fact, by varying L_x in the same range as above we obtained the very same TR value. This result is once again consistent with previous data [112]. In this latter, in fact, it has been proved that for a graphane/graphene planar junction, which in this case is supposed to be infinite, by increasing the ribbons dimension in the heat flux direction from 20 nm to 100 nm, no TR variation has been observed.

The different behavior of sample A and B suggests different physical mechanisms leading to thermal rectification. In particular, for model A this phenomenon is mainly related to the different temperature-dependence of the intrinsic thermal conductivity of the two materials (see after). For this reason, the overall TR is almost unaffected by the sample size. On the other hand,

the key feature of sample B is the increasing of the graphane/-graphene interface area for increasing L_x, which results in an overall rectification raise.

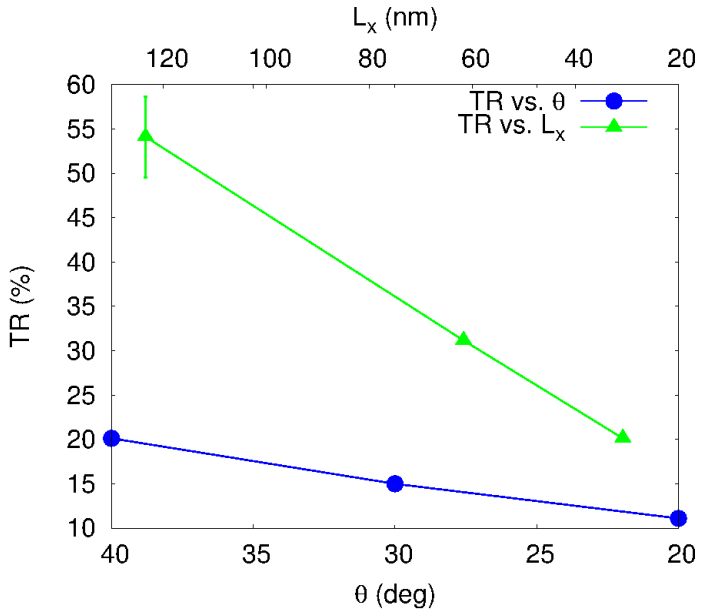

Figure 7.5: Rectification as a function of the sample length L_x (top axis) and vertex angle θ (bottom axis) for sample B with ΔT=400 K.

In order to disentangle the effect of the sample asymmetry on the total rectification, we explored the TR dependence on the vertex angle θ by keeping fixed the sample length L_x =30.8 nm and the sample width L_y=23.8 nm. Fig.7.5 (blue dots) shows that TR increases as θ increases from 20° to 40° due to an higher sample asymmetry (i.e. an higher ratio between the right and the left graphene edges). A similar trend has been observed in a pure triangular GNRs[105].

7.3 SAMPLE A: INTERFACE THERMAL RESISTANCE AND TR EXPLANATION

In order to rationalize the scenario presented, I first investigated the simplest case of sample A. As already pointed out by Ref.[112], an actual thermal resistance at the graphene/graphene interface is expected because of a remarkable interface phonon scattering. Fig.7.6 shows the temperature profile estimated in the non-equilibrium stationary condition in the case of the for-

ward (top) and reverse (bottom) bias for ΔT=400 K. In both cases we observe that graphane shows a much larger temperature slope with respect to graphene due to its reduced thermal conductivity [1]. Moreover, we observe an abrupt temperature discontinuity ΔT_{int} at the graphane/graphene interface, indicating the presence of an interface thermal resistance $R_{int} = \Delta T_{int}/|\mathbf{J}|$. The corresponding estimated values are R^{for}_{int}=4.0 $\times$ 10^{-11} ($m^2W^{-1}K$) and R^{rev}_{int}=5.1 $\times$ 10^{-11} ($m^2W^{-1}K$) respectively. We attribute the small variation between R^{for}_{int} and R^{rev}_{int} to the different interface temperatures occurring in the forward and reverse bias (see Fig.7.6).

Definition of interface thermal resistance

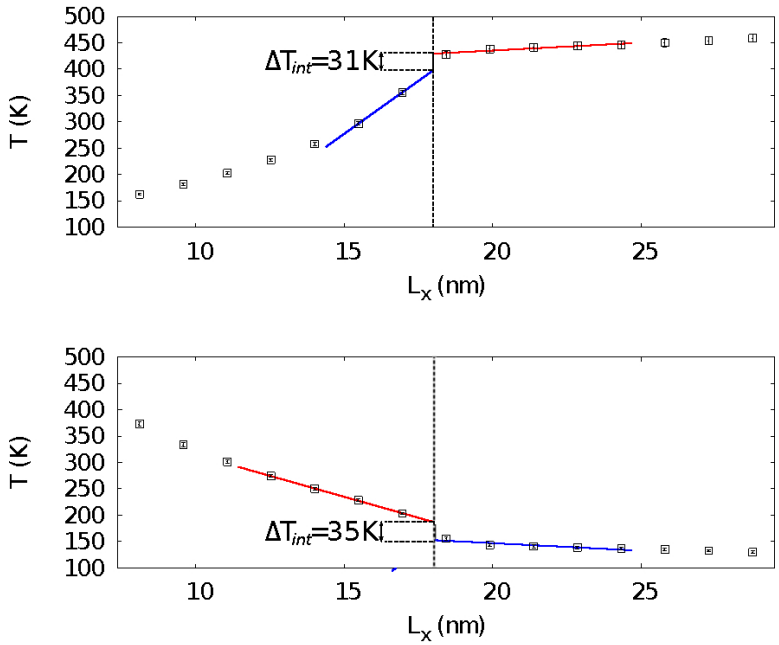

Figure 7.6: Temperature profile along sample A for the forward (top) and reverse (bottom) bias. The vertical black dashed line indicates the position at L_x=18.0 nm of the actual graphane (left) /graphene (right) interface.

The observed TR can be easily explained in terms of the different dependence of the thermal conductivity on temperature in the two materials [106]. To demonstrate this idea, we take into account the thermal conductivity of graphene and graphane estimated by solving the Boltzmann transport equation via DFT calculations in Ref.[41]. In the case of ΔT=400 K and forward bias (corresponding to T_L=100 K and T_R=500 K) we considered the graphane thermal conductivity $\kappa^{cold}_{graphane}$ at T=200 K

and the graphene thermal conductivity $\kappa^{hot}_{graphene}$ at T=400 K. Conversely, in the reverse bias (corresponding to T_L=500 K and T_R=100 K) we considered the graphane thermal conductivity $\kappa^{hot}_{graphane}$ at T=400 K and the graphene thermal conductivity $\kappa^{cold}_{graphene}$ at T=200 K. We accordingly estimate an effective thermal conductivity in forward and reverse bias condition as

$$\frac{1}{\kappa^{for}} \sim \frac{1}{2\kappa^{cold}_{graphane}} + \frac{R^{for}_{int}}{L_x} + \frac{1}{2\kappa^{hot}_{graphene}} \tag{7.2}$$

$$\frac{1}{\kappa^{rev}} \sim \frac{1}{2\kappa^{hot}_{graphane}} + \frac{R^{rev}_{int}}{L_x} + \frac{1}{2\kappa^{cold}_{graphene}} \tag{7.3}$$

by describing the system as a series of thermal resistances [106]. We obtained κ^{for}=803 W $m^{-1}K^{-1}$ and κ^{rev}=517 W $m^{-1}K^{-1}$, confirming that in the case of forward bias the thermal conduction is favoured.

7.4 PHONON TRANSMISSION AND ANALYSIS OF THE VIBRATIONAL DENSITY OF STATES

The previous analysis can be straightforwardly exploited only for simple planar junctions as in sample A. In the case of more complicated interface morphologies, such those found in samples B and C, it should be better consider interface phonon transmission as inferred by the analysis of the vibrational density of states (VDOS). In particular, by estimating the overlap between the VDOS calculated in neighbour sample regions, it is possible to qualitatively compare how phonons are transmitted along the sample in the forward and reverse bias. To this aim, we divided each sample in five different contiguous regions along the x direction (see Fig.7.7). For each of the five regions we calculated the corresponding VDOS by Fourier transforming the velocity autocorrelation function(see Chapter 5) in both the forward and reverse configurations. Finally, we estimated the VDOS overlap between neighbour regions.

Fig.7.8 shows an example of the VDOS overlap between different regions in sample B for the forward (top) and reverse

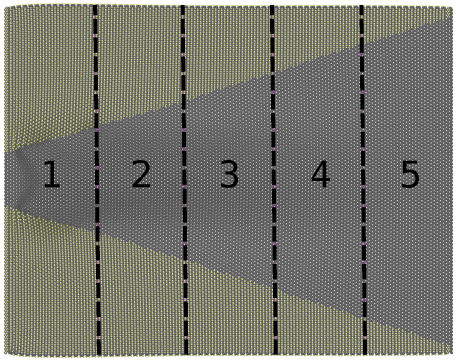

Figure 7.7: Schematic view of the 5 different contiguous regions where the VDOS was estimated in sample B.

(bottom) bias, while Fig.7.9 reports the resulting estimate of the VDOS overlap for all the systems here investigated.

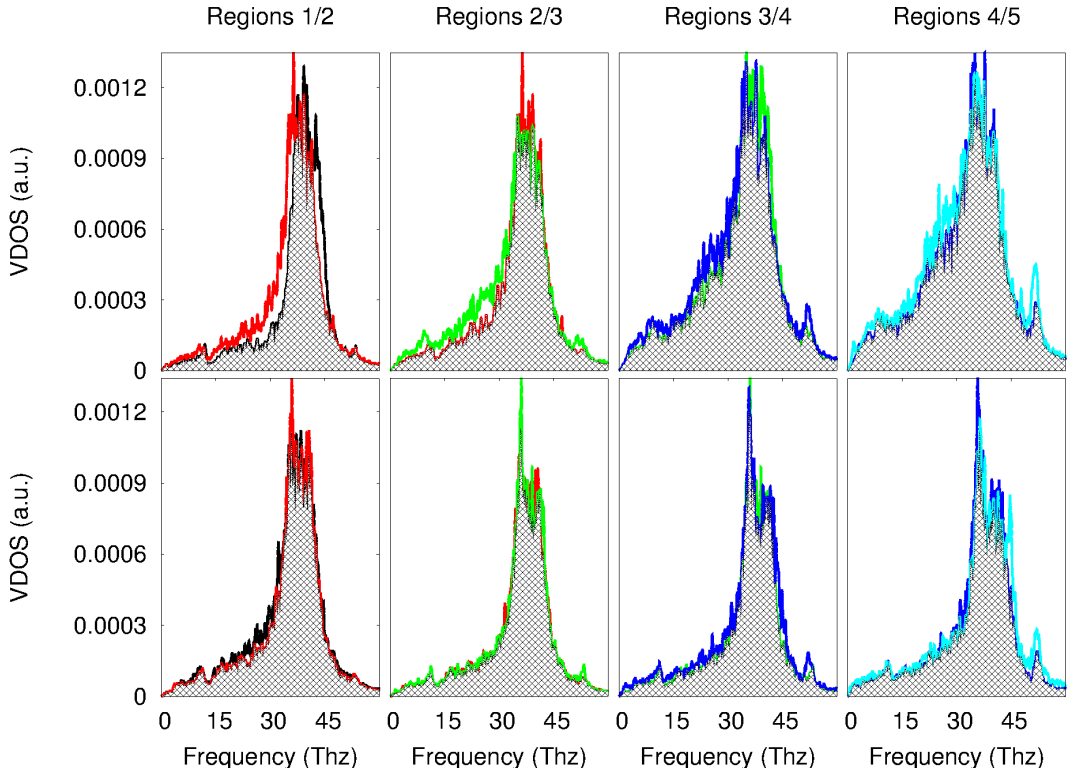

Figure 7.8: VDOS overlap between 5 different contiguous regions (1/2, 2/3, 3/4, 4/5) for sample B in the forward (top) and reverse (bottom) configurations. The black, red, green, blue and cyan lines are respectively to the VDOS calculated in region 1, 2, 3, 4, and 5. The filled patterned gray domain corresponds to the overlap area between two contiguous regions.

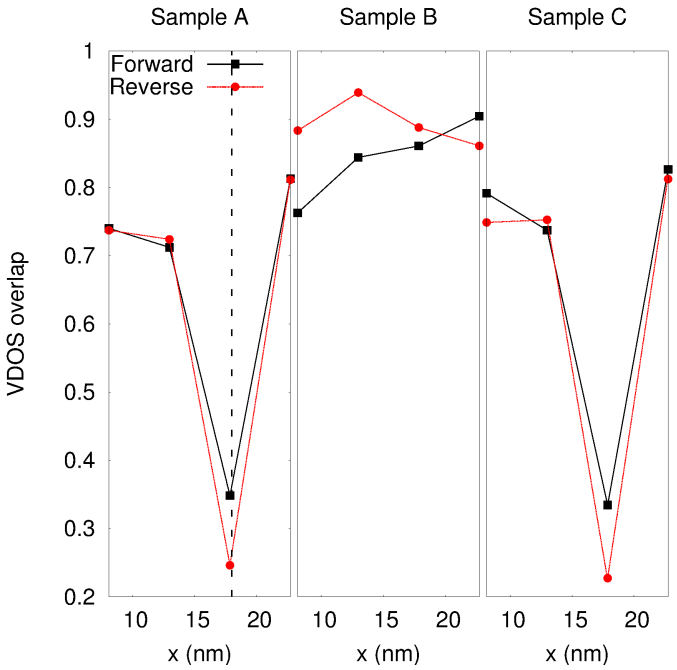

Figure 7.9: VDOS overlap magnitude along the x direction for sample A (left), B (center) and C (right) for forward (black squares) and reverse (red circles). The graphane/graphene interface in sample A at x=18.0 nm is indicated by a dashed line.

For sample A and C we observe an abrupt reduction of the VDOS overlap corresponding to the graphane/graphene interface which is located at x=18.0 nm. Interestingly enough, in both cases the VDOS reduction in the forward bias is smaller than the one in the reverse case, giving rise to an overall asymmetric phonon transport. On the other hand, for sample B the VDOS overlap increases (decreases) with x in the forward (reverse) case due to a different angular-dependent phonon transmission at the graphane/graphene interface. This last result justifies also the TR increase with L_x, which we have observed just in sample B.

7.5 EFFECTIVE CONTINUUM MODEL TO CALCULATE TR

Mathematical necessary condition for thermal rectification

In conclusion, I propose a thermal rectification analysis based on effective continuum model. A further rationalization of ther-

mal rectification effects, in fact, is obtained by considering the unidimensional heat equation in a steady-state condition:

$$\frac{d}{dx}\left[\kappa(x,T)\frac{dT(x)}{dx}\right]=0 \tag{7.4}$$

where $\kappa(x,T(x))$ is the thermal conductivity, which in our case depends on both temperature $T(x)$ and x. $T(x)$ is the temperature profile that, in the steady-state, only depends on x. By integrating Eq.7.4 we obtain:

$$\kappa(x,T(x))\frac{dT(x)}{dx}=-J \tag{7.5}$$

where the integration constant J, which is determined through the boundary conditions, is nothing but the heat flux. It has been recently demonstrated that a necessary condition for thermal rectification is that thermal conductivity must be a function of both x and T, and that this function must be non-separable [116].

In fact, in the case in which thermal conductivity is separable, it can be written as the product of two independent functions of the variables x and T, i.e. $\kappa(x,T)=A(x)\lambda(T)$. Therefore , by integrating Eq.7.5:

$$\int_{T_1}^{T_2}\lambda(T)dT=-J\int_{L_1}^{L_2}\frac{dx}{A(x)} \tag{7.6}$$

This can be rewritten to give the heat rate as

$$J=-\frac{\int_{T_1}^{T_2}\lambda(T)dT}{\int_{L_1}^{L_2}\frac{dx}{A(x)}} \tag{7.7}$$

To calculate rectification, the only difference between $\mathbf{J}_{for}$ and $\mathbf{J}_{rev}$ is that the boundary conditions in the integral of $\lambda(T)$ are reversed. Since reversing the limits changes the sign of the integral, it can be easily seen that the reversing of the boundary temperatures results in $\mathbf{J}_{for}=-\mathbf{J}_{rev}$ and $TR=0$. Therefore, it can be concluded that separable thermal conductivity is a sufficient condition for no thermal rectification i.e. if the thermal conductivity $\kappa(x,T)$ is separable, there is no TR.

Based on Eq.7.5, we want to model the thermal rectification in sample B, which is the one showing the largest TR as well as

a remarkable TR size dependence. Since we previously demonstrated [1] that κ of pristine graphene is more than one order of magnitude larger the the corresponding graphane one, we can assume that in sample B the heat flux will be mainly conveyed along the pristine graphene region, being suppressed in graphane. This is confirmed by Fig.7.10 (top line) where both the modulus (color map) and the orientation (vectors) of the in-plane heat flux $\mathbf{J}_{x-y}$ are shown for the forward (right) and reverse (left) bias. Conversely, Fig.7.10 (bottom line) proves that the out-of-plane component of the heat flux field $\mathbf{J}_z$ has an opposite behavior, showing a suppression in the graphene region. This allows the overall heat flux conservation along the whole sample.

Heat flux field by color map representation

LAMMPS code define a computation that calculates the heat flux vector based on contributions from atoms in the specified group. This can be used by itself to measure the heat flux into or out of a reservoir of atoms, or to calculate a thermal conductivity using the Green-Kubo formalism (see Chapter 3). The heat flux $\mathbf{J}$ is defined by:

$$\begin{aligned} \mathbf{J} &= \frac{1}{V}[\sum_i e_i \mathbf{v}_i - \sum_i \mathbf{S}_i \mathbf{v}_i] \\ &= \frac{1}{V}[\sum_i e_i \mathbf{v}_i - \sum_{i<j} (\mathbf{f}_{i,j} \cdot \mathbf{v}_j)\mathbf{x}_{i,j}] \\ &= \frac{1}{V}[\sum_i e_i \mathbf{v}_i + \frac{1}{2}\sum_{i<j} (\mathbf{f}_{i,j} \cdot (\mathbf{v}_i + \mathbf{v}_j))\mathbf{x}_{i,j}] \end{aligned} \tag{7.8}$$

where e_i in the first term of the equation is the per-atom energy. This is calculated by adding the computed per-atom kinetic energy and per-atom potential energy; $\mathbf{S}_i$ in the second term is the per-atom stress tensor. The tensor multiplies $\mathbf{v}_i$ as a 3x3 matrix-vector multiply to yield a vector. The vector $\mathbf{J}$ actually calculated by the code is an extensive quantity, meaning it scales with the number of atoms in the simulation. It must be divided by the appropriate volume to get a flux, which would then be an intensive value, meaning independent of the number of atoms in the simulation.

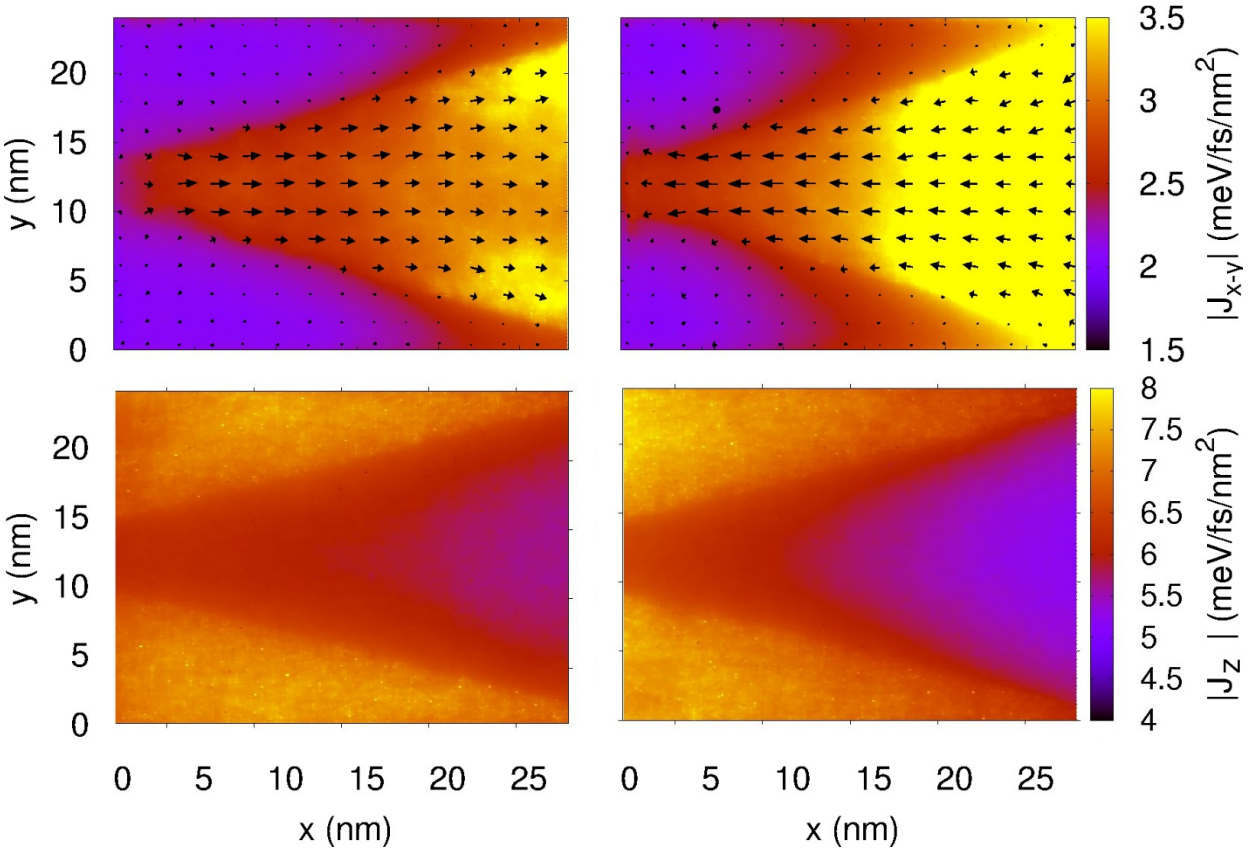

Figure 7.10: Modulus (color map) and vector field of $\mathbf{J}_{x-y}$ for sample B in the forward (left) and reverse (right) reservoirs configurations (top line). Modulus (color map) and vector field of $\mathbf{J}_z$ for sample B in the forward (left) and reverse (right) reservoirs configurations (bottom line)

In order to represent the vector field $\mathbf{J}_{x-y}$ in Fig.7.10 we have partitioned the simulation cell by 13×13 mesh. In each portion of such a mesh, the local value of $\mathbf{J}_{x-y}$ has been calculated by considering only the x and y components of the $\mathbf{J}$ computed with the precedent procedure. These locale $\mathbf{J}_{x-y}$ values have been therefore averaged over all atoms there contained for 200 ps. The same procedure is repeated for $\mathbf{J}_z$ in the out-of-plane direction.

Taking into account only the graphene active channel, the overall thermal conductivity will be a function of the temperature $T(x)$ and the slab height h which, in turns shows an x dependence for the specific case of the triangular shape. Such a $\kappa(h)$ dependence has been recently predicted in free-standing

graphene nanoribbons by means of the linearized Boltzmann transport equation [117]. Since the explicit analytical form of $\kappa(h(x))$ is not known, we consider an overall x-dependence as implicitly contained in $T(x)$. Therefore, in order to solve Eq.7.5 and estimate J, we need to find an analytical approximation for $\kappa(T)$. I fitted the data of Ref.[41] in the interval 100-500 K (where our atomistic simulations are performed) by a power series expansion to obtain the following analytical expression for $\kappa_{graphene}(T)$:

Temperature dependence of graphene thermal conductivity obtained by BTE

$$\kappa_{graphene}(T) = a_0 + a_1 T + a_2 T^2 + a_3 T^3 + O(T^4) \tag{7.9}$$

where: a_0=805736, a_1=−205.642, a_2 =0.467112 and a_3=−0.000363619. To a first approximation, we neglected the quadratic and cubic terms, which are about zero, and solved the following first order differential equation for both forward and reverse configurations:

$$[a_0 + a_1 T(x)]\frac{dT(x)}{dx} = -J \tag{7.10}$$

The solution for Eq.7.10 is:

$$T(x) = \frac{\sqrt{a_0 c - 2a_0 J x + a_1^2} - a_1}{a_0} \tag{7.11}$$

where c is a constant defined by the boundaries conditions. In the case of sample B with L_x=30.8 nm and ΔT=400 K, I used the solution $T(x)^{for}$ ($T(x)^{rev}$) for the forward (reverse) bias case to fit the corresponding temperature profile along the sample, obtaining J^{for} (J^{rev}). Fig.7.11 shows the fitting of $T(x)^{for}$ and $T(x)^{rev}$, together with the corresponding MD temperature profiles. The predicted TR=$\frac{J^{for}-J^{rev}}{J^{rev}}$ is 19.4% in very good agreement with the simulation result of 20.1%.

In conclusion in the work [3], we demonstrated that graphane/-graphene nanoribbons can be efficiently used as thermal diodes. In particular, we designed three kinds of thermal diodes based on different graphane/graphene junction morphologies (i.e. vertical, triangular and T-shaped) and we identified the triangular junction as the one with the highest thermal rectification of $\sim$ 54%. Moreover, we explored the dependence of thermal

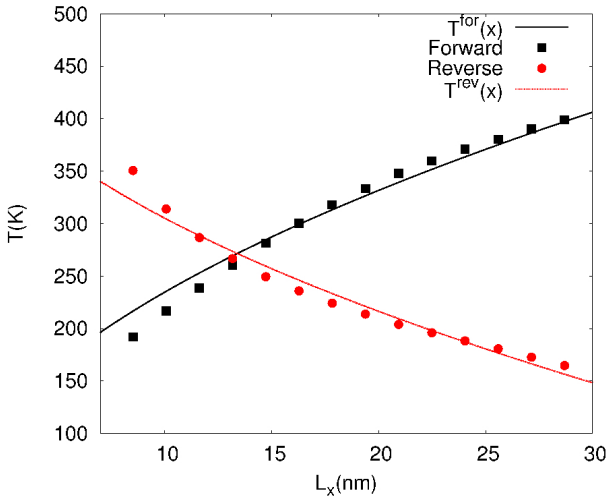

Figure 7.11: Temperature profiles along sample B with L_x=30.8 nm and ΔT=400 for the forward (black squares) and reverse (red circles) bias together with the corresponding analytical solutions of Eq.7.11: $T(x)^{for}$ (black line) and $T(x)^{rev}$ (red line).

rectification upon thermal gradient, showing an overall TR increase for all the three kinds of diodes, while we observed a significant TR increase with size only for the triangular one. We explored the size and vertex angle thermal rectification dependence for the triangular junction finding an increase with both of them. We also investigated the physical reasons behind thermal rectifications in terms of interface thermal resistance and different temperature-dependence of the thermal conductivity in graphane and graphene for the vertical junction. For more complicated junctions, such as the triangular and T-shaped, we compared phonon transmission along the sample in the forward and reverse configurations in terms of a vibrational density of states analysis. A further razionalization of thermal rectification has been proposed by using an effective continuum model based on the steady-state heat equation solution, which is able to quantitatively estimate thermal rectification for a graphane/-graphene triangular junction.

Part V

CONCLUSIONS

8

CONCLUSIONS AND FUTURE DIRECTION

In this thesis I investigated the thermal properties of graphene and graphene-based systems by means of non equilibrium molecular dynamics simulations.

As a first analysis, I addressed the issue of calculating thermal conductivity in mono-layer pristine graphene. An innovative method with respect to the mainly common equilibrium molecular dynamics (EMD) and non-equilibrium Müller and Plate method, named "Approach to equilibrium" (AEMD) has been used. This technique has been previously tested for other bulk materials [52] and in this work applied for the first time to graphene [2]. By using this approach, we are able to simulate the system evolution from a non equilibrium condition, in which a temperature gradient is imposed upon the sample, through an equilibrium state where the temperature distribution is uniform along the system. In the initial non-equilibrium state, a step-like temperature profile has been set. We used the solution in terms of harmonic functions of the well-known heat equation to fit the temperature difference $\Delta T(t)$ between the two sides (left and right) of the sample. By using this procedure, the sample thermal diffusivity is obtained. The purpose of this work is to address the dependence of κ on the sample length in the direction of heat transfer, definitively solving the active debate about the infinite sample length extrapolation. We address this issue by avoiding any guess or approximation on the underlying microscopic heat transport mechanisms; we rather perform direct atomistic simulations aimed at estimating thermal conductivity in samples with increasing size up to the unprecedented value of $L_x = 0.1$ mm. In fact, our goal is to provide evidence that thermal conductivity in graphene is definitely upper limited in samples long enough to allow a diffusive transport regime for both single and collective phonon

excitations. Finally, our data are compared with the *ab-initio* results, obtained by exactly solving the Boltzmann transport equation [41]. The excellent agreement shown is the clear prove that a diffusive-to-ballistic crossover has been approached at about $L_x = 0.1mm$ as indeed proposed in the *ab-initio* analysis. The longer characteristic length at which a pure diffusive phonon behavior is experienced has been explained as due to the longer mean-free-path (MFP) of phonon collective excitations with respect to the single phonon mode MFP. These collective phonon behavior has been guessed to affect the graphene thermal transport much more strongly with respect to other bulk materials even at room temperature. For this reasons, a further investigation could be suggested in order to explore the hydrodynamical regime in graphene where such collective excitations dominate the heat transport. Moreover, the discussion in our work could stimulate experimental efforts in order to measure thermal conductivity on mm-long samples.

Continuing in the framework of pristine graphene thermal characterization, in Chapter 5 I focused on the transient response to a laser beam excitation on a circular graphene sample. This is a crucial topic since many experimental methods rely on optical sources in order to provide heating power. In our work [4] the heat absorption due to the laser spot has been mimicked by reproducing the excitation of the $K - A_1'$ and $\Gamma - E_{2g}$ optical phonon modes, which are the ones who experience the strongest coupling with photo-generated electrons [118]. In this case, the previously used AEMD simulation technique has been implemented by fitting the time evolution of temperature profile $T(r,t)_{sim}$, instead of $\Delta T(t)$. Eventually, the solution of the radial heat equation $T(r,t)_{theo}$ is used to fit the simulation $T(r,t)_{sim}$. The estimated thermal conductivity shows a dependence on the kind of thermalization procedure used. In particular, we compare the κ resulting from a "white" spot thermalization procedure, where all the degrees of freedom have been thermalized, with the corresponding $\kappa_{colored}$, obtained by selecting a single phonon mode within the spot . In both cases of $K - A_1'$ and $\Gamma - E_{2g}$ excited modes, the κ is shown to be

dramatically reduced with respect to the fictitious "white" thermostat procedure. Moreover, $\kappa_{colored}$ is much less sensitive to both temperature and size. With the aim of elucidating such differences, we analyzed the time dependent vibrational density of states in all the cases. The VDOS analysis has been reveled to be very useful because it allows to distinguish the different decay channels of the two considered optical phonon modes, explaining why the thermal transport behavior in these single-mode cases is different with respect to the case in which all the phonon modes are equally excited. In particular, we observe that the colored phonon population remains far from the equilibrium during the whole simulation, giving rise to a completely different thermal transport mechanism.

On the other side, we must point out that by comparing the temperature difference between the spot and the rest of the sample $\Delta T(t)_{sper}$ and the corresponding $\Delta T(t)_{theo}$ predicted by heat equation solutions, some discrepancies have been noticed in the first simulation time-steps. This last feature could be interpreted in the framework of the recently observed thermal transport hydrodynamic regime in graphene, by instance responsible of the collective phonon excitation whose importance has been cited in our precedent work. In this sense a future direction of investigation could be to consider the complete heat transport equation behind the Fourier formalism in order to explore such anomalies.

In the second part of this thesis, I focused on the hydrogenated graphene systems. In particular, we studied [1] the effects of hydrogenation on graphene thermal properties such as thermal conductivity and phonon vibrational density of state. The ordered hydrogenated graphene characterized by 1:1 ratio between C and H atoms, namely graphane, has been considered. The three most stable graphane isomers (B-, C-, and W-graphane) [76], differing in the specific position of H atoms with respect to the C lattice, have been analyzed. AEMD simulations have been performed on samples with increasing lengths L_x in the direction of the heat flux. In the length range here explored it is definitely true that $\kappa(L_x) \sim \log(L_x)$. The presence of Hydrogen

drastically changes the overall graphane thermal conductivity, that is reduced with respect to pristine graphene by more than one order of magnitude for all the isomers and in both armchair and zigzag transport directions. Moreover, a small anisotropy has been observed between armchair and zigzag directions as due to the simulation cell finiteness. The isomer which shows the largest reduction is W-graphane.

We explained this reduction in terms of different vibrational density of states (VDOS) and dispersion curves. We observed a reduction of the peaks intensity in the acoustic range of graphane VDOS and a reduced group velocity of the TA and LA acoustic modes in phonon dispersion curve. In addition, we correlated the κ decrease with the increasing out-of-plane oscillation amplitude, due to the sp2-sp3 bond transition upon hydrogenation. In this scenario, another possibility should be exploiting other Hydrogen isomers, for example Deuterium, a heavier isotope containing a neutron in addition to a proton. It has been already proved that the graphene deuteration reaction proceeds faster than hydrogenation [119] and that the electronic structure is modified, a tuneable electron energy gap can be induced, by both hydrogenation and deuteration. To the best of my knowledge, there are no works addressing the thermal properties of the deuterated graphane. However, it is reasonable that, by considering a heavier isotope , the phonon spectra should be more strongly modified . In particular, a lowering of the high frequency modes should be aspected.

Finally, we propose an useful application of the previously observed graphene thermal conductivity reduction upon hydrogenation by designing a novel thermal diodes based on graphane/-graphene interface [3]. Such a thermal device can be potentially applied in the framework of thermal management in electronics as well as in logic circuits based on phononic instead of electronic information. We considered three kinds of graphene/-graphane nanoribbons with different interface morphologies: vertical, triangular and T-shape junctions. For all of these a complete characterization has been performed in terms of thermal rectification coefficient (TR). In detail, to calculate thermal recti-

fication, a NEMD simulation has been performed in which we imposed a stationary thermal conduction regime and then calculated the corresponding heat flux. A quantitative difference between heat flux magnitude in one temperature gradient direction ("forward") with respect to the "reverse" temperature gradient has been observed, identifying the typical non-linear effect characteristic of a diode. The highest thermal rectification has been obtained in the case of triangular junction, reaching a value of 54%. Moreover, we showed an overall TR increase with ΔT for all the three kinds of diodes and a significant TR increase with size only for the triangular junction. In the case of this largely efficient triangular junction, we also explored the thermal rectification dependence on the vertex angle: an increase with its has been observed, that could be seen as an evidence of the importance of anisotropy in such non-linear phenomena.

Such an observed TR has been discussed by considering different physical reasons. In the case of vertical junction the phenomenon is explained in terms of interface thermal resistance and different temperature-dependence of the thermal conductivity between graphane and graphene. On the other side, for the triangular and T-shaped junctions, we compared phonon transmission along the sample in the forward and reverse configurations by a vibrational density of states analysis. The overlap between VDOS in contiguous regions along the sample, actually, gives an indication about how phonons are transmitted in the forward and reverse bias.

Our final goal is to propose an analysis of thermal rectification in triangular junction based on an effective continuum model, which is only based on the steady state temperature profile, rather than the actual heat flux. The model quantitatively predicts thermal rectification (TR= 19.4%) in very good agreement with the standard analysis (20.1%) based on the heat flux. We remark the convenience of working with simple continuum model which allows to quickly estimate thermal rectifications at a negligible computational cost. In particular such a model has been developed in order not to be explicitly dependent on the materials atomic structure since the only inputs needed are the

analytical form for $\kappa(T)$ (which can be easily obtained from previous experimental or theoretical data) and the actual shape of the sample.

Part VI

APPENDIX

A

APPENDIX

A.1 CLASSICAL SPECIFIC HEAT AND QUANTUM CORRECTIONS IN GRAPHENE

In order to obtain the thermal conductivity κ from the thermal diffusivity α computed in AEMD simulation, the formula $\alpha = \frac{\kappa}{\rho C_V}$ is used, where the graphene volumetric heat capacity C_V must be inserted.

Actually we know that the total energy in an harmonic crystal with N atoms has the form

$$E = \sum_{\mathbf{k},s} (n_{\mathbf{k},s} + \frac{1}{2}) \hbar \omega_s(\mathbf{k}) \tag{A.1}$$

where $n_{\mathbf{k},s}$ and $\omega_s(\mathbf{k})$ are the number and the frequencies of modes with momentum $\mathbf{k}$ in the s branch. Moreover in a quantum system the thermal energy density u can be written as

$$u = u_{eq} + \frac{1}{V} \sum_{\mathbf{k},s} \frac{1}{2} \hbar \omega_s(\mathbf{k}) + \frac{1}{V} \sum_{\mathbf{k},s} \frac{\hbar \omega_s(\mathbf{k})}{exp(-\frac{\hbar \omega_s(\mathbf{k})}{K_B T}) - 1} \tag{A.2}$$

where u_{eq} is the energy of the equilibrium configuration. In the quantum theory of an harmonic solid, the specific heat is then

$$C_V = \frac{1}{V} \sum_{\mathbf{k},s} \frac{\partial}{\partial T} \frac{\hbar \omega_s(\mathbf{k})}{exp(-\frac{\hbar \omega_s(\mathbf{k})}{K_B T}) - 1} \tag{A.3}$$

In the case $K_B T/\hbar$ is larger with respect to all the phonon frequencies i.e. when every normal mode is in a highly excited state, we can expand Eq.A.3 obtaining $C_V = 3\frac{N}{V} K_B$ which is the classical form for the specific heat of a N-atomic system derived by Dulong and Petit, while additional terms in the expansion give the quantum correction to the specific heat at temperature high enough for the expansion to be valid. On the other side for

intermediate and low temperature another form must be found. One extrapolation historically used is due to Debye

$$C_V = \frac{\partial}{\partial T}\frac{3\hbar c}{2\pi^2}\int_0^{\mathbf{k}_D}\frac{\mathbf{k}^3 d\mathbf{k}}{exp\frac{\hbar c\mathbf{k}}{K_B T}-1} \tag{A.4}$$

where a linear dispersion $\omega_{\mathbf{k}} = c\mathbf{k}$ for all the branches has been guessed. It is convenient to define a phonon frequency ω_D to which corresponds the maximum momentum k_D. We define from these, $\Theta_D = \hbar\omega_D/K_B = \hbar c\mathbf{k}_D/K_B$, which is called Debye temperature and it is a measure of the temperature above which all modes begin to be excited and below which modes begin to be frozen out. Eq.A.4 can be rewritten in terms of Debye temperature as

$$C_V = \frac{\partial}{\partial T}\frac{3\hbar c}{2\pi^2}\int_0^{\mathbf{k}_D}\frac{\mathbf{k}^3 d\mathbf{k}}{exp\frac{\hbar c\mathbf{k}}{K_B T}-1} = 3NK_B\, q(\frac{\Theta_D}{T}) \tag{A.5}$$

In the AEMD simulations generally, the classical approximation by Dulong and Petit is used for the specific heat. This choice is coherent with the classical nature of MD simulation, in which the phonon distribution is the classical one and not the corresponding quantum Bose-Einstein distribution. In fact, Fig.A.1 shows the total energy during a NVE run in function of the system temperature T (for T=290,295,300,305,310 K) for a graphene sample with N=480 atoms performed by using empirical Tersoff potential. The black line is the data fitting function, whose T-derivative gives the value of C_V, according to the basic definition $C_V = \frac{\partial u}{\partial T}$. The value obtained by means of this simple procedure is $C_V \cdot V = 0.129958\frac{eV}{K}$ very similar to $C_V \cdot V = 0.12384\frac{eV}{K}$ which is the Dulong and Petit prediction for the same system.

However, in graphene the maximum values of frequencies for the planar and the Z modes are found to be, respectively, 3.01 and 1.68 in units of 10^4 Hz. These values correspond to Debye temperatures 2300 and 1287 K, respectively [120]. All the simulations shown in this thesis are performed at an average temperature of 300 K. This temperature is largely below the graphene Debye temperatures Θ_D=1000-2300 K. Therefore, we should discuss the amount of error involved in using the classical approximation to phonon occupation statistics.

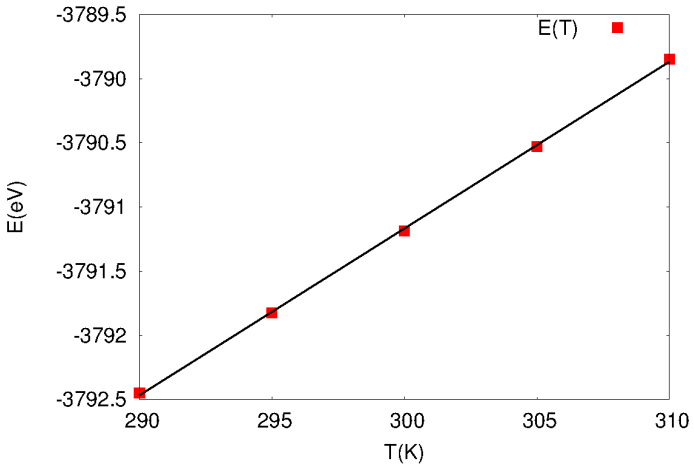

Figure A.1: Total energy E for graphene system at T=290,295,300,305,310 K together with the corresponding fitting function. The angular coefficient obtained by the fit is a=0.129958.

In particular, because it represents the total energy of the crystal weighted by the respective phonon population, the volumetric specific heat of the solid gives a good indication of the errors done by considering the classical approximation.

In Ref.[121] the ratio of the computed specific heat using classical statistics and Bose-Einstein (BE) statistics is showed for different temperatures, stating that the classical approximation clearly over predicts the total specific heat by more than three times at room temperature.

At every temperature, the Dulong and Petit value is always greater than the corresponding value obtained from BE statistics, and they converge one to each other in the high-temperature limit.

In order to overcome this problem, generally, in graphene some quantum corrections are added to the calculation in order to improve the MD classical predictions. In detail, the κ is computed from the calculated α by using $\kappa = \alpha C_V \rho q$. This last q depends on the temperature T at which the simulation is performed and in particular on the ratio between T and Θ_D which in our case is 0.15. The quantum correction is based on Eq.A.4 and the tabular value for q is taken from Ref.[122] and it is equal to 0.213 for graphene at T=300 K.

In Chapter 4 and 6 we use such corrections, in the first case for sake of convenience to facilitate the comparison with other literature results in which these are generally used, in the latter to obtain a more realistic graphane κ estimate (which has been measured for the first time in our work), within the limitation of the empirical potential used. On the other side, we discarded the quantum correction in the Chapter 5, since in this case we are mainly interested in the relative difference in κ measures according to the different thermalization techniques rather that to its exact absolute value.

BIBLIOGRAPHY

[1] Giuliana Barbarino, Claudio Melis, and Luciano Colombo. *Carbon*, 80:167, 2014.

[2] Giuliana Barbarino, Claudio Melis, and Luciano Colombo. *Physical Review B*, 91(3):035416, 2015.

[3] Claudio Melis, Giuliana Barbarino, and Luciano Colombo. *Physical Review B*, 92(24):245408, 2015.

[4] Giuliana Barbarino, Giorgia Fugallo, Claudio Melis, Francesco Mauri, and Luciano Colombo, 2016.

[5] K S Novoselov, A K Geim, S V Morozov, D Jiang, Y Zhang, S V Dubonos, I V Grigorieva, and A A Firsov. *Science (New York, N.Y.)*, 306(5696):666, 2004.

[6] Gordon E. Moore. Moore's law at 40. In *Understanding Moore's Law: Four Decades of Innovation*. 2006.

[7] Alexander A. Balandin. *IEEE Potentials*, 21(1):11, 2002.

[8] Alexander A. Balandin, Suchismita Ghosh, Wenzhong Bao, Irene Calizo, Desalegne Teweldebrhan, Feng Miao, and Chun Ning Lau. *Nano Letters*, 8(3):902, 2008.

[9] S. Ghosh, I. Calizo, D. Teweldebrhan, E. P. Pokatilov, D. L. Nika, A. A. Balandin, W. Bao, F. Miao, and C. N. Lau. *Applied Physics Letters*, 92(15):151911, 2008.

[10] A. A. Balandin, S. Ghosh, D. L. Nika, and E. P. Pokatilov. *Fullerenes, Nanotubes and Carbon Nanostructures*, 18(4-6): 474, 2010.

[11] Suchismita Ghosh, Wenzhong Bao, Denis L Nika, Samia Subrina, Evghenii P Pokatilov, Chun Ning Lau, and Alexander A Balandin. *Nature Materials*, 9(7):555, 2010.

[12] N. D. Mermin. *Physical Review*, 176(1):250, 1968.

[13] Herbert Wagner and U. Schollwoeck. *Scholarpedia*, 5(10): 9927, 2010.

[14] Pierre Le Doussal and Leo Radzihovsky. *Physical Review Letters*, 69(8):1209, 1992.

[15] Jannik C. Meyer, A. K. Geim, M. I. Katsnelson, K. S. Novoselov, T. J. Booth, and S. Roth. *Nature*, 446(7131):60, 2007.

[16] R. C. Thompson-Flagg and et Al. *EPL (Europhysics Letters)*, 85(4):46002, 2009.

[17] A. Fasolino, J. H. Los, and M. I. Katsnelson. *Nature Materials*, 6(11):858, 2007.

[18] A. K. Geim and K. S. Novoselov. *Nature Materials*, 6(3):183, 2007.

[19] Ning Wei, Lanqing Xu, Hui-Qiong Wang, and Jin-Cheng Zheng. *Nanotechnology*, 22(10):105705, 2011.

[20] Alexander A Balandin. *Nature Materials*, 10(8):569, 2011.

[21] Yanan Yue and Xinwei Wang. *Nano reviews*, 3:11586, 2012.

[22] J. M. Ziman and H. L. Armstrong. *American Journal of Physics*, 33(4):349, 1965.

[23] Daniel R. Cooper, Benjamin DAnjou, Nageswara Ghattamaneni, Benjamin Harack, Michael Hilke, Alexandre Horth, Norberto Majlis, Mathieu Massicotte, Leron Vandsburger, Eric Whiteway, and Victor Yu. *ISRN Condensed Matter Physics*, 2012:501686, 2012.

[24] S. Bernard, E. Whiteway, V. Yu, D. G. Austing, and M. Hilke. *Physical Review B*, 86(8):085409, 2012.

[25] Pedro Venezuela, Michele Lazzeri, and Francesco Mauri. *Physical Review B*, 84(3):035433, 2011.

[26] Denis L Nika and Alexander a Balandin. *Journal of physics Condensed matter*, 24(23):233203, 2012.

[27] Jae Hun Seol, Insun Jo, Arden L Moore, Lucas Lindsay, Zachary H Aitken, Michael T Pettes, Xuesong Li, Zhen Yao, Rui Huang, David Broido, Natalio Mingo, Rodney S Ruoff, and Li Shi. *Science (New York, N.Y.)*, 328(5975):213, 2010.

[28] L. Lindsay, D. A. Broido, and Natalio Mingo. *Physical Review B*, 82(11):115427, 2010.

[29] Dhruv Singh, Jayathi Y. Murthy, and Timothy S. Fisher. *Journal of Applied Physics*, 110(4):044317, 2011.

[30] L. Lindsay, W. Li, J. Carrete, N. Mingo, D. A. Broido, and T. L. Reinecke. *Physical Review B*, 89(15):155426, 2014.

[31] Nicola Bonini, Jivtesh Garg, and Nicola Marzari. *Nano Letters*, 12(6):2673, 2012.

[32] Yee Kan Koh, Myung Ho Bae, David G. Cahill, and Eric Pop. *Nano Letters*, 10(11):4363, 2010.

[33] D. L. Nika, E. P. Pokatilov, A. S. Askerov, and A. A. Balandin. *Physical Review B*, 79(15):155413, 2009.

[34] L. Lindsay and D. A. Broido. *Physical Review B*, 81(20): 205441, 2010.

[35] Lorenzo Paulatto, Francesco Mauri, and Michele Lazzeri. *Physical Review B*, 87(21):214303, 2013.

[36] Shanshan Chen, Qingzhi Wu, Columbia Mishra, Junyong Kang, Hengji Zhang, Kyeongjae Cho, Weiwei Cai, Alexander A. Balandin, and Rodney S. Ruoff. *Nature Materials*, 11 (3):203, 2012.

[37] I Calizo, A A Balandin, W Bao, F Miao, and C N Lau. *Nano letters*, 7(9):2645, 2007.

[38] W. Jang, W. Bao, L. Jing, C. N. Lau, and C. Dames. *Applied Physics Letters*, 103(13):133102, 2013.

[39] Wanyoung Jang, Zhen Chen, Wenzhong Bao, Chun Ning Lau, and Chris Dames. *Nano Letters*, 10(10):3909, 2010.

[40] Jiaqi Guo, Xinwei Wang, David B. Geohegan, and Gyula Eres. *Functional Materials Letters*, 01(01):71, 2008.

[41] Giorgia Fugallo, Andrea Cepellotti, Lorenzo Paulatto, Michele Lazzeri, Nicola Marzari, and Francesco Mauri. *Nano letters*, 14(11):6109, 2014.

[42] Luiz Felipe C. Pereira and Davide Donadio. *Physical Review B*, 87(12):125424, 2013.

[43] Xiangfan Xu, Luiz F C Pereira, Yu Wang, Jing Wu, Kaiwen Zhang, Xiangming Zhao, Sukang Bae, Cong Tinh Bui, Rongguo Xie, John T L Thong, Byung Hee Hong, Kian Ping Loh, Davide Donadio, Baowen Li, and Barbaros Özyilmaz. *Nature Communications*, 5(3689), 2014.

[44] William J. Evans, Lin Hu, and Pawel Keblinski. *Applied Physics Letters*, 96(20):203112, 2010.

[45] Xin Mu, Xufei Wu, Teng Zhang, David B Go, and Tengfei Luo. *Scientific Report*, 4(3909), 2014.

[46] Zhen Wah Tan, Jian-Sheng Wang, and Chee Kwan Gan. *Nano Letters*, 11(1):214, 2011.

[47] Qing-Xiang Pei, Zhen-Dong Sha, and Yong-Wei Zhang. *Carbon*, 49(14):4752, 2011.

[48] Wei Rong Zhong, Mao Ping Zhang, Bao Quan Ai, and Dong Qin Zheng. *Applied Physics Letters*, 98(11):113107, 2011.

[49] Hengji Zhang, Geunsik Lee, and Kyeongjae Cho. *Physical Review B*, 84(11):115460, 2011.

[50] Patrick K. Schelling, Simon R. Phillpot, and Pawel Keblinski. *Physical Review B*, 65(14):144306, 2002.

[51] Florian Müller-Plathe. *Journal of Chemical Physics*, 106(14): 6082, 1997.

[52] Claudio Melis and Luciano Colombo. *Physical Review Letters*, 112(6):065901, 2014.

[53] E. Lampin, P. L. Palla, P. A. Francioso, and F. Cleri. *Journal of Applied Physics*, 114(3):033525, 2013.

[54] Sha Liu, X. F. Xu, R. G. Xie, Gang Zhang, and B. W. Li. *European Physical Journal B*, 85:337, 2012.

[55] Baowen Li, Lei Wang, and Giulio Casati. *Physical Review Letters*, 93(18):184301, 2004.

[56] Baowen Li, Lei Wang, and Giulio Casati. *Applied Physics Letters*, 88(14):143501, 2006.

[57] Nianbei Li, Jie Ren, Lei Wang, Gang Zhang, Peter Hänggi, and Baowen Li. *Reviews of Modern Physic*, 84(3):1045, 2012.

[58] Jorge Sofo, Ajay Chaudhari, and Greg Barber. *Physical Review B*, 75(15):153401, 2007.

[59] D. C. Elias, R. R. Nair, T. M. G. Mohiuddin, S. V. Morozov, P. Blake, M. P. Halsall, and et al. *Science*, 323(5914):610, 2009.

[60] Steve Plimpton. *Journal of Computational Physic*, 117(1):1, 1995.

[61] Frank P. Incropera, David P. DeWitt, Theodore L. Bergman, and Adrienne S. Lavine. *Fundamentals of Heat and Mass Transfer*, volume 6. 2007.

[62] J. M. Ziman. *Electrons and Phonons: The Theory of Transport Phenomena in Solids*, volume 20. 1960.

[63] Daan Frenkel and Berend Smit. *Understanding Molecular Simulation*, volume 2. 2002.

[64] Loup Verlet. *Physical Review*, 159(1):98, 1967.

[65] R. W. Hockney. The potential calculation and some applications. In *Methods in Computational Physics*, volume 9. 1970.

[66] J. Tersoff. *Physical Review B*, 38(14):9902, 1988.

[67] S. J. Stuart, A. B. Tutein, and J. A. Harrison. *The Journal of Chemical Physics*, 112(14):6472, 2000.

[68] Donald W Brenner, Olga A Shenderova, Judith A Harrison, Steven J Stuart, Boris Ni, and Susan B Sinnott. *Journal of Physics: Condensed Matter*, 14(4):783, 2002.

[69] Boris Ni, Ki-Ho Lee, and Susan B Sinnott. *Journal of Physics: Condensed Matter*, 16(41):7261, 2004.

[70] Melville S. Green. *The Journal of Chemical Physics*, 22(3): 398, 1954.

[71] Ryogo Kubo. *Journal of the Physical Society of Japan*, 12(6): 570, 1957.

[72] Yuping He, Ivana Savic, Davide Donadio, and Giulia Galli. *Physical Chemistry Chemical Physics*, 14(47):16209, 2012.

[73] J. E. Turney, E. S. Landry, A. J. H. McGaughey, and C. H. Amon. *Physical Review B*, 79(6):064301, 2009.

[74] Claudio Melis, Riccardo Dettori, Simon Vandermeulen, and Luciano Colombo. *European Physic Journal B*, 87(4): 96, 2014.

[75] Carlos Campana and Martin H. Muser. *Physic Reviev Letters*, 74(7):075420, 2006.

[76] Emiliano Cadelano, Pier Luca Palla, Stefano Giordano, and Luciano Colombo. *Physical Review B*, 82(23):235414, 2010.

[77] P. G. Klemens and D.F. Pedraza. *Carbon*, 32(4):735, 1994.

[78] P. G. Klemens. *International Journal of Thermophysic*, 22(1): 265, 2001.

[79] D. L. Nika, S. Ghosh, E. P. Pokatilov, and A. A. Balandin. *Applied Physic Letters*, 94(20):203103, 2009.

[80] B. D. Kong, S. Paul, M. Buongiorno Nardelli, and K. W. Kim. *Physical Review B*, 80(3):033406, 2009.

[81] Yulu Shen, Guofeng Xie, Xiaolin Wei, Kaiwang Zhang, Minghua Tang, Jianxin Zhong, Gang Zhang, and Yong Wei Zhang. *Journal of Applied Physics*, 115(6):063507, 2014.

[82] R. A. Guyer and J. A. Krumhansl. *Physical Review*, 148(2): 766, 1966.

[83] Jae Ung Lee, Duhee Yoon, Hakseong Kim, Sang Wook Lee, and Hyeonsik Cheong. *Physical Review B*, 83(8):081419, 2011.

[84] H Cabrera, D Mendoza, J L Benítez, C Bautista Flores, S Alvarado, and E Marín. *Journal of Physics D: Applied Physics*, 48(46):465501, 2015.

[85] C. C. Ackerman, B. Bertman, H. A. Fairbank, and R. A. Guyer. *Physical Review Letters*, 16(18):789, 1966.

[86] V. Narayanamurti and R. C. Dynes. *Physical Review Letters*, 28(22):1461, 1972.

[87] Howard E. Jackson, Charles T. Walker, and Thomas F. McNelly. *Physical Review Letters*, 25(1):26, 1970.

[88] Nicola Bonini, Michele Lazzeri, Nicola Marzari, and Francesco Mauri. *Physical Review Letters*, 99(17):176802, 2007.

[89] Michele Lazzeri, Claudio Attaccalite, Ludger Wirtz, and Francesco Mauri. *Physical Review B*, 78(8):081406, 2008.

[90] Tobias Kampfrath, Luca Perfetti, Florian Schapper, Christian Frischkorn, and Martin Wolf. *Physical Review Letters*, 95(18):187403, 2005.

[91] Lei Wang, Dahai He, and Bambi Hu. *Physical Review Letters*, 105(16):160601, 2010.

[92] D. W. Boukhvalov, M. I. Katsnelson, and A. I. Lichtenstein. *Physical Review B*, 77(3):035427, 2008.

[93] Xiao-Dong Wen, Louis Hand, Vanessa Labet, Tao Yang, Roald Hoffmann, N. W. Ashcroft, and et al. *Proceedings of the National Academy of Sciences*, 108(17):6833, 2011.

[94] Haijun Shen. *Micro Nano Letters, IET*, 8(10):740, 2013.

[95] Dengfeng Li, Yong Xu, Xiaobin Chen, Bolin Li, and Wenhui Duan. *Applied Physics Letters*, 104(14):143108, 2014.

[96] Marcel H. F. Sluiter and Yoshiyuki Kawazoe. *Physical Review B*, 68(8):085410, 2003.

[97] S. Ghosh, I. Calizo, D. Teweldebrhan, E. P. Pokatilov, D. L. Nika, A. A. Balandin, and et al. *Applied Physic Letters*, 92 (15):151911, 2008.

[98] Bo Qiu and Xiulin Ruan. *Applied Physic Letters*, 100(19): 193101, 2012.

[99] Jin-Wu Jiang, Bing-Shen Wang, Jian-Sheng Wang, and Harold S Park. *Journal of Physics: Condensed Matter*, 27 (8):083001, 2015.

[100] Emiliano Cadelano and Luciano Colombo. *Physical Review B*, 85:245434, 2012.

[101] Lei Wang and Baowen Li. *Physical Review Letters*, 99(17): 177208, 2007.

[102] M. Terraneo, M. Peyrard, and G. Casati. *Physical Review Letters*, 88(9):094302, 2002.

[103] D. Sawaki, W. Kobayashi, Y. Moritomo, and I. Terasaki. *Applied Physics Letters*, 98(8):081915, 2011.

[104] Gang Wu and Baowen Li. *Physical Review B*, 76(8):085424, 2007.

[105] W. Kobayashi, Y. Teraoka, and I. Terasaki. *Applied Physics Letters*, 95(17):171905, 2009.

[106] Riccardo Rurali, Xavier Cartoixà, and Luciano Colombo. *Physical Review B*, 90(4):041408, 2014.

[107] Ming Hu, Pawel Keblinski, and Baowen Li. *Applied Physics Letters*, 92(21):211908, 2008.

[108] C. W. Chang, D. Okawa, A. Majumdar, and A. Zettl. *Science*, 314(5802):1121, 2006.

[109] Stefano Lepri, Roberto Livi, and Antonio Politi. *Physics Reports*, 377(1):1, 2003.

[110] Nuo Yang, Gang Zhang, and Baowen Li. *Applied Physics Letters*, 93(24):243111, 2008.

[111] Jiuning Hu, Xiulin Ruan, and Yong P Chen. *Nano Letters*, 9(7):2730, 2009.

[112] A Rajabpour, S M Vaez Allaei, and F Kowsary. *Applied Physics Letters*, 99(5):051917, 2011.

[113] Lei Wang, Bambi Hu, and Baowen Li. *Physical Review E*, 86(4):040101, 2012.

[114] Nuo Yang, Xiaoxi Ni, Jin-Wu Jiang, and Baowen Li. *Applied Physics Letters*, 100(9):093107, 2012.

[115] Nuo Yang, Gang Zhang, and Baowen Li. *Applied Physics Letters*, 95(3):033107, 2009.

[116] D.B. Go and Mihir Sen. *Journal of Heat Transfer*, 132(12): 124502, 2010.

[117] Yogesh Sonvane, Sanjeev K Gupta, Pooja Raval, Igor Lukačević, and Pankajsinh B Thakor. *Chemical Physics Letters*, 634:16, 2015.

[118] S. Piscanec, M. Lazzeri, F. Mauri, and A. C. Ferrari. *European Physical Journal*, 148(1):159, 2007.

[119] Alessio Paris, Nikolay Verbitskiy, Alexei Nefedov, Ying Wang, Alexander Fedorov, Danny Haberer, Martin Oehzelt, Luca Petaccia, Dmitry Usachov, Denis Vyalikh, and Sachdev et al. *Advanced Functional Materials*, 23(13):1628, 2013.

[120] V. K. Tewary and B. Yang. *Physical Review B*, 79(12):125416, 2009.

[121] Dhruv Singh, Jayathi Y. Murthy, and Timothy S. Fisher. *Journal of Applied Physics*, 110(11):113510, 2011.

[122] Neil W. Ashcroft and N. David Mermin. *Solid State Physics*, volume 2. 1976.